Aus der Klinik für Hals- Nasen- Ohrenheilkunde. Kopf- und Halschirurgie
der Medizinischen Fakultät Mannheim
(Direktorin: Prof. Dr. med. Nicole Rotter)

3D BIO-PRINTED IN VITRO MULTICELLULAR MODEL FOR HEAD AND NECK SQUAMOUS CELL CARCINOMA

Inauguraldissertation
zur Erlangung des Doctor scientiarum humanarum
der
Medizinischen Fakultät Mannheim
der Ruprecht-Karls-Universität
zu
Heidelberg

vorgelegt von

ALEXYA AZHAKESAN

aus

NAGERCOIL, INDIA

2025

Dekan: **Prof. Dr. Sergij Goerdt**

Referent(in): **Prof. Dr. Nicole Rotter**

Dedicated to

My beloved brother…

Whose unseen presence has been a guiding light throughout my entire life. Though we have never met, you have inspired me deeply, and meeting you remains my greatest wish!

To you I owe everything, my brother!

INDEX

LIST OF FIGURES

LIST OF TABLES

LIST OF ABBREVIATIONS

A

Alg- Alginate
ATP- Adenosine triphosphate

B

BSA- Bovine serum albumin

C

CAD- Computer aided design
CTC- Carboxymethylated tunicate nanocellulose
Carboxy-NC- CTC mixed with alginate
Cis80- Cisplatin 80 µM

D

2D& 3D- 2- & 3-Dimension
DLP- Digital light process
DMEM- Dulbecco's modified eagle medium
DPBS- Dulbecco's phosphate-buffered saline

E

EBV- Epstein-Barr virus
EGFR- Epidermal growth factor receptor
ECM- Extracellular matrix
EMT- Epithelial mesenchymal transition
ELISA- Enzyme linked immunosorbent assay
EMEM- Eagle's minimum essential medium
EDTA- Ethylenediaminetetraacetic acid
E-cad- E-cadherin

F

FDM- Fused deposition model
FBS- Fetal bovine serum

N

NK- Natural killer
NAM- Novel alternative method
NC- Nanocellulose
NK-κB- Nuclear factor kappa-B

P

PEG- Polyethylene glycol
PD-L1- Programmed death-ligand 1
PFA- Paraformaldehyde

Q

qPCR- quantitative Polymerase chain reaction

R

RCT- Radiochemotherapy
RT- Radiotherapy
R/M- Recurrent/ metastatic
RLU- Relative luminescence unit
RGD- Arginylglycylaspartic acid
ROI- Region of interest

S

SSE- Semi-solid extrusion
SLA- Stereolithography
SEM- Scanning electron microscopy
StemMACS™ XF- StemMACS™ MSC expansion basal media with growth factor
SD- Standard deviation
STING- Stimulator of interferon genes
SNAIL- Snail super family of zinc-finger transcription factors

G

GelMA- Gelatin methacryloyl
GelMAA- GelMA in Alginate

H

HNSCC- Head and neck squamous cell carcinoma
HNC- Head and neck cancer
HPV- Human papillomavirus
HA- Hyaluronic acid
hNC- human Nasal chondrocytes
hPL- human Platelet lysate
H&E- Hematoxylin and eosin
HTS- High-throughput study

I

IHC- Immunohistochemistry
IF- Immunofluorescence

L

LIFT- Laser-induced forward transfer

T

TNM- Tumor node metastasis
TME- Tumor microenvironment
TTC- TEMPO oxidized tunicate nanocellulose
TEMPO-NC- TTC mixed with alginate
TPS- Tumor proportion score

U

UV- Ultra-violet
ULA- Ultra low attachment

V

VEGF- Vascular endothelial growth factor

Z

ZEB1- Zinc finger E-box binding homeobox 1

1. INTRODUCTION : HEAD AND NECK SQUAMOUS CELL CARCINOMA (HNSCC)

Cancer is characterized by the uncontrolled proliferation of abnormal cells, which have the potential to invade other parts of the body while evading the immune system. [1-5] Unlike normal cells, which adhere to a regulated growth pattern, cancer cells undergo chronic proliferation driven by various biological factors. [1-5] In the context of head and neck cancers (HNCs), key risk factors that can trigger the transformation of normal healthy cells into a malignant state include tobacco smoking, alcohol consumption, and other factors such as the presence of oncogenic strains of human papillomavirus (HPV) and the Epstein-Barr virus (EBV). [1-6] Head and neck squamous cell carcinomas (HNSCC) originate from the mucosal epithelium in the oral cavity, pharynx and larynx in the head and neck region (Figure 1). [1-4, 7, 8] Additionally, chronic exposure of the upper aerodigestive tract to all factors mentioned above, can result in premalignant lesions of the mucosa and ultimately leading to HNSCC development. Globally, HNSCC was responsible for more than 1,464,550 incident cases and 487,993 deaths in 2020, ranking as the 3rd most prevalent cancer type worldwide. [9] The incidence in males is significantly higher than in females, with a male-to-female ratio ranging from 2:1 to 4:1. [9] HNSCCs represent an invasive solid tumor type that accounts for approximately 90% of HNCs. [9] Especially, HNSCCs are noted for their substantial heterogeneity, with ample intra-tumor genetic diversity that poses a profound impact on health worldwide. [8, 9] Patients diagnosed with HNCs often experience complex issues such as difficulties in swallowing, breathing, and communication, as well as psychosocial changes, leading to an increased burden on healthcare systems significantly impacting everyday livelihood of those diagnosed.[7, 8, 10] The prognosis for patients with HNSCC is strongly influenced by tumor localization, stage, and the presence of metastasis, with a 5-year survival probability ranging between 45% and 60%. [7, 8, 10] Most of the patients, nearly 70% are often diagnosed at advanced or terminal stages needing high-intensive therapeutic strategies and triggering the possibility of tumor recurrence. [1-4, 7, 8]

1.1. General treatment options

Assessment of HNSCCs involves clinical evaluation, along with histopathological and radiologic assessments, to determine the tumor-node-metastasis (TNM) stage. [5-7] The TNM classification guides the clinical treatment approach. Historically, surgical resection combined with radiochemotherapy (RCT) has been considered a standard treatment. [5-7] Contrastingly, poor diagnosis calls for a more aggressive multimodal treatment approach, which may include surgical resection, RCT, immunotherapy, and other combinational therapies. [5-7]

Meanwhile, radiotherapy (RT) affects both cancerous and normal cells, leading to DNA damage activating various cell death pathways, including apoptosis, senescence, necrosis, and autophagy. [11, 12] While this process can effectively eradicate cancer cells, it also causes substantial damage to normal tissues. Therefore, it is crucial to maintain a balance between tumor control and normal tissue preservation, known as the therapeutic window. [11, 12] This balance is often achieved by administering the total radiation dose in multiple fractions, allowing normal tissues to partially recover between treatments. To enhance the efficacy of RT maintaining the therapeutic window, it is often combined with chemotherapy to overcome radiation resistance. [5, 6, 12, 13] A commonly employed combination in RCT involves the use of the cisplatin alongside radiation. [5, 6] Cisplatin enhances the effects of radiation by increasing DNA damage in cancer cells, though it also amplifies the dose delivered to normal tissues, it also increases the risk of toxicity. [5, 6, 12-14] Studies have shown that the side effects of this combination treatment can be particularly severe in patients with advanced or terminal-stage disease. [5, 6, 12-14] As a result, RCT with cisplatin is typically recommended only for patients with adequate renal function to mitigate these risks. [5, 6, 12-14]

Henceforth, to effectively improve the therapeutic regimen, and in search of patient specific treatments, recently, targeted therapies, particularly immunotherapies, have gained prominence and have shown relative effectiveness. Especially in patients with advanced-stage HNSCC drug resistance remains a significant challenge in therapy development. In an attempt to overcome the side effects caused due to RT with cisplatin, cetuximab, a monoclonal antibody drug targeted against the epidermal growth factor (EGFR) receptor became effected to be administered along with RT. [5, [6, 12-14] Given EGFR is overexpressed in tumor cells, targeting EGFR not only alters tumor progression, angiogenesis, invasion and metastasis, it also triggers immune response by the activation of natural killer (NK) cells and dendritic cells. [6, 15, 16] Generally, tumors have mechanisms to resist the radiation acquired damages, also in HNSCCs the cure rate from RT is relatively limited due to the tissue complexity. [5, 6] Moreover, irrespective of RT, drug resistance has become a major challenge in drug development or treatment regimen of HNSCC. [17]

Overcoming these challenges requires a deeper understanding of HNSCC pathophysiology and progression mechanisms to develop novel treatments and improve the efficacy of existing treatments. Despite these efforts, a significant proportion of treated patients experience tumor recurrence or develop a second primary tumor within a five-year period. [5, 6, 13, 17, 18] Recurrent or metastatic (R/M) HNSCC is therefore common and an indication of urgent need for more effective and targeted multimodal therapies.

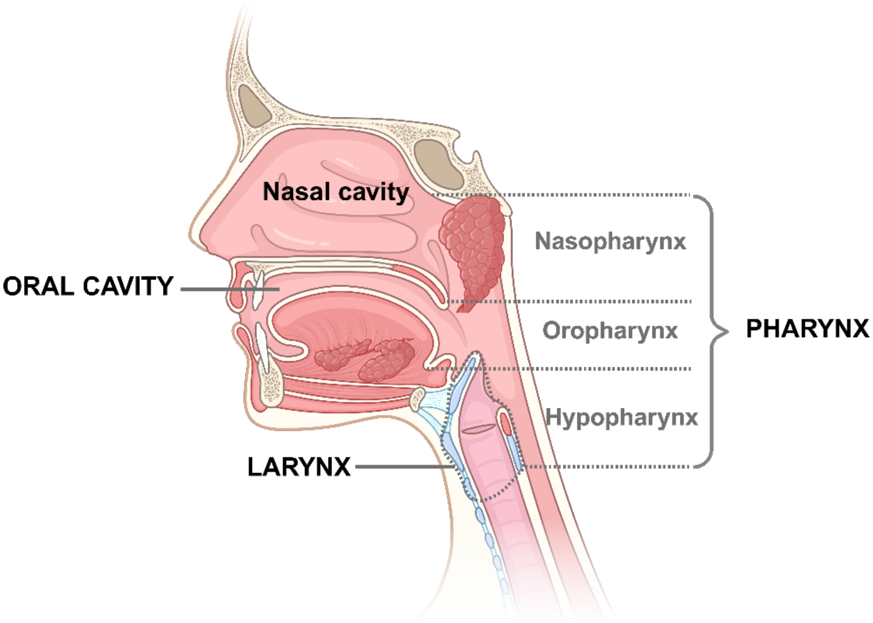

Figure 1 Anatomical illustration of head and neck tumors highlighting conventional tumor origin sites, including the oral cavity, nasopharynx, oropharynx, and hypopharynx. *Created in Biorender.*

1.2. Pathogenesis of HNSCC

The HNSCC tumor is complex and heterogeneous integrated with a complex extracellular matrix (ECM) that collectively makes the tumor-stroma tumor bed. [7, 10, 19-21] In the late 1800s there was already an indication pointing towards the possibility of connection that is veiled between the tumor and its microenvironment. [20] The tumor microenvironment (TME) comprises of tumor epithelial cells, and the surrounding extracellular matrix, mesenchymal cells, fibroblasts, vascular endothelial cells, bone-marrow derived cells, and immune cells activating endocrine and paracrine signals that supports cell proliferation and metastasis. [7, 10, 19-21] The complex cross-talk between the TME and the tumor entity, supplies necessary nutrients and oxygen supporting alteration of ECM structure, angiogenesis promotion, inducing immune checkpoint molecule expression, and production of immunosuppressive cytokines. [19] In recent studies, it has been proved that there is a strong inter-play between the tumor cells and the surrounding microenvironment that plays a functional part in tumor progression and dissemination. [8, 13]

The TME also influences the effect of immunotherapy or RCT on HNSCCs. [8, 13] Hence researchers have become curious in understanding and unveiling TME to develop and tailor effective novel anti-cancer therapeutics. To attain this objective, representative models that can precisely reciprocate the complexity and the heterogeneity seen in a typical HNSCC are required. The TME's influence on immunotherapy and other treatments necessitates the development of models that accurately replicate its complexity.[19] Such models would help in understanding how the TME affects treatment efficacy and in designing therapies that target specific components of the TME to enhance treatment outcomes. An ideal model can help us understand the tumor niches encouraging us to develop novel therapeutics.

1.3. State-of-the-art of preclinical tools

Traditionally, any anti-cancer drugs that are newly developed have to undergo a series of clinical trials before market authorization and being made available to patients. [2, 22] The drug-discovery process has been accelerated and improved but carried out in a focused patient-oriented manner considering the already known limitation in the existing preclinical screening strategy. [2, 22] One potential reason for the failure of any anti-cancer drug could be due to the wide range of *in vitro* and *in vivo* studies that a new drug undergoes to be tested using animal models. [3, 23] Unfortunately, most drugs are withdrawn at this preclinical drug trial phase in interpretation of the non-specificity of the current preclinical testing tools used. [3, 23] It is widely known that there is ample evidence from research that no animal model replicates and equates to the normal human situation. [1, 3, 24-26] Beginning from the intra-species differences that create receptor non-specificity, varied immune system reactions, and differential drug metabolism to the extreme lack of genetic diversity in the used inbred laboratory animals, that is coupled with associated ethical dilemmas, animal testing in general raises much controversy lately. [1, 3, 24-26] In particular, there is a consensus developed within areas of drug discovery and toxicological investigations on the need for complex, predictive and reproducible human-based models among scientists, pharmaceutical companies, and government healthcare policy makers. [24] There is need of human-based, reproducible *in vivo*-like preclinical models supporting the proposed and preferred paradigm shift. [1, 3, 24-26] In recent years, the so-called novel alternative methods (NAMs) have been introduced- methods that can replace *in vivo* experiments following the 3R principle: Reduce, Replace, and Refine.[27-30] In support of this trend, researchers, clinicians, and pharmaceutical companies have been focusing on the fabrication of *in vitro* preclinical models that are capable of recapitulating the complex nature of the TME. [1, 3, 24-26]

1.3.1. Current tumor modelling methods encompass various facets of organ and tissue complexity

2D (2-dimensional) monolayer cultures have demonstrated as the main *in vitro* modelling setup used in preclinical testing. While these 2D systems provide user-friendly features and are supported by extensively established protocols, their relevance has come into question. This is greatly due to their shortcomings in replicating the complex biochemical and mechanical signals of native tissues. [1, 31, 32] Although 2D models have been indispensable in the advancement of the basic understanding of cellular pathophysiology, they fail at a multicellular level. [1, 31, 32] More precisely, they cannot accurately replicate cell-cell and cell-matrix interactions, let alone the complex inter- and intracellular pathways involved in drug screening and toxicological studies. This limitation extends to their inability to mimic their corresponding changes in protein and gene expression profiles observed *in vivo*. [1, 31, 32]

On the other hand, as already mentioned, the widely used *in vivo* models- PDX and animal models are currently relatively less preferred due to the changing norms in drug discovery. [33] Meanwhile, *ex vivo* models- such as explant cultures represent the native tissue as best since it is directly derived from the patient. However, it is greatly limited by the availability of tumor tissue samples. Another drawback with explant models is that they do not allow for long-term cultures and have low reproducibility. [33] To develop more accurate preclinical tools with high resemblance to the natural tissue environment, many human-based *in vitro* models have been established using various tissue engineering methodologies. Such established models are facilitated by combining biology-based models- spheroids, organoids-together with engineering-based models- scaffolds, bioprinted constructs, and organ/tissue-on-a-chip models. [34-38] Every tumor model has its own advantages and disadvantages (Table 1).

Table 1 Advantages and limitations of different tumor models (including in vitro, ex vivo and in vivo model systems)

Tumor models	**Model definition [34-38]**	**Advantages [34-38]**	**Limitations [34-38]**
In vitro models			
2D models	Cells cultured on a flat 2D surface	- High throughput - High reproducibility - User friendly - Low cost	- Low physiological relevance - High probability of genetic drift - Limited cell- matrix interactions
3D models	Biological or engineering approaches to simulate tumor environments		
	3D models- Biological approaches		
Spheroids	Cells self-assemble into aggregates	- High throughput - High reproducibility - User friendly - Low cost - Facilitates cell-cell and cell-matrix interactions	- Heterogeneous sized spheroids - Lacks native tissue spatial organization - Restricted oxygen/ nutrient transfer
Scaffolds	Cells embedded in a 3D matrix	- Reproducibility (limited to a batch) - User friendly (limited to existing and automated protocols) - Relatively low cost - Facilitates cell-cell and cell-matrix interactions	- Adaptable throughput but limited to a batch - Non-representative scaffold architecture - Inefficient oxygen/ nutrients transfer - Limitations in long-term culture due to compromising

			biochemical and mechanical properties of the scaffold
Organoids	Stem cells/ progenitors self-organize in 3D structures	- Resembles native tissue organisation - Relatively intermediate cost - Supports long-term culture - Scalable culture model - Biomarker identification possible	- Low throughput - Low reproducibility - High variability in size/ shape - Laborious protocols - Not user friendly
	3D models- Engineering approaches		
Bioreactors	Cells/ tissues in a bio physiologically well-defined environment	- High throughput - Long term culture possible - Reproducible dynamic microenvironment - Scalable culture model	- Extremely expensive set-up - Difficult for automation - Laborious protocols tailored for specific read-outs - Not user friendly - Limited control over the mechanical inputs
Micro physiological systems (MPS)	Bio-engineered models mimicking native tissue physiology	- High throughput - High physiological relevance - Cell-cell, cell-matrix, cell-immune and cell-vascular network cross talks can be modelled - Multi-organ effect can be studied	- Expensive set-up - Difficult for automation and highly susceptible to errors (Special protocols needed for read-outs) - Lacks the incorporation of multi-dimensional tissue architecture - Difficult to scale up
Biofabricated models	Bioprinted models mimicking native tissue spatial organisation	- High throughput - Highly reproducible - High physiological relevance - Relatively intermediate cost - Relatively high automation - Cell-cell, cell-matrix, cell-immune and cell-vascular network cross talks can be modelled - Multi-cell effect can be studied	- Prolonged printing time for multicellular models - Geometric limitations - Challenging to balance biocompatibility, printability while fulfilling cell specific growth necessities - Opting a hydrogel that is compatible on a multi-cellular level with drug compatibility is challenging
Ex vivo models			
Explant models	Patient-derived tumor tissue fragments/ slices	- High throughput (restricted to the resected tumor size but in addition cohort studies must be performed) - High physiological relevance - Automation possible - Retained native ECM - Cheaper than animal models	- Experimental ease and reproducibility restricted - Difficult to access patient tumor tissue with equivalent pathophysiology - High contamination risk
In vivo models			

PDX models	Patient-derived tumors tissue xeno transplanted into immune deficient/ humanised mice	- High native tumor relevance - Automation possible but highly laborious - Recapitulates cell-matrix interactions - Recommended as a preclinical tool	- Low throughput - Inter-species differences - Lacks immune microenvironment - Sample limitation - Laborious protocols requiring trained officials/ scientists - Lures ethical concerns and poses constraints - Expensive and time-consuming
Animal models	Transplanted human tumors or artificially induced tumors in animals	- High reproducibility - High native tumor relevance - Drug kinetics/ toxicological studies possible - Recommended as a preclinical tool	- Low throughput - Intra-species differences - Laborious protocols requiring trained officials/ scientists - Expensive and time-consuming

1.3.2.Advancing cell culture to 3D in vitro models

As previously stated, given the constraints that prevails in current 2D *in vitro*, as well as other *ex vivo* and *in vivo* models, 3D cultures provide significantly improved clinical relevance, especially in terms of drug discovery. [34-38] Although there are different 3D *in vitro* models (Table 1), biofabricated models using 3D bioprinting technology offer a promising possibility to mimic the TME. Moreover, 3D biofabricated models facilitate the incorporation of spatial-temporal organisation, biochemical, and mechanical signals relevant to HNSCC. [22, 25, 26, 39, 40] In addition, the integration of native-like complex 3D structures facilitates the modulation of multi-cellular responses to drugs, the examination of their kinetics, and the investigation of their impacts on inter- and intracellular interactions within a three-dimensional framework. [25, 39, 41] Besides its unique advantages in drug discovery, bioprinting technology offers to design and print structures in a custom manner with a defined geometry that consists of a mixture of living cells and biomaterials at a desired ratio complementing cell growth and progression. [25, 39, 41] Thus, a bioprinted 3D system that integrates complexly engineered biologically components is comparably precise, time efficient, and reproducible having its application in high-throughput drug screening, gene therapy, personalized medicine, toxicological studies. [40] Owing to these advantages, 3D bioprinting technology was preferred in this study to develop a 3D *in vitro* preclinical tool for HNSCC.

1.4. 3D Bioprinted tumor modelling

3D bioprinting, allows to replicate the intricate spatial organization seen in native tumor. In the last decade, 3D bioprinting has been increasingly employed in cancer research owing to its distinctive advantages in accurately replicating the TME (Table 1). [25, 26, 34-41] Initially, the 3D bioprinting technology entailed the deposition of certain cell types into different hydrogel matrices derived from natural biopolymers, synthetic polymers, or decellularized extracellular matrices of human or animal origin. [25, 26, 39, 42] Pioneer research with 3D bioprinting technology employed inkjet-based bioprinting, establishing a fundamental framework for the advancement of bioprinted models. [25, 39, 40, 42] As the necessity to mimic the complex and multimodal architecture of biological tissues became evident, advanced bioprinting techniques were developed. Meanwhile, a diverse array of 3D bioprinting techniques/ methods have been developed over time, each aimed at addressing particular issues associated with the replication of tissue structure and function. Different methods encompass inkjet printing, extrusion-based bioprinting, laser-assisted bioprinting, stereolithography, light- or droplet-based bioprinting, electro-hydrodynamic bioprinting, volumetric bioprinting, and the more modern fresh bioprinting. [25, 39, 40, 42] Every bioprinting technique has its unique advantages and tackles particular limitations, influenced by factors such as ease of use, printing resolution, the diversity of cell types that can be integrated, the range and complexity of required biomaterials, accuracy in reproducing the intended architecture, and the necessity for biodegradability in certain tissue characteristics. [42] Furthermore, post-printing characterization is essential for assessing the fidelity, viability, drug kinetics, and modulation in biomarker expression of the printed structure/ construct in comparison to its native tissue. [33, 43, 44] As a result, continuous improvements in bioprinting methods are enhancing the accuracy, intricacy, and biomimetic authenticity of 3D printed structures, expanding their applications in regenerative medicine and cancer research as well as translation of new therapeutics into the clinical front.

This study has focused on extrusion-based bioprinting, a method selected for its user-friendly nature and rapid reproducibility (Table 2). [25, 39, 40, 42] In brief, extrusion-based bioprinting uses a pneumatic/ screw/ piston-based extrusion pump to extrude continuous filaments of the bioink in a layer-by-layer fashion. This approach aligns with the requirements for building the elements in the HNSCC TME in a step-by-step manner, thus offering a balance between technical ease and functional robustness. It is true that the extrusion bioprinting is relatively simpler and highly user-friendly, however there are certain critical parameters that must be adjusted and optimized, to achieve a highly printable, cell-friendly model that promotes cell growth, proliferation, and migration.

Table 2 Different 3D bioprinting methods depicting their mechanism and resolution [25, 39, 40, 42]

3D Bioprinting Method	Description	Printing resolution	Speed	Cost
Inkjet (or drop-on-demand) bioprinting	Employs thermal or acoustic pressures to eject microdroplets of bioinks (e.g., cells, biomaterials) onto a substrate. Thermal mechanisms increase the print-head temperature to generate enough/ required pressure for droplet ejection. Meanwhile, acoustic mechanisms employ piezoelectric crystals to fragment/ segregate the liquid into droplets. Frequently employed for high-throughput and cellular patterning applications.	300 – 100µm	Slow-medium	Low
Extrusion-based bioprinting	Employs either semi-solid extrusion (SSE) or fused deposition modelling (FDM) to continuously extrude bioinks (e.g., hydrogels, cell-laden hydrogels) via a nozzle/ needle of selected diameter. This method accommodates highly viscous substances and facilitates the printing of larger, more intricate structures.	100 µm - 1cm	Slow-medium	Medium
Light-assisted bioprinting	Employs light sources (UV- or visible light) to deposit or crosslink biomaterials, such as hydrogels (with or without cells), into specified three-dimensional configurations. This method encompasses stereolithography (SLA) or digital light processing (DLP) and light sensitive biomaterials are used.	<1µm - 4000 cm	Fast	Medium-High
Laser-based bioprinting	Employs laser pulses to convey bioink (cells-laden hydrogels/ biomaterials) from printing cartridges onto a substrate, generally via laser-induced forward transfer (LIFT). This is the best method for the fabrication of high-precision tissue constructs including positioning of cells with high viability incurring minimal-to-no cellular damage.	10– 300 µm	Fast	High
Electrohydrodynamic bioprinting	Employs electric fields to produce ultra-fine jets/ filaments from a liquid bioink, resulting in high-resolution structures. It is capable of printing	0.01-40µm	Fast	High

	nanofiber scaffolds or microdroplets for accurate cellular organisation. Usually employed for multimodal/ heterotypic 3D structures that involve multiple layering of hydrogels/ biomaterials.			
Volumetric bioprinting	A rapid 3D printing method that uses light to harden a bioink in one step by illuminating a rotating volume. This method facilitates the instant fabrication of intricate tissue structures between seconds to minutes (depending on the designed 3D structure).	25µm -4cm	Fast	High
Fresh bioprinting	Employs a sacrificial hydrogel as a support medium during bioprinting, which facilitates the fabrication of intricate, freeform 3D structures. The support bath can be detached post-printing, resulting in the retention of the bioprinted structure. This method is vastly used for bioprinting vascular networks in tumor modelling.	100µm – 1 mm	Fast	High

1.4.1. 3D Bioprinting parameters

The development of reproducible and viable 3D bioprinted HNSCC models hinges on a range of interdependent bioprinting factors. These include, designing an optimal 3D structure/model that is anatomically relevant, selecting appropriate cell types and tissue specific biomaterials, ensuring consistent and necessary nutrient supply, and usage of tailored hydrogels with relevant biochemical and mechanical properties suitable for bioprinting (Figure 2). [45, 46] In addition, fine tuning the bioprinting parameters such as bioprinting pressure, time, speed, temperature, nozzle diameter, infill density, pre-and post-print delay, printing pattern, and number of layers plays a critical role in achieving optimal print fidelity and bioconstruct viability. [45, 46] Also, the choice of crosslinking strategies- be it physical or chemical and the establishment of post-print culture and system specific characterization protocols are critical for successfully biofabricating a preclinical model.

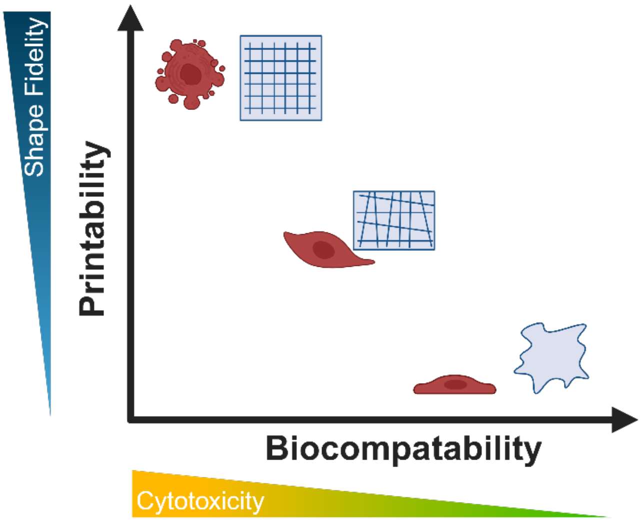

Figure 2 Schematic illustration depicting the interplay between bioprinting parameters and their impact on biocompatibility in achieving a viable bioprinted structure. *It is crucial to optimize the bioprinting parameters within the defined bioprinting window in compliance with the inversely proportional relationship between cytotoxicity and shape fidelity. Created using BioRender.*

1.4.1.1. Bioinks and biomaterials

Typically, extrusion-based 3D bioprinting relies on bioinks (hydrogels encapsulated with biological materials including cells, tissues, spheroids and organoids) with rheological properties that withstands the shear thinning behavior, recoverability, gelation kinetics, biocompatibility, biodegradability and additionally, its mechanical strength aligning with the cellular requirements across pre-processing, printing, and post-printing stages. [45, 46] Polymers and biomaterial formulations such as gelatin, polyethylene glycol (PEG), alginate (Alg), agarose, hyaluronic acid (HA), collagen, and nanocellulose (NC) are widely used due to their biocompatibility and their rapid stabilization properties. [47] However, these materials frequently present challenges such as low viscosity, batch-to-batch variability, and susceptibility to enzymatic degradation *in vivo* which to-date remain unaddressed. [47] Addressing the printability limitations within this window often involves modifications to bioinks through strategies such as surface functionalization, adjustments to biomaterial concentration based on specific objectives- enhancing the viscosity, surface tension and wettability, and the application of crosslinking techniques with enhanced functionalization (e.g., increased crosslinker concentration). [45-47] These approaches are intended to maintain structural fidelity while aligning bioink properties with the requirements for successful biofabrication. Advanced bioink formulations address such limitations within the ‘biofabrication window’ to balance printability, thereby protecting cell viability by optimising biomaterial composition, viscosity and crosslinking strategies (Figure 2). [48]

Recently, in contrast to the commonly used bioinks, nanocellulose (NC) has gained attention for its application in disease modelling, drug delivery, tissue engineering and regenerative medicine. [49-56] This is due to its profuse biochemical and mechanical properties i.e.- non-toxicity, high surface area, surface tunable chemistry, good mechanical strength, low bioburden and high-water retention capacity with high biocompatibility and low-to no cytotoxicity inducing no to low immune response. [49-56] Owing to its exclusive biochemical and mechanical properties, rapid developmental strategies have been built to tailor its properties for 3D bioprinting applications. NC-source and extraction method defines its unique physiochemical and mechanical properties. [49-56]

In this project, I used nanocellulose derived from tunicates. It is considered as one of the purest forms of cellulose without hemicellulose and lignin. Recently, *Gatenholm et al.* investigated tunicate-derived NC-based bioinks to analyze their bio-chemical and mechanical properties when printed with human nasal chondrocytes (hNC), thus interpreting their suitability as a biocompatible bioink for fabricating 3D bioprinted models. [57] The cell/ tissue type and the amount of cells/ tissue chosen defines the cell number to the bioink concentration ratio. Cell density/mL of bioink varies for every cell type depending upon the robustness and, sensitivity of the cell type of interest. Scientists and researchers have broadly experimented with 1×10^6 - 10×10^7 cells/mL of bioink for epithelial tumor cells and 1×10^6 - 5×10^6 cells/mL bioink fibroblast, endothelial and immune cells components.

1.4.1.2. 3D design

Prior to printing, computer-aided design (CAD) files are generated to create constructs with complex and anatomically relevant structures that are readable by the bioprinter. [44, 46, 48] These CAD files are then converted into G-code, which conveys the precise printing path and parameters (e.g., speed, location, and infill density) to the 3D printer. The bioprinting process typically operates at speeds ranging from 700 $mm\cdot s^{-1}$ to 10 $\mu m\cdot s^{-1}$. [44, 46, 48] Subsequently, bioinks are loaded into extrusion barrels for printing. Mechanical properties, such as viscosity and shear-thinning capacity, are critical for ensuring cell viability by allowing the bioink to flow under minimal applied stress during extrusion. The viscosities of bioinks suitable for extrusion-based bioprinting generally range from 30 to 6 × 10^7 mPa·s. [44, 46, 48]

Certain standard designs such as 3D cylinders and spheres are frequently employed to replicate tumor morphology, while honeycomb and leaf-like configurations are utilized to mimic vascular networks. [44, 46, 48] While gridded cylinders represent fibroblast networks, multi-layered cylinders or domes are often used to model co-cultured tumor-fibroblast microenvironments. Advanced technologies such as volumetric bioprinting and four-dimensional two-photon polymerization (4D 2PP) bioprinting, allows the precise replication of the TME while achieving higher resolutions. [24]

Principally, the pathology of HNSCC is characterized by a structure comprising tumor and matrix zones that become infiltrated by immune and endothelial components as the tumor progresses and metastases (Figure 9). Considering the complexity of the TME, the 3D structure was meticulously designed to reflect the pathological features of primary HNSCC tumors. In this study, a 3D cylinder was constructed to accurately represent the organisation of epithelial tumor cells.

1.4.1.3. Printing parameters

The bioprinting parameters used for every system are different and are tailored with respect to the specific system/model. [44, 46, 48] I experimented and defined the bioprinting parameters such as- cell density, growth media volume, growth factor concentration, surface modifier molecules (ligands), print head and print-bed temperature, printing speed & pressure, number of layers, printing pattern, infill density, nozzle/ needle size, flow rate; chemical crosslinking and post-printing characterisation can be adapted according to the system (Table 10). Secondly, while opting for biomaterials to encapsulate the HNSCC cells, the chosen biomaterial must complement typical cell behavior- such as cell growth, progression and migration. [44, 46, 48]

1.4.1.4. Cellular characteristics

To ensure reproducibility and viability of the 3D bioprinted HNSCC model, post-printing protocols play a pivotal role in fostering the desired cellular behaviors, including adhesion, proliferation, differentiation, and migration. [44, 46, 48] The interplay of biomaterial properties and cellular responses within the printed construct is influenced by several factors, such as the chemical composition of bioinks, crosslinking dynamics, and nutrient delivery within the construct. Optimal post-print culture conditions are required to sustain the viability of HNSCC cells while promoting phenotypic characteristics that mimic the tumor microenvironment (TME). [25, 26, 44, 48]

HNSCC is a heterogeneous malignancy characterized by its intricate interactions with the surrounding stroma, immune infiltrates, and vasculature. Reproducing this *complexity in vitro* requires precise modulation of the biophysical and biochemical cues imparted by the bioink and culture conditions. For example, the TME composition, including stromal fibroblasts and endothelial components, is essential to model tumor-stroma crosstalk and mimic angiogenesis and tumor progression pathways. [7, 19, 58]

Co-cultures of epithelial tumor cells with fibroblasts and immune cells have been shown to enhance tumor-specific traits, including matrix remodeling and epithelial-mesenchymal transition (EMT). [7, 19, 58] The integration of these co-culture systems into the 3D bioprinted HNSCC models ensures a comprehensive representation of the pathological hallmarks of the disease. Furthermore, vascularization strategies, such as incorporating endothelial cells or applying vascular growth factors, augment the physiological relevance of the bioprinted constructs. [7, 19, 58]

1.4.1.5. Crosslinking strategies and bioink innovations

Crosslinking strategies—physical, chemical, or enzymatic—are vital for achieving structural fidelity while preserving cell viability within bioprinted constructs.[44, 46, 48] Physical methods, such as ionic gelation, temperature- or UV- induced crosslinking, offer rapid stabilization but may compromise long-term mechanical properties.[59] Conversely, chemical crosslinking using agents like genipin or glutaraldehyde provides enhanced mechanical stability but requires optimization to mitigate cytotoxic effects. [59]

Advanced bioink formulations have emerged as a cornerstone of bioprinting innovations, particularly for cancer models. Hybrid bioinks combining natural polymers such as collagen or alginate with synthetic polymers like polyethylene glycol (PEG) have demonstrated improved tunability and biomechanical properties.[59, 60] Recent studies also highlight the potential of functionalized nanocellulose composites to synergize with these formulations, offering unparalleled biocompatibility and structural integrity. [33, 57, 59, 60]

1.4.1.6. Characterization and functional assessment of constructs

After bioprinting, thorough characterization of the 3D bioprinted constructs is indispensable to validate their fidelity to the designed structure and functionality.[48] Techniques such as confocal microscopy, scanning electron microscopy (SEM), and rheological analyzes are employed to assess cellular distribution, matrix composition, and mechanical stability. [44, 46, 48] Functionally, constructs are evaluated for their ability to replicate tumor progression, invasion, and response to therapeutics. The use of molecular assays such as qPCR, ELISA, and immunofluorescence enables the monitoring of cell-specific markers, signaling pathways, and ECM remodeling, which are key determinants of tumor behavior. [44, 46, 48] Every type of characterization experimental protocol must be tailored for the specific hydrogel-based 3D bioprinted construct. [48]

1.4.2.Applications and future directions

The successful development of viable and reproducible 3D bioprinted HNSCC models holds transformative potential for translational cancer research. Such models provide a robust platform for drug screening, enabling the evaluation of chemotherapeutic efficacy and resistance mechanisms under physiologically relevant conditions. [61] Furthermore, they can facilitate the study of immune-oncology therapies, where the inclusion of immune components within the TME allows for the assessment of immune cell-tumor interactions. [61]

Future advancements in bioprinting technology, including multi-material printing and real-time in situ monitoring, are anticipated to enhance the fidelity and scalability of these models.[24] Coupled with the integration of omics technologies and machine learning, these developments will drive precision medicine approaches tailored to HNSCC treatment. [24, 61, 62] By replicating the complex interplay of cellular and matrix components, these models provide an invaluable tool for unraveling the intricacies of HNSCC and accelerating the development of novel therapeutic strategies.[24]

1.5. AIMS

This thesis aims to develop a representative and predictive 3D bioprinted model for HNSCC, addressing critical challenges in preclinical cancer modeling (Figure 3). By leveraging 3D bioprinting technology, this work aims to establish a platform that replicates the native TME for applications in drug screening and personalized medicine.

The first and foremost aim focuses on the establishment of a 3D bioprinted HNSCC model as a proof-of-concept. This involves demonstrating the feasibility of bioprinting HNSCC cells that can survive long-term (≥21 days), maintain an epithelial phenotype, and support functional studies such as drug testing and toxicology studies. To achieve this, two NC-based bioinks- TEMPO-oxidized and carboxymethylated NC- were evaluated against gelatin methacryloyl (GelMA), all formulated with alginate for improved stability. The viability, cellular distribution, proliferation, and biomarker expression of HNSCC cell lines in these bioinks were investigated, alongside a breast cancer cell line for benchmark comparison. The cell distribution was evaluated by correlating the microstructural analysis of the bioinks using SEM. Additionally, the model was advanced/ upgraded to a heterotypic one by incorporating one of the additional cell types representative of the TME.

The second aim centers on the functional validation of the bioprinted HNSCC model through clinically relevant treatments. The response of UM-SCC-22B cell-laden Carboxy-NC constructs to platinum-based chemotherapy (80 μM) and fractionated irradiation (3x 2 Gy) was assessed. This functional assessment is strategized to assess the model’s ability to mimic patient-like responses to combined radiochemotherapy regimens, further supporting its translational relevance.

The third aim focuses on the development of a xeno-free, patient-derived 3D HNSCC explant model to enhance translational relevance. HNSCC explants were cultured in human platelet lysate (hPL) and commercially available, StemMACS™ MSC expansion media (StemMACS™ XF) media and compared to HNSCC explants cultured in fetal bovine serum (FBS). Key markers, including PD-L1, Ki-67, and vimentin, were analyzed to evaluate the explants' morphology, viability, and biomarker expression. The explants' responses to radio-chemotherapy were also assessed, with biomarker profiles compared to uncultured primary tissues to confirm physiological relevance.

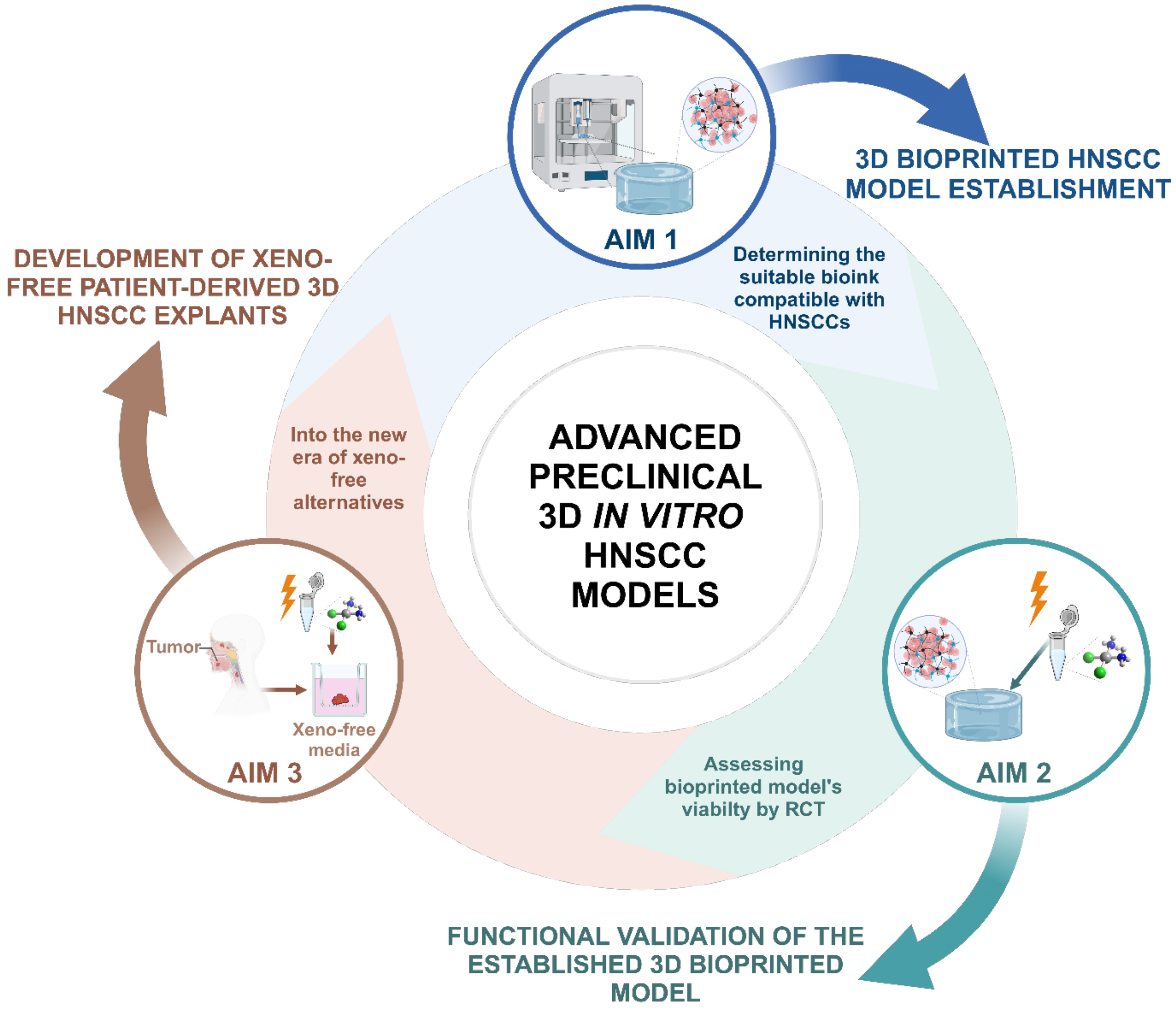

Figure 3 Graphical overview of the main goals presented in this thesis. *Created in Biorender.*

2. MATERIALS AND METHODS

2.1. MATERIALS

All the materials used in this thesis are presented below.

2.1.1. HNSCC cell/ tissue culture

Table 3 Cell lines used

Cell line name	Disease	Site of origin	Age/Gender	Doubling time
UM-SCC-14C	Oropharyngeal squamous cell carcinoma	Oral cavity; Floor of mouth	64yr/ Female	27 ± 4hr
UM-SCC-11B	Laryngeal squamous cell carcinoma	Larynx	64yr/ Male	31 ± 3hr
UM-SCC-22B	Hypopharyngeal squamous cell carcinoma	Lymph node metastasis	59yr/ Female	34 ± 2hr
MCF-7	Breast adenocarcinoma	Pleural effusion of metastatic breast	69yr/ Female	24hr

Table 4 Culture media, supplements, reagents, kits and consumables

Medium/ Reagent	Catalog No.	Manufacturer	Use
Eagle’s minimum essential medium (EMEM)	9047.1	Roth	HNSCC cell culture
Fetal bovine serum (FBS)	A5256701	Gibco	Cell culture
Antibiotic-Antimycotic	15240062	ThermoFisher	Cell culture
Dulbecco's Modified Eagle Medium (DMEM)	12491023	Thermo Fischer	MCF-7 cell culture
Liberase DH (1:100)	5401054001	Sigma Aldrich	Enzymatic digestion of primary cells
PneumaCult™-Ex Plus basal medium	# 05040	Stemcell Technologies	
L-glutamine	9183.1	Roth	Cell culture
Hydrocortisone	# 07926	Stemcell Technologies	Primary cell culture
Human Fibroblast Expansion Basal Medium	M106500	Gibco	Fibroblast cell culture
Dulbecco modified Eagle’s medium (DMEM)	#880010	Lonza	Primary explant procurement
Puromycin	ant-pr-1	InvivoGen	Primary explant procurement
StemMACS™ MSC expansion media	130-091-680	Miltenyi Biotec	Primary explant culture
Heparin Cofactor II	375115-100UG	Merck Millipore	Primary explant culture

Dulbecco's phosphate-buffered saline (DPBS) without calcium and magnesium	14190144	ThermoFisher	Cell harvesting
Dulbecco's phosphate-buffered saline (DPBS) with calcium and magnesium	14040083	ThermoFisher	Cell harvesting
0.4% Trypan blue	17-942E	Lonza	Counting cells
0.5 % Trypsin/EDTA (10x)	15400-054	Gibco	Passaging cells
CELLSTAR T-75 flask	GN658175	Greiner	Cell culture
Nucleon Sphera 96-well ultra-low attachment (ULA) plates	174925	Thermofisher Scientific	Bioconstruct culture
ThinCert	665610	Greiner Bio-One	Explant culture

2.1.2. Bioprinted model fabrication

Table 5 Hydrogels, reagents and consumables for bioprinting

Name	Catalog No.	Manufacturer	Use
TUNICELL TTC +M Medical Grade	-	Ocean TuniCell AS	TEMPO-NC Bioink preparation
TUNICELL CTC +M Medical Grade	-	Ocean TuniCell AS	Carboxy-NC Bioink preparation
Pronova® SLG 100 Ultrapure, sodium alginate	# 4202101	IFF Nutrition Norge AS	NC-Bioink preparation
D-mannitol	29054300000	Sigma Aldrich	Diluting alginate
GelMA A	IK3521020303	CELLINK	GelMAA Bioink preparation
Empty cartridges with end and tip caps, 3 mL	CSC010300102	CELLINK	NC-Bioink Bioprinting
Female/Female Luer Lock Adapter	OH000000010	CELLINK	Bioprinting
UV-shielding cartridges, 3 mL	CSO010311502	CELLINK	GelMAA-Bioink Bioprinting
Temperature-controlled printhead	CL-PH-TCPH	CELLINK	GelMAA-Bioink Bioprinting
Sterile high-precision conical bioprinting nozzles, 22G-410µm	NZ3220005001	CELLINK	NC-Bioink Bioprinting
Sterile standard blunt needles 22G	-	CELLINK	GelMAA-Bioink Bioprinting
$CaCl_2$ Crosslinking Agent	CL1010006001	CELLINK	Crosslinking bioconstructs
Cisplatin		Selleckchem	Chemotherapy treatment

2.1.3. Characterization

Table 6 Assay kits, antibodies and consumables for model characterization

Name	Catalog No.	Manufacturer	Use
3D CellTiter-Glo® viability kit	G9681	Promega	Viability test
Xylol	9713.1	Roth	IHC sample preparation
Ethanol	9065.2	Roth	IHC sample preparation
Mayer's hematoxylin	HMM125	ScyTek Laboratories	H&E staining

Eosin	EYA500	ScyTek Laboratories	H&E staining
ROTI®Mount mounting medium	HP68.1	Roth	H&E and IHC staining
Citrate buffer	C2488	Sigma Aldrich	IHC staining
Tris EDTA-based buffer	93302	Sigma Aldrich	IHC staining
Hydrogen peroxide	H1009	Sigma Aldrich	IHC staining
Normal sheep serum	S22-M	Sigma Aldrich	IHC & IF staining
Ki-67	#IR626	Agilent Technologies	IHC staining
PD-L1	#13684	Cell Signaling Technology	IHC staining
Vimentin	#5741	Cell Signaling Technology	IHC & IF staining
Antibody diluent	#S080983-2	Agilent Technologies	IHC staining
Anti-rabbit multilink antibody	#RPN 1004V	Cytiva	IHC staining
Anti-mouse antibody	#RPN 1001V	Cytiva	IHC staining
Streptavidin-biotin horseradish peroxidase complex	#RPN1051-2ML	Merck	IHC staining
3-amino-9-ethylcarbazole	ACG500-IFU	ScyTek Laboratories	IHC staining
Permanent Mounting Media	SCY-PMT030	ScyTek Laboratories	IHC staining
Blocker BSA	37520	Thermo Fischer	IF wash buffer
Triton™ X-100	9036-19-5	Millipore Merck	IF wash buffer
TWEEN® 20	28320	Thermo Fisher	IF wash buffer
Normal goat serum		BIOZOL	IF staining
E Cadherin	ab219332	Abcam	IF staining
Vimentin Rabbit	5741T	Cell Signalling Technologies	IF staining
Ki-67	BNC942463-100	BIOZOL Diagnostica Vertrieb	IF staining
Anti-rabbit Alexa-488	#4412	Cell Signalling Technology	IF staining
Anti-rabbit Alexa 647	111-605-003	Jackson ImmunoResearch	IF staining
DAPI	D1306	Thermo Fischer	IF staining
Agarose	9012-36-6	Sigma Aldrich	IF sample mounting
μ-Dish 35 mm (glass bottom)	81218-200	Ibidi	Confocal imaging

2.1.4. Instruments

Table 7 Overall instruments used for characterization

Name	Manufacturer	Use
Infinite 200 Pro plate reader	Tecan Austria	Viability plate reader
BIO X™	CELLINK	Bioprinting
Medical linear accelerator	Synergy; Elekta AB	
Carl Zeiss A	Zeiss	
Alpha 3-4 LSC basic	Martin Christ	Freeze-drying bioconstructs
Sputter- targets gold-palladium target	Rave Scientific	Sputter coating bioconstructs
Zeiss Leo 1530	Zeiss	SEM
TCS SP8 upright	Leica	Confocal microscope

2.2. METHODS

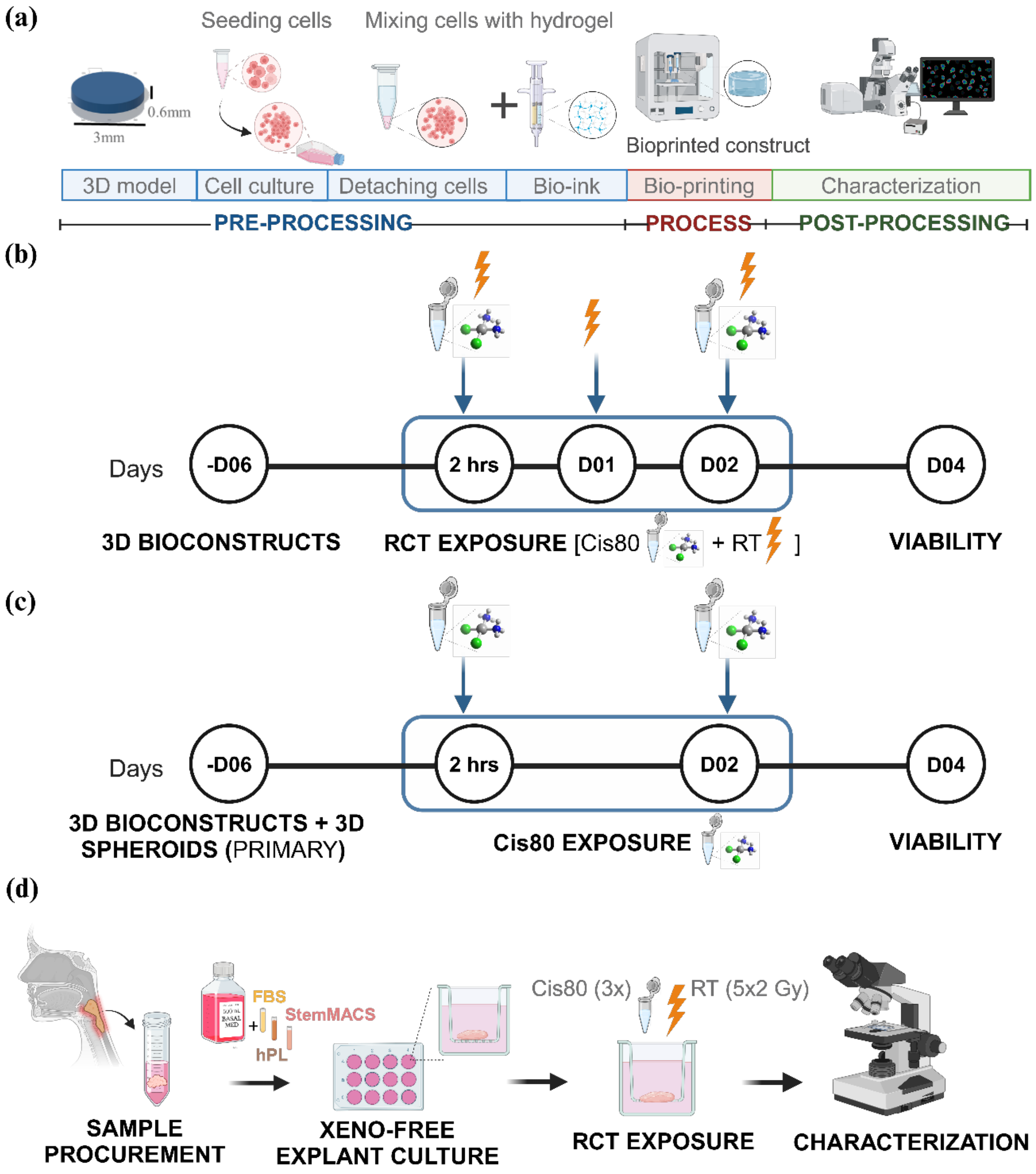

Figure 4 Illustration depicting the step-by-step methods involved in the biofabrication of a 3D bioprinted HNSCC model, the establishment of a xeno-free explant model, and their functional validation with radiochemotherapy (RCT). *(a) The biofabrication of the 3D bioprinted model is outlined in three stages: pre-processing, processing, and post-processing. In the* ***pre-processing stage****, a 3D cylindrical structure (3 mm in diameter and 0.6 mm in height) was designed using 3D modeling software, while bioink formulations were prepared by incorporating HNSCC cell lines (UM-SCC-14C, 11B, and 22B) into hydrogel mixtures. These bioinks, optimized for bioprinting, combined nanocellulose-based hydrogels (TEMPO-NC: TEMPO-oxidized tunicate-derived NC; Carboxy-NC:*

carboxymethylated tunicate-derived NC) with gelatin methacrylate (GelMA) and alginate. The ***processing stage*** *involved loading the bioinks into bioprinter cartridges and fabricating 3D cylindrical constructs through precise bioink deposition. In the* ***post-processing stage****, constructs underwent comprehensive characterization, including cell viability assays, proliferation analysis, cell-specific biomarker expression, and microstructural evaluation of cell-free hydrogels to assess model fidelity and functionality. (b) & (c) Functional validation demonstrated the efficacy of the treatment modalities on both cell line derived and patient derived HNSCC bioprinted model. While (b) narrates the UM-SCC-22B cell laden Carboxy-NC bioconstructs being exposed to RCT from days 00-03, (c) portrays patient-derived HNSCC cells biofabricated into bioprinted constructs and spheroids being subjected to Cis80 on days 00-03. (d) The process involved in establishing patient-derived 3D HNSCC explants in xeno-free- hPL and StemMACS™ XF media (hPL- human platelet lysate; StemMACS™ XF- StemMACS™ MSC expansion media XF supplemented) and compared to those in FBS (Fetal bovine serum) media grown tissues. The explants were subjected to RCT and characterized for their changes in morphology, proliferation and immune cell infiltration via H&E and IHC staining (H&E- Haematoxylin & Eosin; IHC- Immunohistochemical staining). Created in BioRender.*

2.2.1.HNSCC cell/ tissue source

The cell lines used (Table 8) to establish the 3D bioprinted HNSCC model in this thesis are listed below:

Table 8 A tabular overview of the HNSCC cell lines used in this thesis. [63, 64]

Cell line name	**Disease**	**Site of origin**	**Age/Gender**	**Doubling time**
UM-SCC-14C	Oropharyngeal squamous cell carcinoma	Oral cavity; Floor of mouth	64yr/ Female	27 ± 4hr
UM-SCC-11B	Laryngeal squamous cell carcinoma	Larynx	64yr/ Male	31 ± 3hr
UM-SCC-22B	Hypopharyngeal squamous cell carcinoma	Lymph node metastasis	59yr/ Female	34 ± 2hr
MCF-7	Breast adenocarcinoma	Pleural effusion of metastatic breast	69yr/ Female	24hr

The HNSCC cells were cultured in a culture media cocktail containing Eagle's minimum essential medium (EMEM) supplemented with 10% fetal bovine serum and 1% antibiotic-antimycotic mix. MCF-7 cells were cultured in a growth media cocktail prepared with Dulbecco's Modified Eagle Medium (DMEM) supplemented with 10% FBS and 1% antibiotic-antimycotic mix. All cells were cultured in T-75 flasks and were maintained in the conventional humidified culture conditions in an incubator at 37 °C with 5% CO_2. The cells were supplemented with fresh medium every 3 days. When cells reached confluency (85-90% confluency), they were trypsinized (with 2% trypsin). The harvested cells were counted using a hemacytometer. Meanwhile, a part of the cells was passaged at a seeding density of 3×10^5 cells/ T-75 flask.

The HNSCC cell line used for Aim 2 of this thesis was UM-SCC-22B. [63] The culture medium used for maintaining the HNSCC cells was identical to the growth medium employed for the establishment of the homotypic 3D bioprinted HNSCC model. The UM-SCC-22B cells were bioprinted at a concentration of 5×10^6 cells/mL.

To evaluate the functionality of the 3D bioprinted model, primary head and neck squamous cell carcinoma (HNSCC) cells were employed. These cells were derived from tumor tissues obtained from three independent donors, following informed consent and ethical approval from the Ethics Committee of the Medical Faculty of Mannheim, University of Heidelberg (Approval No. 2018-603N-MA). The study adhered to the principles outlined in the Declaration of Helsinki.

On the day of surgical resection, a portion of the tumor specimens was collected. Primary epithelial HNSCC cells were isolated through an enzymatic digestion process. The tissues were first rinsed with phosphate-buffered saline (PBS without Ca^{2+} and Magnesium) and then manually sectioned into fragments measuring approximately 2 mm^2. These fragments were digested in Liberase DH (1:100 dilution in Dulbecco's PBS containing calcium and magnesium) at 37 °C for 30 minutes under constant agitation. The resulting cell suspension was filtered through a 100-µm cell strainer and centrifuged to form a cell pellet.

The isolated cells were cultured in T-75 flasks using a custom-prepared primary cell culture medium. This medium consisted of PneumaCult™-Ex Plus basal medium supplemented with PneumaCult™ Ex Plus Supplement, as per the manufacturer's protocol, along with 1% L-glutamine, 1% antibiotic-antimycotic solution, and hydrocortisone (96 µg/mL). The cultures were maintained at 37 °C in a humidified environment with 5% CO_2 and passaged when reaching approximately 80% confluence.

The isolated cells from the resected sections were cultured in Fibroblast growth media cocktail for the culture of primary stromal cells. The fibroblast growth media consisted of the Basal medium for the expansion of human fibroblasts supplemented with 10% FBS, 1% L-glutamine, and 1% antibiotic-antimycotic mix. The cultures were maintained at 37 °C in a humidified environment with 5% CO_2 and passaged when reaching approximately 80% confluence. The primary HNSCC cells both tumor and stromal, were used for the fabrication of heterotypic 3D bioprinted constructs.

Primary HNSCC tumor cells once confluent, were harvested for the development of 3D *in vitro* models. For 3D bioprinted constructs, cells were embedded in a bioink at a concentration of 5×10^6 cells/mL, while for 3D spheroid models, 21,000 cells were seeded per spheroid per well. The bioprinted constructs were cultured in 96-well flat-bottom plates, and the spheroids were grown in Nucleon Sphera 96-well ultra-low attachment (ULA) plates. Both models were maintained under identical conditions for 10 days before undergoing further functional analyzes.

To establish a HNSCC explant model, the tissue samples were obtained from eight consented patients diagnosed with HNSCC tumors. The patients gave informed consent (ethic vote 2019-528N; ethics committee II, Medical Faculty Mannheim, Heidelberg University). HNSCC samples used in this thesis were collected from various tumor localisations (5x oropharynx, 1x hypopharynx and 1x larynx) as listed in Table 9. The tissues were collected and transferred to the research laboratory within 30 mins after the surgical resection. The samples were transferred in a sterile standard procurement medium. The tissue procurement medium used consisted of Dulbecco modified Eagle's medium (DMEM) which was mixed with 1mL of puromycin 50mg/mL.

Table 9 HNSCC ex-vivo culture- patient cohort data

# Ex-vivo (n)	Age at initial diagnosis	Sex	Tumor localization	TPS score (%)	Growth media supplemented with (FBS/ hPL / StemMACS™ XF)
01	69	M	Oropharynx	-	FBS
02	59	M	Larynx	35	FBS
03	61	M	Oropharynx	5	FBS, hPL & StemMACS™ XF
04	62	M	Oropharynx	-	FBS & hPL
05	70	M	Oropharynx	10	hPL & StemMACS™ XF
06	58	M	Oropharynx	20	hPL
07	76	M	Larynx	-	StemMACS™ XF

08	63	M	Hypopharynx	-	hPL

2.2.2. 3D HNSCC model establishment

2.2.2.1. 3D model design

To develop a 3D bioprinted model, it is essential to design a reproducible 3D structure that aligns with the specific objectives of the study. The critical bioprinting parameters included cell density, growth media volume, growth factor concentration, hydrogel type, hydrogel concentration, hydrogel gelation temperature, print head and print bed temperatures, printing speed and pressure, layer number, printing pattern, infill density, nozzle/needle size, crosslinking methods, and post-print sample characterization protocols tailored to the system. [43-46, 59] Optimisation steps were aimed to create a highly reproducible, cell-friendly structure that promotes cellular growth, proliferation, and migration, as outlined in the step-by-step process depicted in Figure 4. [46]

It was crucial to design a structure that not only met the requirements for printability and reproducibility but also closely mimicked the *in vivo* tumor microenvironment. To achieve this, I initially focused on developing a homotypic model using HNSCC epithelial cells, allowing us to systematically refine the biofabrication parameters. For the preliminary design, a simple 3D cylindrical structure, measuring 3 mm in diameter and 0.6 mm in height (with an approximate volume of 4.2 μL), was designed using Fusion 360 software (Autodesk Inc.). The 3D structure, created in .stl format, was subsequently converted to gcode format for compatibility with the bioprinter. The final optimized bioprinting parameters are detailed in Table 10.

Table 10 Optimized bioprinting parameters for fabricating a 3D HNSCC model

Bioprinting parameters	Ranges tested	Optimized Value
NC- gelation temperature (℃)	20-26 ℃	26 ℃
GelMAA- gelation temperature (℃)		26 ℃ (GelMAA- in a temperature controlled printhead) *
Printing temperature (℃)		26 ℃ (R.T)
Print-head temperature (℃)		26 ℃ (R.T)
Print-bed temperature (℃)		10 ℃ (GelMAA bioink) *
Infill density (%)	60-90	75-85
Printing speed (mm/s)	2-6	3-4

Printing pressure	5-20	6-12
Number of layers	1-2	1
Printing pattern	Concentric, grid & honeycomb	Concentric
Crosslinking method		Chemical- $CaCl_2$
Needle/ Nozzle inner diameter (µm)	0.025-0.041	0.041
Growth media volume (µL)	50-200	200

**(as per the manufacturer's protocol)*

2.2.2.2. Bioink preparation

Two different tunicate-derived nanocellulose (NC)-based bioinks were used: TEMPO-NC: TTC- TEMPO-mediated oxidized NC in alginate and Carboxy-NC: CTC- Carboxymethylated NC in alginate respectively. They were compared with a gelatin-based bioink in alginate, GelMAA (Table 11). The NC hydrogels were combined with 3% (w/v) alginate dissolved in 4.6% (w/v) D-mannitol at a ratio of 2:1. The mixing step was carried out using luer-lock syringes connected by luer-lock connectors. The hydrogels in the luer-lock syringes were mixed up to 200 times to ensure homogeneity while avoiding the introduction of air bubbles. GelMAA was prepared following the manufacturer's instructions. Subsequently, a 1 mL mixture of TEMPO-NC, Carboxy-NC or GelMAA hydrogel were combined with HNSCC cells, re-suspended in 200 µL of media per 1 mL of bioink.

Initially, to define the cell density that is required to prepare the bioink, different cell concentrations were tested, specifically 1 × 10^5, 1 × 10^6, and 1 × 10^7 cells/mL of bioink. The cell-laden hydrogel mixture was gently homogenised using luer-lock syringes to ensure even cell distribution. After preparation, 1 mL of the bioink was loaded into bioprinting cartridges via luer-lock connectors and was prepared for bioprinting.

Table 11 Summarized differences between the TEMPO-NC, Carboxy-NC and GelMAA hydrogels used in this study

Properties	**TEMPO-NC** ***(TEMPO-mediated oxidized tunicate NC)*** [55, 65, 66]	**Carboxy-NC (*Carboxymethylated tunicate NC*)** [55, 65, 66]	**GelMAA *(Gelatin Methacrylate in sodium alginate)*** [67]
Functional groups	Hydroxyl groups of cellulose backbone partially substituted with	Hydroxyl groups of cellulose backbone partially substituted with	Amine groups partially modified with

	carboxyl groups (COOH) mixed with alginate.	**carboxymethyl** groups (CH_2COOH) mixed with alginate.	**methacrylate** groups in alginate.
Zeta potential	- 40.3 ~ - 57.2 mV (negatively charged nanofibrils) *	- 34.8 ± 2.9 mV (negatively charged nanofibrils) *	Not applicable
Endotoxin values	≤ 0.5 EU/m	≤ 0.5 EU/m	≤ 50 EU/m
Surface area	High	High	Depends on surface modified polymer
Viscosity	High	High	Low
Printability	High (even at 0.5mL bioink used)	High (even at 0.5mL bioink used)	Low or poor (<1mL bioink used)
Shape fidelity	Favors for long term cultures	Favors for long term cultures	Varies based on cell conc. and bioink formulation
Properties	Good drug-loading capacity, biocompatibility, & biodegradability and highly stable	Good drug-loading capacity, biocompatibility, & biodegradability and highly stable	Improvable by further surface modification to enhance drug-loading capacity, biocompatibility, biodegradability & stability
Application	In-vivo drug delivery, disease modelling, wound healing, tissue engineering	In-vivo drug delivery, disease modelling, wound healing, tissue engineering	Disease modelling, wound healing, tissue engineering

** The data on zeta- potential, and endotoxin of the NC-hydrogels were obtained from the product specification listed on the website of Ocean TUNICELL, Norway. The link to the description is mentioned in the appendix.*

2.2.2.3. Bioprinting

After preparing the bioink, the bioprinter was sterilized and calibrated with cartridges containing the respective bioinks (the calibration was performed following the instructions of the bioprinter). Following calibration, the cell-laden bioinks were bioprinted into cylindrical constructs and deposited into 96-well plates as per the optimized bioprinting parameters (refer to Table 10). Depending on the experimental conditions, a minimum of 3 and up to 48 bioprinted constructs were bioprinted. These constructs were then chemically crosslinked by adding $CaCl_2$ for 5 minutes, with two concentrations (50 mᴍ and 20 mᴍ) tested for optimal crosslinking. After 5 minutes, the crosslinking solution was aspirated, and 200 µL of the respective growth media cocktail was added to each well. The 3D bioprinted constructs were then cultured under sterile conditions in an incubator for 21 days, with 50% of the media being refilled every third day to support long-term cell viability and growth.

2.2.3. Xeno- free patient-derived 3D HNSCC explant model establishment

For the HNSCC explant model, the resected HNSCC tumor were washed twice with PBS. The tissues were then sectioned into 6-9 pieces of approximately 3 mm thickness each. One portion of the tumor section was immediately formalin-fixed (4% paraformaldehyde (PFA)) and paraffin-embedded, serving as the untreated primary control. The remaining tissue slices were cultured in a 12-well plate with ThinCert inserts, where they were placed at the air-media interface. The slices were cultured in growth media supplemented with various serum constituents (Table 12) and maintained at 37°C with 5% CO_2 in a humidified incubator, as previously described by *Affolter et al.* [68]

Table 12 Growth media cocktail constituents

Growth media	Base medium	Serum supplement	Antibiotics	Additional supplements
FBS media	DMEM + 2% L-glutamine	10% FBS	1% Pen/Strep	
hPL media	DMEM + 2% L-glutamine	12% hPL	1% Pen/Strep	0.2% heparin
StemMACS™ XF media	StemMACS™ MSC expansion media	-	-	1.4% StemMACS™ MSC expansion media XF supplement

The basal media was prepared by the addition of 2% L-glutamine and 1% penicillin/streptomycin to DMEM. Media variants were then created by adding specific serum supplements to the basal media (Table 12). The FBS media was formulated by adding 10% triple-filtered FBS.

The human platelet lysate (hPL) media was prepared by adding 12% platelet lysate and 0.02% heparin to the basal media. The hPL was derived from pooling two buffy-coat platelet concentrates, each generated from four platelet-rich buffy coats collected from healthy blood donors through the German Red Cross Blood Donor Service

Baden-Württemberg–Hessen, Mannheim. Platelet concentrates were then lysed through freeze-thaw cycles at −30°C and 37°C, followed by centrifugation at 2000 g for 20 minutes at room temperature. The supernatant was aliquoted and cryopreserved at −30°C. Prior to use, aliquots were thawed, centrifuged again at 2000 g for 10 minutes, and 12% of the resulting supernatant was added to the basal media. [69, 70]

In addition, a commercially purchased xeno-free medium (StemMACS™ MSC Expansion Medium XF) was employed as a control. StemMACS™ XF media was prepared according to the manufacturer's instructions by adding 1.4% of the StemMACS™ MSC Expansion Medium Supplement XF (human) to the corresponding basal media. The *ex vivo* tissue sections were fed with their respective growth media every second day during the 10- day culture period.

2.2.4. Radiochemotherapy (RCT) exposure to 3D HNSCC models

To investigate the functionality of the 3D bioprinted HNSCC model, the bioprinted constructs were subjected to a radiochemotherapeutic (RCT) treatment (Figure 4b). The bioconstructs were treated with cisplatin on day 6 and 8 at a concentration of 80 µM (Cis 80). In addition, they were exposed to fractionated irradiation (RT) on day 6, 7 and 8 at a dose of 2 Gy with 2 cm of polymethylmethacrylate slabs placed above and 5 cm below the 96-well plate to simulate clinical irradiation conditions. RT was delivered using a medical linear accelerator (Synergy; Elekta AB, Stockholm, Sweden) with a photon energy of 6 MV. The RCT protocol was tailored based on the standard treatment regimen for HNSCC patients and from the preliminary data from the established 2D and 3D spheroid HNSCC models. [63, 68]

As a comparative model to the 3D bioprinted model, 3D spheroids were generated with the primary HNSCC cells. Both models were exposed to cisplatin on days 6 and 8 (Figure 4c). Their comparative viability was monitored on day 10 using the chemiluminescence ATP-based viability assay kit.

In the HNSCC explant model, cisplatin at 80 µM concentration (Cis80) was administered on days 1, 3, and 7 during the culture period. [68] Additionally, three samples were subjected to RT starting on day 1 of culture, continuing for five days (on days 1, 2, 3, 6, 7). RT was delivered as described above.

2.2.5. Characterization

2.2.5.1. Cell viability analysis

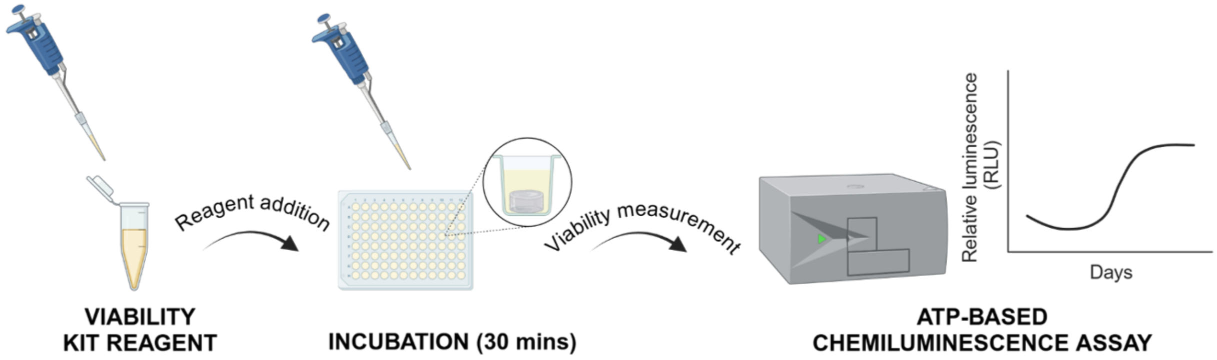

Figure 5 Schematic illustration depicting the process of cell viability analysis using an ATP-based chemiluminescence assay. *The workflow entails the addition of the viability kit reagent to the sample, followed by a 30 min incubation period. After incubation, the viability of the cells were measured by ATP levels as an indicator of metabolic activity. The results were plotted as relative luminescence units (RLU) over time. Created in Biorender.*

To investigate the metabolic activity/ viability of cells within the bioprinted constructs, an ATP-based chemiluminescence assay was employed using the 3D CellTiter-Glo® viability kit following the manufacturer's protocol. The bioprinted constructs were transferred to an opaque 96-well plate and washed three times with PBS, allowing a 5 mins resting interval between washes. Following the washing steps, 100 µL of the viability assay reagent was added to each well, and the plate was shaken for 5 mins to ensure even mixing. The constructs were then incubated at room temperature for 30 mins. Subsequently, luminescence was measured using a microplate reader to quantify cell viability (Figure 5). The viability measurements were taken at multiple time points: days 0, 3, 6, 12, 14, 16, and 21, to monitor cellular activity over the course of the experiment (for AIM 1) (Figure 4a). The relationship between cell number and RLU were established comparing 2D and 3D bioprinted models. For 2D, the cells were seeded in 96-well plates at a cell seeding density of 5,000, 10,000, 15,000, and 20,000 cells per well. For the 3D bioprinted model- the bioink was prepared at cell densities - 1×10^6, 2×10^6, 3×10^6, 4×10^6, and 5×10^6 cells/mL, thus corresponding to 4,200, 8,400, 12,600, 16,800, and 21,000 cells per bioconstruct or cells per well. The bioprinted constructs were crosslinked with 50 mm $CaCl_2$. The viability of both HNSCC models were assessed 24 hrs after the printing/ seeding. Whereas for AIM 2, the viability measurements were carried out on days 3, 6, 7, 8, and 10 (Figure 4b &c).

2.2.5.2. Histological studies (H& E staining)

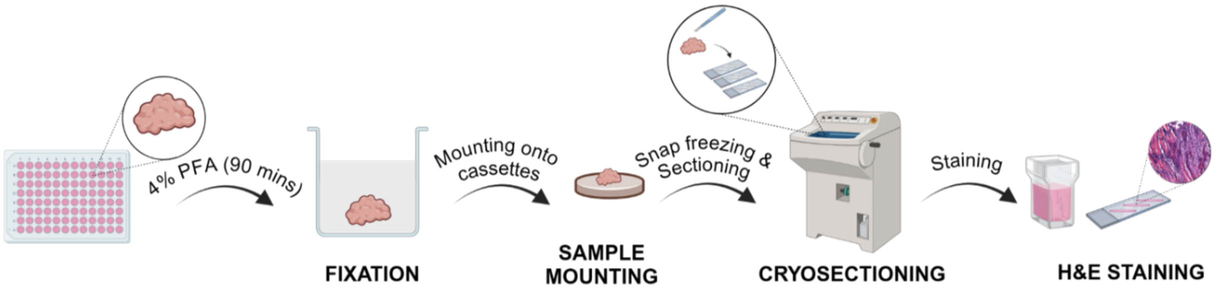

Figure 6 Schematic illustration depicting the process involved in staining HNSCC explants with hematoxylin and eosin (H&E). *Workflow for histological analysis involves- collection of tissue samples, formalin fixation followed by paraffin embedding and cryosectioning the mounted samples using a cryostat. This was followed by H&E staining of tissue sections, and microscopic examination of the stained slides for analysis. Created in Biorender.*

On day 10, the *ex vivo* tissue samples were harvested and immediately fixed in 4% PFA, followed by paraffin embedding in cassettes. Following fixation, the formalin-fixed paraffin-embedded (FFPE) blocks were sectioned into 5 μm-thick slices using a HISTOcut microtome. The tissue sections were then mounted onto adhesion slides (three sections per slide) and subsequently deparaffinized through three washes in xylene (with a rest time of 5 mins each), followed by an ethanol wash series (100%, 95%, 80%, and 70% ethanol, with 5 mins rest time). The slides were immersed in Mayer's hematoxylin solution for 10–15 mins, followed by a brief immersion in eosin solution for 30 secs. After staining, the slides were mounted with coverslips using ROTI®Mount mounting medium and imaged using an optical microscope (Carl Zeiss AG) (Figure 6).

2.2.5.3. Immunohistochemical staining (IHC)

IHC staining was performed using specific antibodies to evaluate the expression of Ki-67, PD-L1, and vimentin, which serve as indicators of cell proliferation, immune checkpoint inhibition, and epithelial-mesenchymal transition (EMT), respectively.

Figure 7 Schematic illustration depicting the process involved in staining HNSCC explants with immunohistochemical staining (IHC). *The workflow for IHC analysis involves- collection of tissue samples, formalin fixation followed by paraffin embedding and cryosectioning the mounted samples using a cryostat. This was followed by IHC staining of tissue sections with primary, and secondary antibodies. The samples were then counter stained with hematoxylin and microscopic examination of the stained slides was performed for analysis. Created in Biorender.*

As an initial step, the deparaffinized tissue sections were subjected to a demasking step using different buffers. Depending on the primary antibody, either citrate (for Ki-67 and Vimentin antibodies) or tris-EDTA- (for PD-L1 antibody) based buffer was employed. Following the demasking step, the slides were incubated in 7% hydrogen peroxide for 7 mins to block endogenous peroxidase activity and subsequently blocked with 10% normal sheep serum for 30 mins. The sections were then incubated overnight at 4°C with their respective primary antibodies: Ki-67 (1:200), PD-L1 (1:200), and vimentin (1:200), prepared in antibody diluent. After primary antibody incubation, the slides were treated for 30 mins with a biotinylated secondary antibody, either anti-rabbit multilink antibody (1:200) (Vimentin and Ki-67) or anti-mouse antibody (1:200) (PD-L1), depending on the primary antibody used. Then, the sections were subsequently treated with a streptavidin-biotin horseradish peroxidase complex for 45 mins. For detection, 3-amino-9-ethylcarbazole (AEC) was utilized, and substrate development was monitored microscopically. The slides were counterstained with hematoxylin, mounted with Permanent Mounting Media, covered with coverslips, and imaged using an optical microscope (Axiovert 25 CFL, Carl Zeiss AG) (Figure 7).

2.2.5.4. Immunofluorescence staining (IF)

To determine whether the cells in the various bioink constructs retained expression of their characteristic cell-specific markers, immunofluorescence (IF) staining was conducted. The epithelial marker E-cadherin, which is typically downregulated during epithelial-to-mesenchymal transition (EMT), was used as a marker for epithelial cells.

Cellular proliferation was assessed through Ki-67 staining, a nuclear protein expressed during the late G1, S, G2, and M phases of the cell cycle.

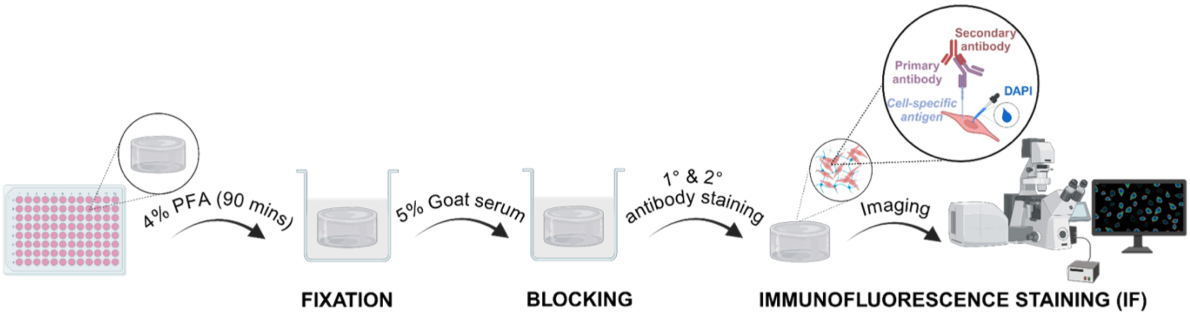

Figure 8 Schematic illustration portraying the step-by-step immunofluorescence (IF) staining process involved in staining 3D bioprinted HNSCC constructs. *The workflow for IHC analysis involves- collection of bioconstructs, formalin fixation followed by blocking with goat serum. This was followed by IF staining with primary, and secondary antibodies overnight. The samples were then counter stained with DAPI, and confocal microscopic examination was performed for analysis. Created in Biorender.*

The IF staining was performed on days 8, 16, and 21. Bioprinted constructs were fixed overnight in 4% paraformaldehyde (PFA) and subsequently permeabilized using an IF wash buffer. The IF buffer contains PBS, 500 mg BSA (0.1% w/v), Triton™ X-100 (0.2% v/v), and TWEEN® 20 (0.1% v/v). After permeabilization, blocking was performed with 5% normal goat serum (v/v). The constructs were then incubated overnight at 4-8°C with primary antibodies against E-cadherin (1:50) or Ki-67 (1:20). Following the incubation with primary antibodies, the constructs for E-cadherin expression analysis were washed three times with IF buffer and PBS and were stained with Alexa-488-conjugated secondary antibodies (1:200 dilution, anti-rabbit). The nuclear counterstaining was performed with DAPI for all the bioconstructs following a PBS wash (three times). After the nuclear staining, the constructs were washed three times with PBS with a rest time of 5 mins between every wash. 2% agarose was prepared to embed the constructs in 35-mm glass-bottom dishes containing PBS. The IF stained bioconstructs were imaged using a confocal laser scanning microscope (TCS SP8 upright, Leica), with a z-stack depth of 200 µm. Each sample was imaged in three distinct regions—representing the top, middle, and bottom sections—using z-stacks of 200 µm. For each condition, three biological replicates were analyzed (n = 3). The acquired images were processed and analyzed using ImageJ software (Figure 8).

The z-stack images were loaded into ImageJ, and the channels were split based on fluorescence assigned (Green- E-cad/Ki67; Blue- DAPI). The maximum projection was applied to generate a single composite image for each channel, after which the channels were merged. The fluorescent artifacts were removed through despeckling, and the images were iteratively processed to ensure accurate biomarker analysis. To assess the co-expression of Ki-67 and E-cadherin, the processed images underwent image thresholding for the DAPI (blue) and Ki-67/E-cadherin (green) channels. Following thresholding and noise reduction, both channels were combined using the image calculator tool to determine co-localization. The resulting co-localization image was further processed by applying image thresholding and converting it into a binary mask. These masks were then superimposed on the composite merged images, and the number of cells expressing both DAPI and Ki-67/E-cadherin were quantified. The percentage of cells expressing the respective biomarkers was calculated and graphically represented. The images presented in this thesis are derived from the mid-section of the constructs.

For Aim2, on day 10, the bioconstructs were processed for IF staining to determine whether the RCT treatment has an effect on proliferation (Ki-67) and epithelial marker expression (E-cadherin). Following the above-mentioned IF staining protocol, the bioconstructs from different conditions- negative/ control, cisplatin only (Cis80), irradiation only (RT) and combinational treatments (RCT) samples were examined for their relative biomarker expression analysis. Three samples per condition was used for IF staining procedure.

2.2.5.5. Scanning electron microscopy (SEM) of the 3D bioprinted constructs

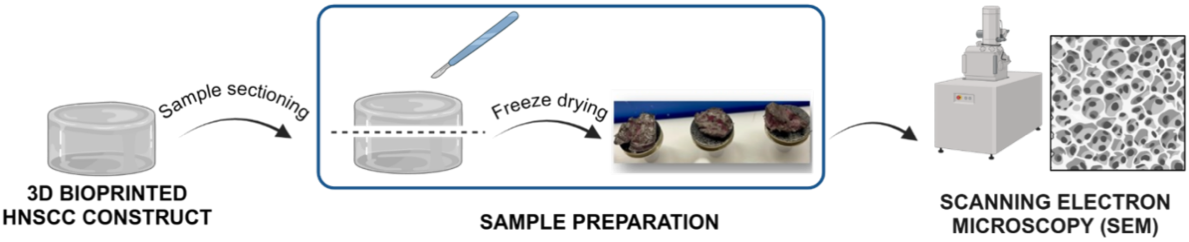

Figure 9 Schematic illustration portraying the methodology involved in scanning electron microscope (SEM) characterization of the 3D bioprinted HNSCC constructs. *The workflow for sample preparation and SEM imaging involved initial sample acquisition, sectioning and freeze drying*

of sample slices, placement and orientation of freeze-dried samples for imaging, followed by examination under SEM to analyze surface morphology and microstructural details. Created with Biorender.

Three different types of hydrogels were used- two were NC-based and one was a gelatin-based hydrogel. To investigate the difference between the three hydrogels, their hydrogel microstructure was examined using SEM. For SEM characterization, cell-free bioconstructs were prepared by casting the hydrogels onto a flat bottom 12-well plate (Corning) in the form of a cylinder and chemically crosslinked with 20mM $CaCl_2$ for 5 mins. Following the crosslinking step, the excess crosslinker was aspirated and HNSCC growth media was added to every well. The constructs were then maintained overnight in an incubator at 37 °C with 5% CO_2. The next day after incubation, the hydrogel constructs were sectioned using a scalpel, and subsequently lyophilized using a freeze-dryer (Alpha 3-4 LSC basic, Christ, Osterode am Harz, Germany) at a cold trap temperature of -105°C. The lyophilized hydrogel samples were then mounted onto a metallic stub using carbon tape and sputter-coated with a 6 nm layer of an 80/20 gold-palladium alloy (Leica Microsystems). The SEM micrographs were acquired using a Zeiss Leo 1530 instrument at the desired magnifications (100 μm and 20 μm), with scans conducted at an accelerating voltage of 2.0 kV. The porosity of the hydrogel samples was quantitatively analyzed using ImageJ software (Figure 9).

The average pore areas and their respective dimensions were determined manually through a re-iterative process. [71] First, the pixel size was calibrated, and thresholding was applied. Following the thresholding, image segmentation was performed wherein the threshold-corrected image was converted to a binary mask, and morphological filtering was applied to correlate the segmented mask with the original SEM image. This filtering process was repeated iteratively until the segmented mask closely matched the pore structures observed in the original SEM image. Upon validation of the segmented mask, quantitative data such as pore size, pore area, and the number of pores were extracted for statistical analysis.

2.2.5.6. Tumor proportion score (TPS) and immunoreactive score (IRS)

The tumor proportion score (TPS), which is used clinically for therapy decisions was calculated for PD-L1 expression (Table 9). TPS was determined as follows:

$$Tumor\ proportion\ score\ (TPS) = \frac{Number\ of\ Positively\ membrane - bound\ stained\ tumor\ cells}{Total\ number\ of\ vital\ tumor\ cells}$$

For the evaluation of Ki-67 and vimentin expression, immunoreactive scores (IRS) were assessed. The IRS assessed the IHC staining intensity and was adapted from Remmele and Stegner's method with scoring performed by two independent observers. [68] The IRS was determined using the following formula:

$$Immunoreactive\ scores(IRS) = Staining\ intensity(S.I) \times Percentage\ of\ positive\ cells(P.P)$$

2.2.5.7. Statistical analysis

Three independent experiments (n = 3), each performed in triplicate, were conducted. The data obtained were analyzed using either a two-tailed unpaired t-test or one-way/two-way analysis of variance (ANOVA), as appropriate for the specific experimental conditions. Results are presented as the mean ± standard deviation (SD), and statistical analyzes were performed using GraphPad Prism software (version 9.5.1.733; San Diego, CA, USA). A p-value of < 0.05 was considered statistically significant, with significance levels denoted as follows: $^{*}p < 0.05$, $^{**}p < 0.005$, $^{***}p < 0.0005$, $^{****}p < 0.0001$.

AIM 1: 3D BIOPRINTED HNSCC MODEL ESTABLISHMENT

3. RESULTS

3.1. Designing a 3D structure that mimics the native HNSCC TME

To build the model in a stepwise manner through a bottom-up method, I designed a 3D cylinder representing the observed tumor region in the primary tumor histopathology. The dimensions of the 3D cylinder were refined according to the experimental criteria, such as- material requirement for bioprinting and culture, imaging feasibility, number of replicates required, staining and fixation flexibility. The initially designed 3D cylindrical construct was modified from 5×1mm to 3×0.6mm (Figure 10).

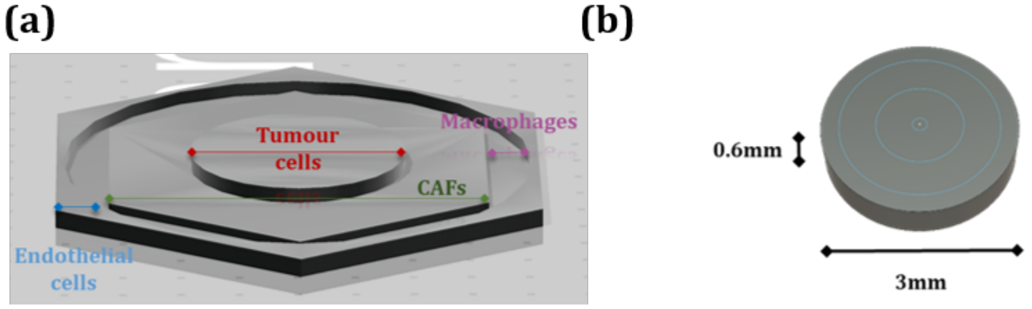

Figure 10 Comprehensive figure illustrating the modeling and development of a 3D bioprinted HNSCC model. *(a) 3D structure modeling based on TME cell distribution, adhering to biofabrication standards, with tumor cells at the centre, surrounded by cancer-associated fibroblasts (CAFs), immune cells (e.g., macrophages) near the tumor stroma, and vascular networks positioned farther from the tumor zone. (b) Fabrication of a preliminary tumor zone to optimize biofabrication parameters, using a 3D cylindrical structure (3 mm x 0.6 mm) as a scalable model for establishing the 3D bioprinted HNSCC system. Created in BioRender.*

3.2. Investigation and optimization of bioprinting parameters

Achieving a bioprinted construct with structural fidelity over a 21-day culture period, several key parameters need to be optimised. These include- printing temperature and speed, infill density, layer count, printing pattern, gelation time and temperature, nozzle diameter, and crosslinking method, as summarized in Table 11. [43, 45, 73] The initial assessment on bioinks after defining key printing parameters revealed that both the tunicate NC-based bioinks demonstrated ease of handling, high bioprintablility, and stability over prolonged culture. Further optimization was carried out as outlined below.

To closely mimic the native TME, it is essential to fabricate a 3D model that allows direct cell-to-cell interactions. In that case, cell density within the bioink (cells/mL) is a critical determinant for cell viability and shape fidelity. [43, 45, 73, 74] Thus, determining an optimal cell density that also allows bioink printability without affecting the bioink's rheological characteristics is a primary objective of this study.

Therefore, I tested varying cell densities - 1×10^5, 1×10^6, and 1×10^7 UM-SCC-11B cells/mL, thereby attempting to attain HNSCC bioconstructs with minimal/ shortest cell-to-cell distances. Then, the bioprinted HNSCC cell constructs with various cell densities were crosslinked with 50 mM $CaCl_2$. After 24 hours, the bioprinted HNSCC constructs were imaged using optical microscopy, and cell-to-cell distances within the constructs were measured at one single focal plane (Figure 11). A significant reduction in average cell-to-cell distance was observed between 1×10^5 and 1×10^6 cells/mL, while no major difference was detected between 1×10^6 and 1×10^7 cells/mL. While bioprinting with 1×10^7 cells/mL, the nozzles were clogged frequently which disrupted the printing and affected the total number of constructs obtained per mL of bioink. As the difference between 1×10^6 and 1×10^7 cells/mL samples were insignificant and for experimental ease, in terms of cell-to-cell distance and to facilitate experimental reproducibility, an intermediate cell density of 5×10^6 cells/mL were chosen as the optimal cell density for bioink preparation. Achieving a cell number of 1×10^7 cells while using primary HNSCC cells is challenging. Moreover, the primary cells cannot be passaged beyond 4-5 passages. Considering experimental reproducibility and the main intent to use primary cells for the optimised HNSCC bioprinted model, the cell density of 5×10^6 cells/mL was chosen. This density enhances cell-to-cell interactions while mitigating the additional nozzle clogging issues observed at 1×10^7 cells/mL.

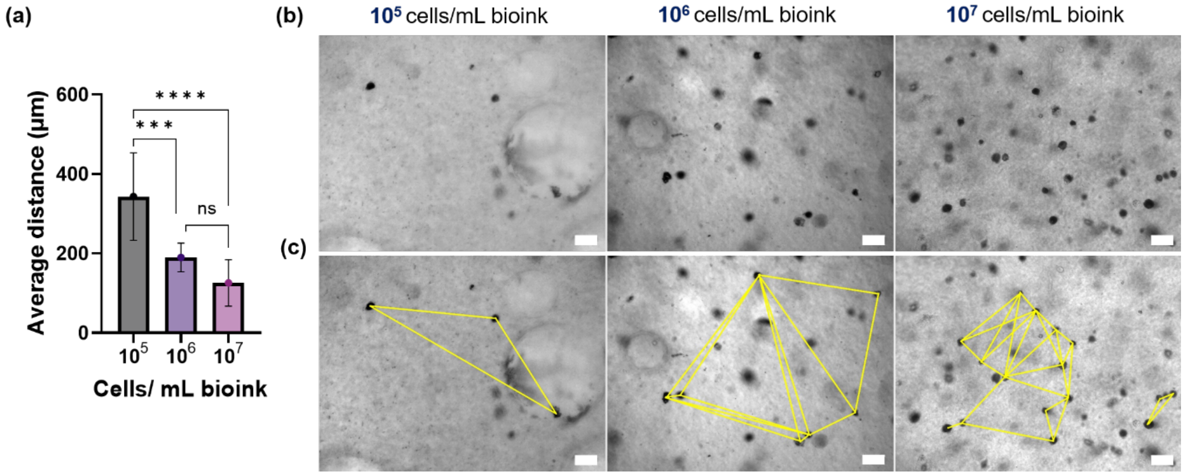

Figure 11 Optimization of cell density/mL in bioink preparation. *(a) Quantification of the average cell-to-cell distance between neighbouring cells, represented as mean ± SD. (b, c) Bright-field microscopic images of HNSCC cells within bioconstructs, with (c) highlighting the cell-cell distance measurement map. Data are based on three independent experiments with five technical replicates. Scale bar: 50 µm. Statistical analysis was performed using a 2-way ANOVA; ns – non-significant, ***$p < 0.0005$, ****$p < 0.0001$.*[75]

3.3. Bioprinting reduces but retains HNSCC- cell type specific metabolic activity/ viability

Having optimised the cell density/mL bioink, to document and establish the relationship between cell number and RLU, firstly, I bioprinted 3D HNSCC cells with different cellular densities per construct were bioprinted and compared to the conventional 2D seeded HNSCC cells with different cell densities per well as briefed in section 2.2.5.1.

The background luminescence signal was determined by measuring the luminescence of cell-free constructs. The RLU values of cell-free constructs were negligible in the range of 70-150 RLU, indicating minimal interference.

I plotted RLU against their respective cellular density i.e., cells/well. I observed a consistent linear relationship between RLU and cell density, which was true for both 2D and 3D models for all the three cell lines used (Figure 12). The luminescence in 3D constructs was 30.8% and 33.9% lower for UM-SCC-14C and UM-SCC-11B cells, respectively, compared to the 2D culture. For UM-SCC-22B cells, the luminescence signal was reduced by a 41.8% in 3D.

Additionally, the luminescence intensity differed for every cell type in both 2D and 3D models, thus indicating that there is a difference in ATP production in different cell types based on their tumor origin site. The ATP levels in UM-SCC-22B and 14C were much higher than the UM-SCC-11B cells in both 2D and 3D.

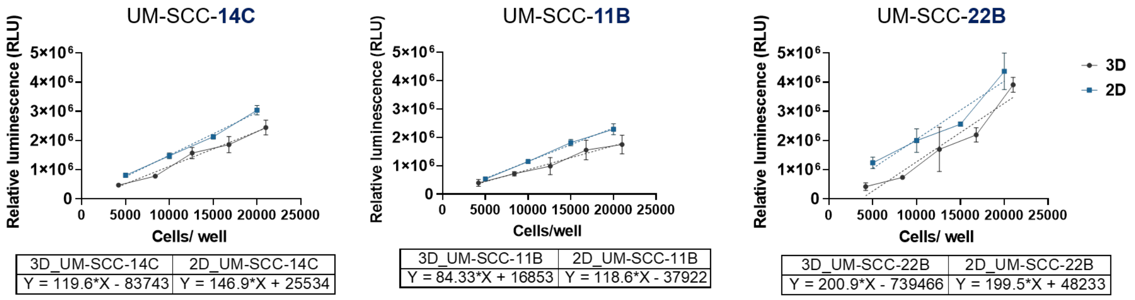

3D_UM-SCC-14C	2D_UM-SCC-14C
Y = 119.6*X - 83743	Y = 146.9*X + 25534

3D_UM-SCC-11B	2D_UM-SCC-11B
Y = 84.33*X + 16853	Y = 118.6*X - 37922

3D_UM-SCC-22B	2D_UM-SCC-22B
Y = 200.9*X - 739466	Y = 199.5*X + 48233

Figure 12 Bioprinting reduces but retains HNSCC cell-type-specific metabolic activity and viability. *The viability of HNSCC cells exhibits cell-line-specific behavior and follows a consistent pattern in both 2D and 3D cultures. Relative luminescence values (RLU) were plotted against cells per well and analyzed using a simple linear regression model:* ***UM-SCC-14C*** *(3D: y = 119.6x – 83743; 2D: y = 146.9x + 25534),* ***UM-SCC-11B*** *(3D: y = 84.33x + 16853; 2D: y = 118.6x - 37922), and* ***UM-SCC-22B*** *(3D: y = 200.9x – 739466; 2D: y = 199.5x + 48233). Data represent 12 samples per condition (n=12). Statistical analysis was performed using a 2-way ANOVA.*[75]

3.4. Carboxy-NC supports long-term HNSCC survival in 3D bioprints comparable to GelMAA, dependent on cell type and crosslinker concentration

TEMPO-NC, Carboxy-NC, and GelMAA bioinks were initially evaluated based on their usability and bioprinting performance. While TEMPO-NC and Carboxy-NC exhibited higher bioprintability under pre-optimized printing conditions at room temperature, GelMAA required meticulously controlled parameters, including gelation temperature, printhead and printbed temperatures, as well as specifically tailored bioprinting conditions such as pre-cooled plates, increased printing pressure, and higher printing speed. These modifications were distinct from NC-bioink printing conditions (Table 11). Despite these highly tailored bioprinting conditions, GelMAA demonstrated poor bioprintability, comprimising reproducibility of the bioprinted constructs compared to those printed using NC-based bioinks.

To further assess long-term viability and metabolic activity of the HNSCC cells, the bioprinted constructs were cultured for 21 days and monitored on days 0, 3, 6, 12, 16, and 21 to evaluate the effects of bioink type, cell line, and crosslinker concentration (Figure 13). To compare bioink efficacy and to understand the behavior of differently originated HNSCC cell types in different bioinks, the three HNSCC cell lines were bioprinted in TEMPO-NC, Carboxy-NC, and GelMAA bioinks (Figure 13a). Different patterns were observed on different days for different cell types in different bioinks. For UM-SCC-14C, a rapid decline in viability was observed in TEMPO-NC, with a slight recovery on D16 before a subsequent drop on D21. Meanwhile in Carboxy-NC, viability of UM-SCC-14C cells declined steadily until D12, after which cells proliferated, showing increased viability through D21, similar to GelMAA constructs. However, initial luminescence values (RLU) were significantly higher in GelMAA than in TEMPO-NC and Carboxy-NC (4×10^6, 3×10^6, and 1.8×10^6, respectively on D0).

UM-SCC-11B cells' viability also declined in TEMPO-NC without any significant recovery over the 21-day culture. In Carboxy-NC, a slight recovery was observed on D16 through D21. GelMAA bioconstructs showed an initial viability drop on D3, followed by a steady increase through D21. Initial RLU values were again roughly double in GelMAA for UM-SCC-22B cells compared to TEMPO-NC and Carboxy-NC bioconstructs. In UM-SCC-22B cell-laden constructs, viability linearly decreased until D12, then recovered on D16 and 21 to baseline levels. Carboxy-NC showed a contrasting profile, with increased viability on D3 and 6 followed by gradual decline, while GelMAA exhibited a biphasic response, with an initial decrease on D3 and 6, and recovery by D8, a drop on D16, and a final increase above baseline levels by D21.

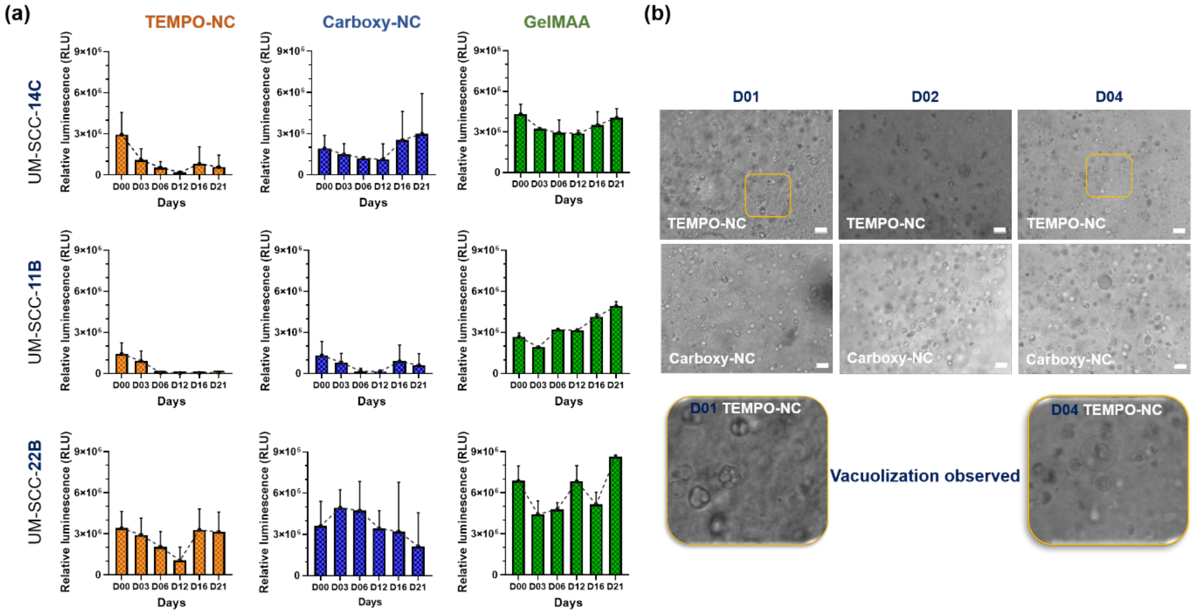

Figure 13 HNSCC cells in NC and GelMAA bioink constructs showed differing metabolic activity specific to the tumor origin. *(a) Viability/ metabolic activity of different HNSCC cell lines over 21 days in different bioinks crosslinked with 50 mM* $CaCl_2$ *and (b) UM-SCC-11B cells in the NC-bioink constructs indicating vacuolization on D01-04. The vacuoles formed have been zoomed and visualized below the microscopic images. N-3 independent experiments; n=3 samples per condition.*[75]

The data demonstrated a significant difference in the initial viability and proliferation of every HNSCC cell line. Moreover, this was observed consistently across the three bioinks used.

Upon lowering the $CaCl_2$ concentration from 50 mM to 20 mM, a significant increase in cell viability/ metabolic activity/ proliferation was observed (Figure 14a), especially in UM-SCC-11B bioconstructs. Additionally, HNSCC bioconstructs appeared to recover from printing-induced shear stress more rapidly, with viability improvements evident by D3. After D3, cells proliferated until D12, reaching a stationary phase by D21 for UM-SCC-14C and 11B constructs. In UM-SCC-22B bioconstructs, luminescence decreased until D12, after which cell proliferation resumed until D21. No significant viability differences were observed between Carboxy-NC and GelMAA bioinks when using the reduced $CaCl_2$ concentration. In TEMPO-NC constructs, crosslinked with 20 mM $CaCl_2$, HNSCC cell survival improved significantly over those crosslinked with 50 mM $CaCl_2$. With the reported differences between GelMAA and NC-hydrogels were less pronounced (e.g., UM-SCC-14C initial values were 4.5×10^6, 4×10^6, and 3×10^6 for GelMAA, Carboxy-NC, and TEMPO-NC, respectively). For UM-SCC-22B, a gradual decline in viability was noted until D12 in NC-hydrogels, with recovery on D16 and 21. In GelMAA, cell viability remained around the initial level.

Collectively, the current findings indicate that HNSCC cells from different tumor site respond uniquely in each bioink. In addition, it was also observed that the crosslinker concentration must be defined with respect to the cell line-since it could be cytotoxic to the cells (Figure 14b). Only Carboxy-NC crosslinked with 20 mM $CaCl_2$ supported a consistent 21-day increase in viability, indicating sustained proliferation. GelMAA consistently promoted long-term cell survival and proliferation across all crosslinker concentrations (Figure 14b).

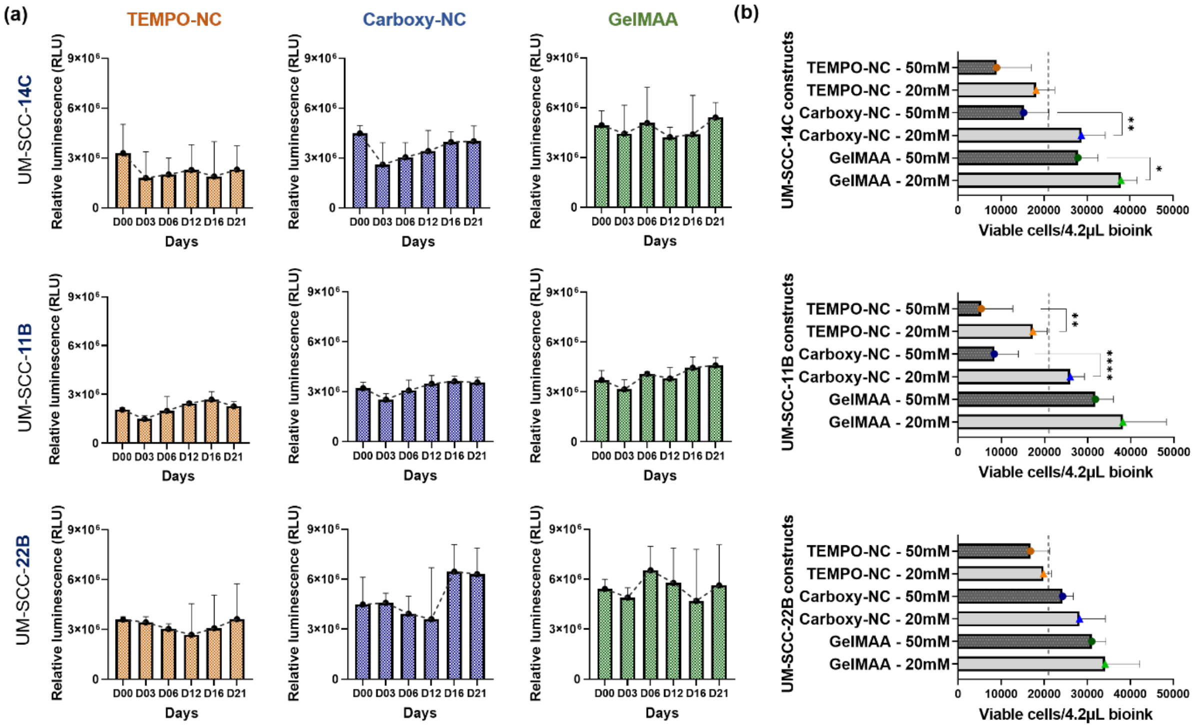

Figure 14 ***Carboxy-NC enables long-term HNSCC survival in 3D bioprinted constructs, showing viability behavior similar to GelMAA and varying by cell line.*** *(a) HNSCC cell viability over 21 days in bioinks crosslinked with 20 mM $CaCl_2$. (b) Collective viability of HNSCC cells in different bioinks after 21 days, assessed across two crosslinker concentrations- 50mM vs 20mM $CaCl_2$. The vertical line represents the initial bioprinted cell count (21,000 cells per 4.2 µL bioink). Data are based on N=3 independent experiments with n=3 samples per condition. Statistical analysis: 2-way ANOVA, *$p < 0.05$, **$p < 0.005$, ***$p < 0.0005$, ****$p < 0.0001$.*[75]

In order to determine whether this trend of Carboxy-NC bioink to be better compatible to GelMAA than TEMPO-NC, was cell-specific, MCF-7 cell line was bioprinted in all the three bioinks- TEMPO-NC, Carboxy-NC and GelMAA (Figure 15). Upon investigating the viability/ metabolic activity, MCF-7 cells exhibited a 70.2% lower luminescence signal in 3D bioprinted constructs compared to 2D culture (Figure 15b).

In addition, MCF-7 bioconstructs in different bioinks, followed a similar viability/ proliferation pattern like to the HNSCC bioconstructs (Figure 15a and c). In TEMPO-NC and Carboxy-NC, MCF-7 cells had reduced viability by D3 and 6, partially recovered by D12, but then declined steeply in TEMPO-NC and gradually in Carboxy-NC until day 21. In contrast, MCF-7 cells in GelMAA displayed a continuous rise in metabolic activity starting from D3, with GelMAA supporting higher viability than Carboxy-NC and TEMPO-NC, consistent with observations in HNSCC lines. Importantly, the viable cell count of MCF-7 cells in all three bioinks was approximately double than the numbers observed in HNSCC constructs (Figure 15c).

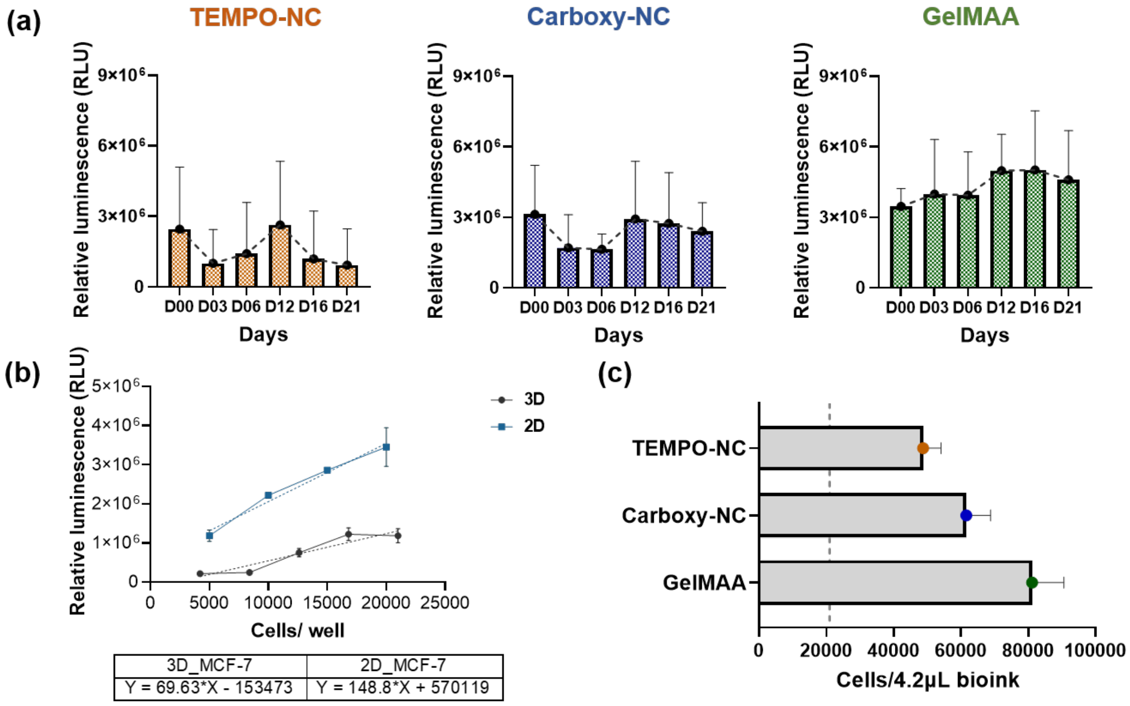

Figure 15 ***Carboxy-NC enables long-term MCF-7 cell survival in 3D bioprinted constructs, comparable to GelMAA, with viability dependent on the cell line similar to HNSCC bioconstructs.*** *(a) Viability of MCF-7 cells over 21 days in bioinks crosslinked with 20 mM* $CaCl_2$*. (b) MCF-7 cell viability exhibits a similar pattern in 2D and 3D cultures, with linear regression equations: 3D (y = 69.63x – 153473) and 2D (y = 148.8x + 570119). (c) Comparison of MCF-7 viability in different bioinks at the end of 21 days. The vertical line represents the initial bioprinted cell count (21,000 cells per 4.2 µL bioink). Data are based on N=3 independent experiments with n=3 samples per condition. Statistical analysis: 2-way ANOVA,* $*p < 0.05$, $**p < 0.005$, $***p < 0.0005$, $****p < 0.0001$.[75]

3.5. Microstructural analysis of hydrogels revealed variations in pore size, which are correlated with the different cell distribution patterns

In comparison to TEMPO-NC bioink constructs, Carboxy-NC bioink constructs demonstrated improved support for the survival of both HNSCC and breast cancer cells, revealing an equivalent performance to that of GelMAA. It was hypothesized that different hydrogel microstructures may have contributed to differing cell numbers/ proliferation. To investigate this, I performed scanning electron microscopy (SEM) in collaboration with the group of C. Selhuber to visualize TEMPO-NC, Carboxy-NC, and GelMAA hydrogels crosslinked with 20 mM $CaCl_2$ (Figure 16a and c).

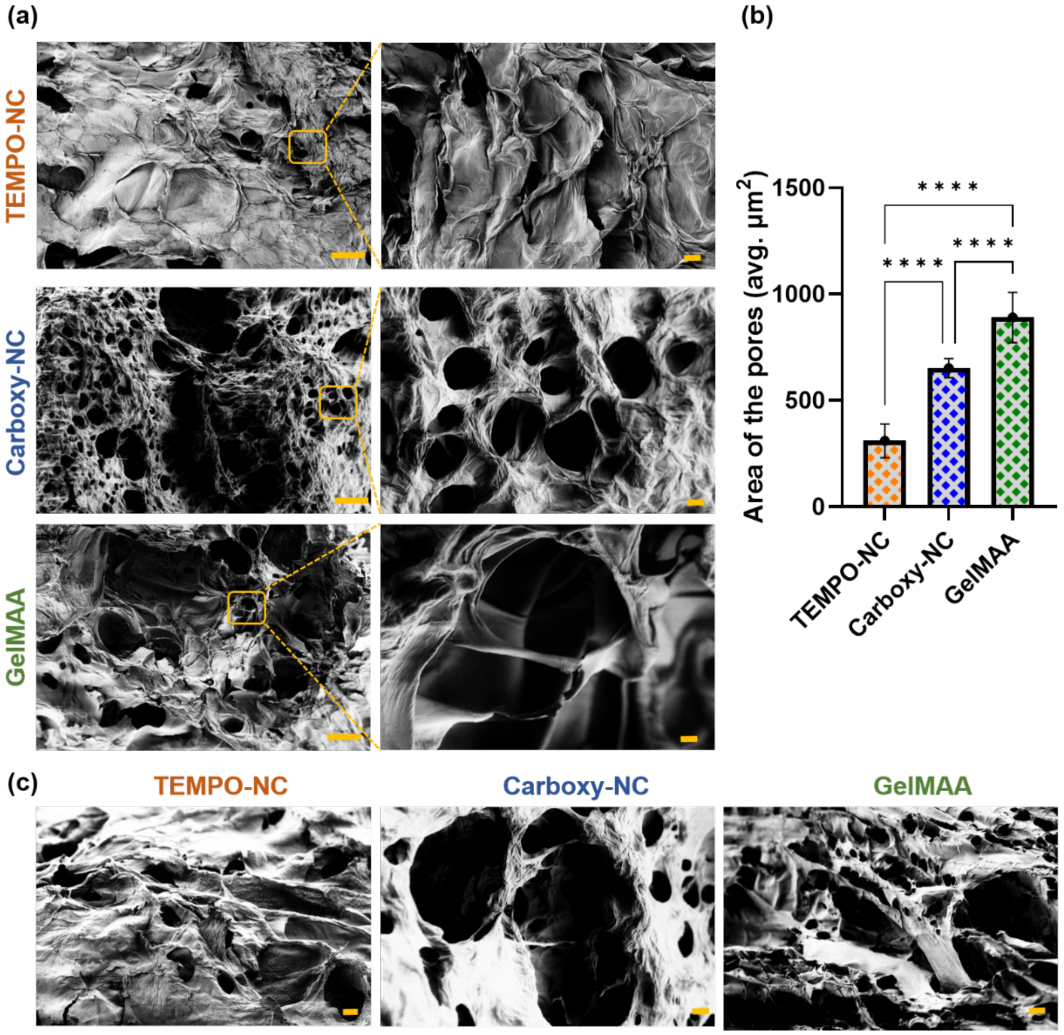

Figure 16 Microstructures of TEMPO-NC, Carboxy-NC, and GelMAA hydrogels crosslinked with 20 mM $CaCl_2$, visualized using scanning electron microscopy (SEM). *(a) The microstructure of all the hydrogels with a certain area zoomed in is presented. Left column: Scale bar = 100 µm; Right*

*coloumn: Scale bar = 20 µm. (b) Quantitative analysis of the average pore area in the three hydrogel types, performed using ImageJ. Data are based on n=3 technical replicates per condition and ROI=3 per sample. Statistical significance: 2-way ANOVA, ****p < 0.0001. (c) Hydrogel microstructure of all three hydrogels showcasing unique areas observed after SEM imaging. Scale bar = 20 µm.*[75]

The SEM analysis revealed that Carboxy-NC and GelMAA hydrogels exhibited an open-pore structure with smooth surfaces, whereas TEMPO-NC hydrogels were characterized by a flat, rough surface and predominantly closed pores (Figure 16a, c and Figure **17**a).

The closed pores in TEMPO-NC hydrogels were exceedingly narrow, which could potentially restrict cell migration, thus promoting higher number of cell cluster formation. Moreover, the higher surface roughness observed in TEMPO-NC hydrogels may hinder cell growth, proliferation, and migration, thereby explaining the slower increase in cell viability in TEMPO-NC constructs (Figure 17a). [76] Meanwhile, TTC only and CTC only micrographs illustrate the presence of a relatively higher number of open pores in comparison to TEMPO-NC and Carboxy-NC (Figure 17b, Figure **16**a and c). CTC only constructs seemed to possess the highest number of open pores. This in turn hints that the presence of alginate might have altered the hydrogel microstructure.

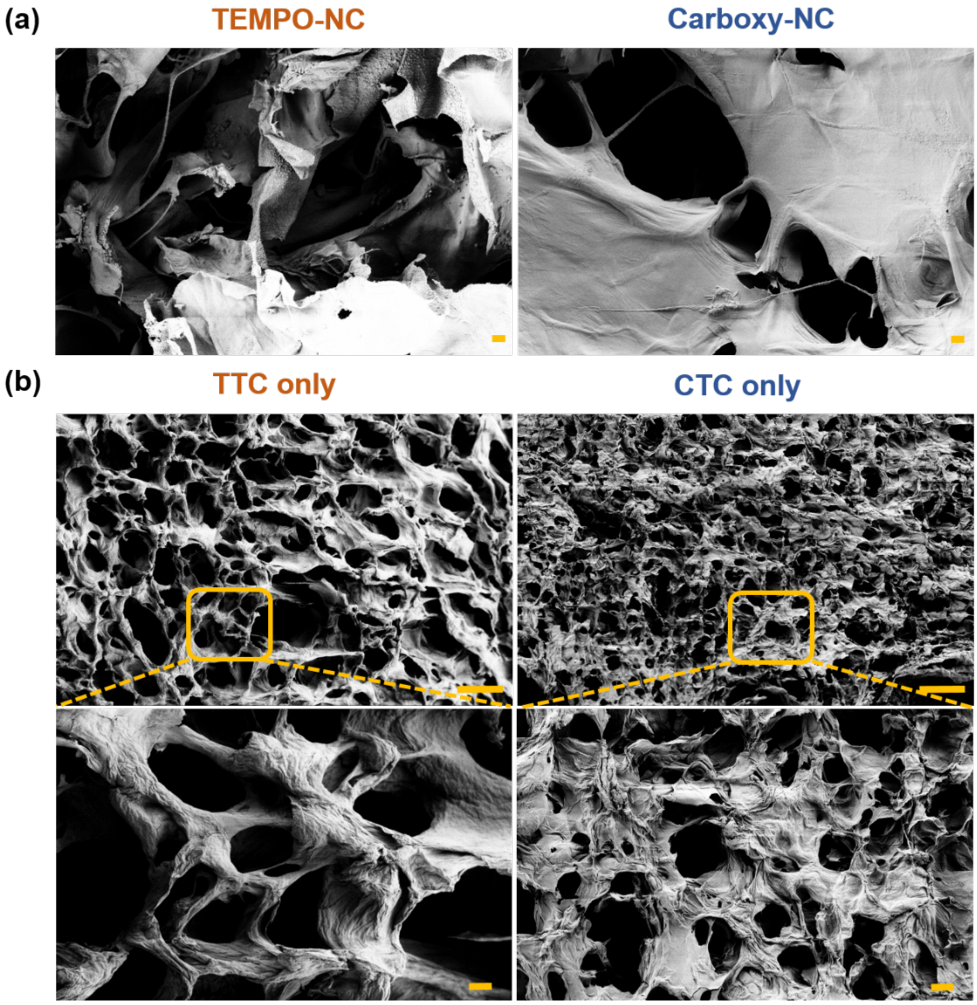

Figure 17 Microstructures of TEMPO-NC, Carboxy-NC, GelMA, TTC-only, and CTC-only hydrogels. *The hydrogels, crosslinked with 20 mM $CaCl_2$, were examined using SEM to visualize their microstructures. Representative images are shown from n = 3 technical replicates per condition. Scale bars: 20 μm for (a) and (b) zoomed-in images; 100 μm for (b) zoomed-out images.*

Quantitative analysis of the average pore area revealed significant differences among the hydrogels, measuring 310 μm² for TEMPO-NC, 652.7 μm² for Carboxy-NC, and 890 μm² for GelMAA (Figure 16b). These pore size variations correlated well with the observed cell viability results (n= 3 technical replicates per condition) (Figure 14 and Figure **15**).

3.6. HNSCC cells proliferate in the bioinks and maintain epithelial phenotypes

The viability results demonstrate that both the HNSCC and breast cancer cells survive in all the tested bioinks. However, the viable cell number at the end of the culture was visibly much lower than anticipated (Figure 14b). The UM-SCC-22B cells in Carboxy-NC and GelMAA proliferated more than the initial bioprinted cell number. Hence it becomes crucial to investigate whether the cells within the bioconstructs can proliferate after they overcome the initial bioprinting related shear stress.

Therefore, IF staining of the well-established proliferation biomarker- Ki-67 on UM-SCC-22B cell-laden different bioink constructs was performed. The bioconstructs were tested for Ki-67 expression on days 8, 16 and 21. On D8, the UM-SCC-22B cell-laden bioconstructs were positive for Ki-67 biomarker within all bioink constructs, with proliferation rates of 46.75%, 50.91%, and 52.94% in TEMPO-NC, Carboxy-NC, and GelMAA constructs, respectively (Figure 18). However, the proliferation rate declined progressively over time, with a prominent decrease from D16 to D21, particularly in TEMPO-NC bioconstructs, which exhibited a 41.02% reduction in proliferating cells by D21. Comparatively, the decline observed in Carboxy-NC and GelMAA bioconstructs was 24.23% and 16.34%, respectively and not as prominent as in TEMPO-NC constructs.

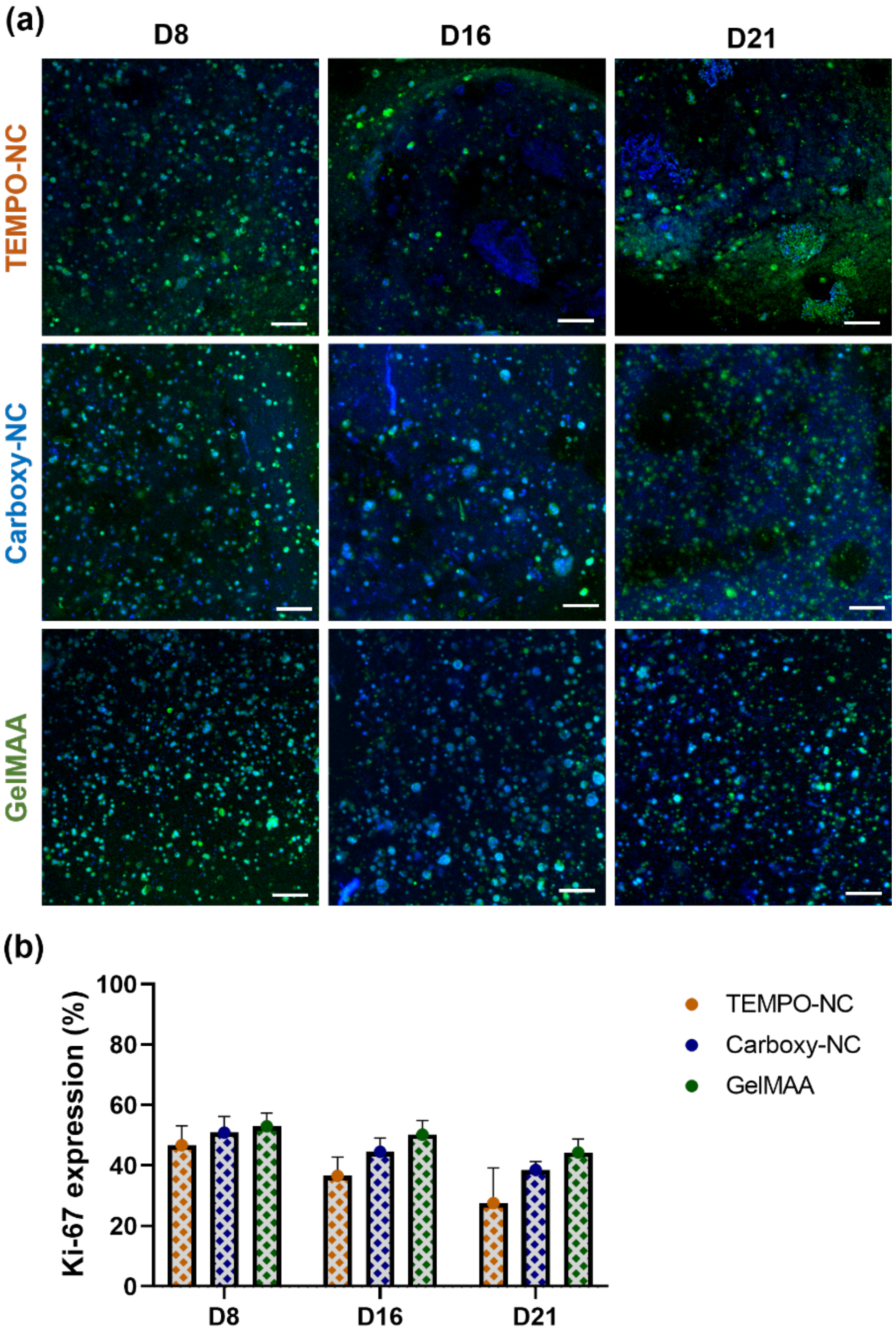

Figure 18 UM-SCC-22B cells proliferate and form defined, similar- sized clusters predominantly in Carboxy-NC and GelMAA hydrogels. *Bioconstructs underwent immunofluorescence (IF) staining for Ki67, followed by confocal imaging (a) (Ki-67; DAPI). The percentage of proliferating cells within different bioink constructs was quantified from the confocal images using ImageJ (b). Representative images are shown from n = 3 independent experiments with 3 samples per condition was considered for image analysis with ROI=3 per sample. Scale bar: 100 µm.*[75]

3D bioprinted models could in principle replicate the *in vivo* characteristics maintaining their cell-specific epithelial phenotype, thus allowing to study epithelial-mesenchymal transition (EMT). [77] To assess the epithelial phenotype preservation, UM-SCC-22B constructs were stained for E-cadherin (E-cad) - a hallmark epithelial biomarker on D08, D16, and D21 (Figure 19).

Quantification of E-cad positive cells in the bioconstructs revealed that on D8, 53.55%, 62.24%, and 70.98% of cells expressed E-cad in TEMPO-NC, Carboxy-NC, and GelMAA bioinks, respectively (Figure 19c). A significant difference was noted between TEMPO-NC and GelMAA constructs. Over time, E-cad expression decreased in 3D bioconstructs. Aligning the experimental timeline, E-cad expression was assessed in 2D cultures on day 3, considering that bioconstructs typically recover from bioprinting stress around day 6. Since IF staining was performed on bioconstructs two days post-recovery (day 8), a similar approach was applied to 2D cultures. Thus, two days after seeding, on day 3, IF staining was conducted to investigate E-cad expression in 2D cultures. While in 2D, most of the UM-SCC-22B cells expressed E-cad on day 3 (Figure 19b).

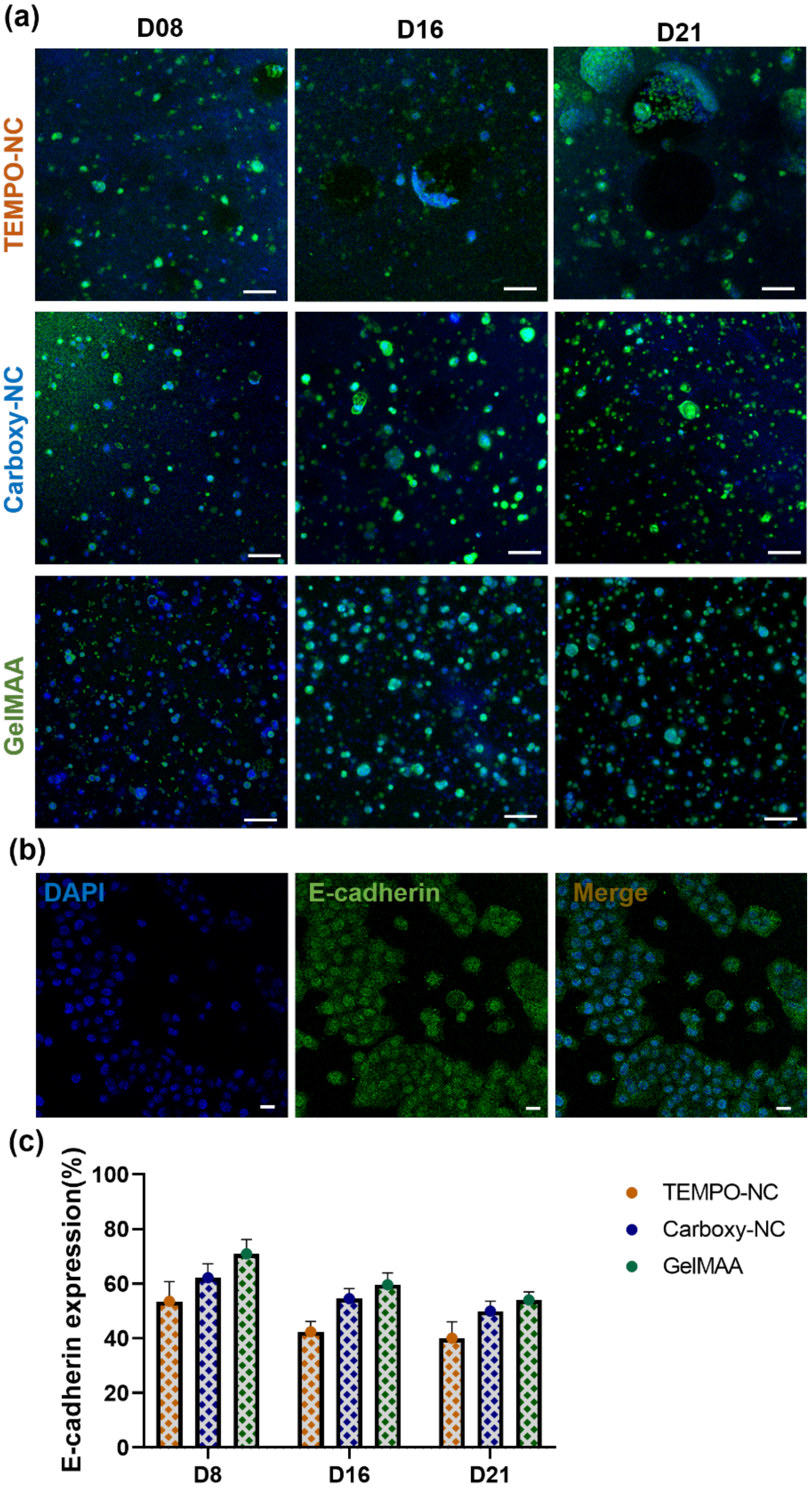

Figure 19 UM-SCC-22B cells form defined, similar sized clusters predominantly in Carboxy-NC and GelMAA hydrogels maintaining their typical epithelial characteristics. *UM-SCC-22B cells in both 3D bioprinted cultures on days 8, 16 and 21 (a) (scale bar: 100 µm) and 2D cultures on day 3 (b)*

(scale bar: 50 µm) were stained for E-cadherin, an epithelial biomarker (Ki-67and DAPI). The percentage of cells expressing E-cadherin in different bioink constructs was quantified from confocal images using ImageJ (c). Representative images are shown from n = 3 independent experiments with 3 samples per condition was considered for image analysis with ROI=3 per sample. [75]

Ki-67 and E-cad IF demonstrated distinct cell-distribution patterns across all bioinks throughout the culture period (Figure 18a and Figure 19a). D16 and D21 TEMPO-NC bioconstructs had large cell clusters along with cell-free zones distributed randomly. Contrastingly, Carboxy-NC and GelMAA bioconstructs illustrated an alike pattern with cell clusters distributed uniformly. Also, the clusters contained 3-8 cells each on D16 and D21 whereas the clusters in TEMPO-NC contained more than 15 cells with no uniformity. These findings fit well with the SEM data demonstrating that all the hydrogels possessed distinct microstructures (Figure 16). Particularly TEMPO-NC, exhibited large surfaces with closed pores- structural features that may mimic 2D culture surfaces, thus supporting a monolayer-like cell growth patterns rather than true 3D proliferation.

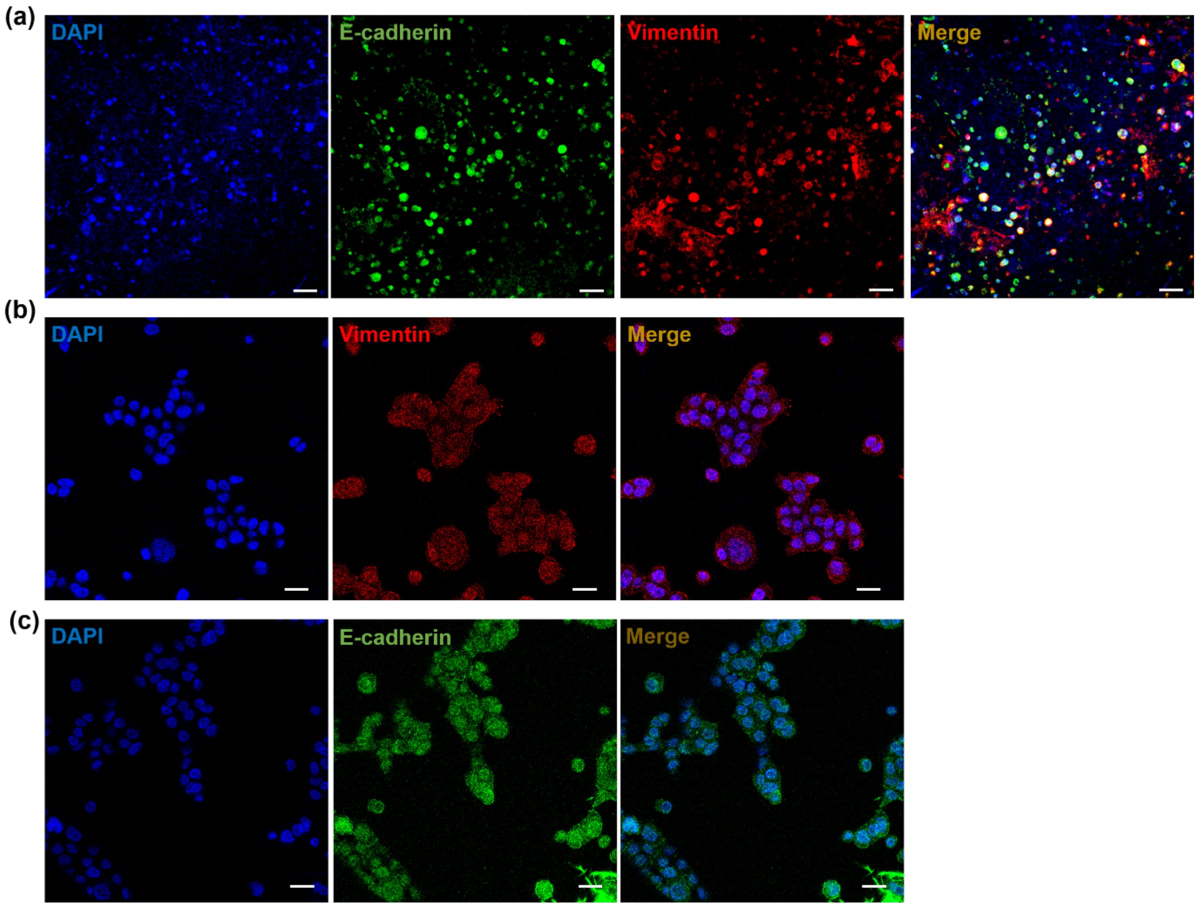

Figure 20 UM-SCC-22B cells in Carboxy-NC bioink constructs tested positive to vimentin (EMT marker) and E-cadherin in both 3D (a) and 2D (b&c) cultures. *(E-cadherin, Vimentin and DAPI). (Scale: 100 µm (a); 50µm (b))* [75]

To further investigate the observed decline in E-cadherin expression across all hydrogels, UM-SCC-22B HNSCC bioconstructs in Carboxy-NC bioink were stained for the epithelial-to-mesenchymal transition (EMT) marker vimentin (Vim) (Figure 20a). Triple IF staining revealed that not all cells co-expressed DAPI, E-cadherin, and Vim, indicating that only a subset of cells was undergoing EMT. To assess vimentin expression in 2D cultures, UM-SCC-22B cells were stained via IF (Figure 20b). In 2D *in vitro* culture, nearly all cells were positive for vimentin expression, suggesting a more uniform EMT phenotype under these conditions. In 2D *in vitro* culture, nearly all cells were positive for E-cad expression (Figure 20c).

3.7. HNSCC stromal cells express higher viability in TEMPO-NC while epithelial cells express higher viability in Carboxy-NC

The next step in the modelling of a 3D bioprinted model for HNSCC was to enhance the physiological relevance of the TME by incorporating multiple cell types. As an initial step, fibroblast cells were integrated into the model to mimic the stromal components of the TME.

A multicellular heterotypic 3D construct was designed with fibroblast-enriched stromal regions surrounding epithelial/tumor zones (Figure 21a). Adapting the already existing 3D construct design, for the co-culture of two cell types, the 3× 0.6 mm 3D cylindrical structure was expanded to a 3D cylinder with the following dimensions: 5 mm in diameter and 1 mm in height. To facilitate direct tumor-stromal cell interactions both within and between layers, the construct was designed with two distinct layers: **layer 1-** tumor cells were positioned centrally, surrounded by fibroblast/stromal cells along the periphery; **layer 2**- the arrangement was reversed, with stromal cells at the center and tumor cells along the periphery. The construct was designed to ensure the maintenance of close cell-to-cell contact, thus promoting *in vivo*-like cellular proliferation, meanwhile preserving native like biochemical cues.

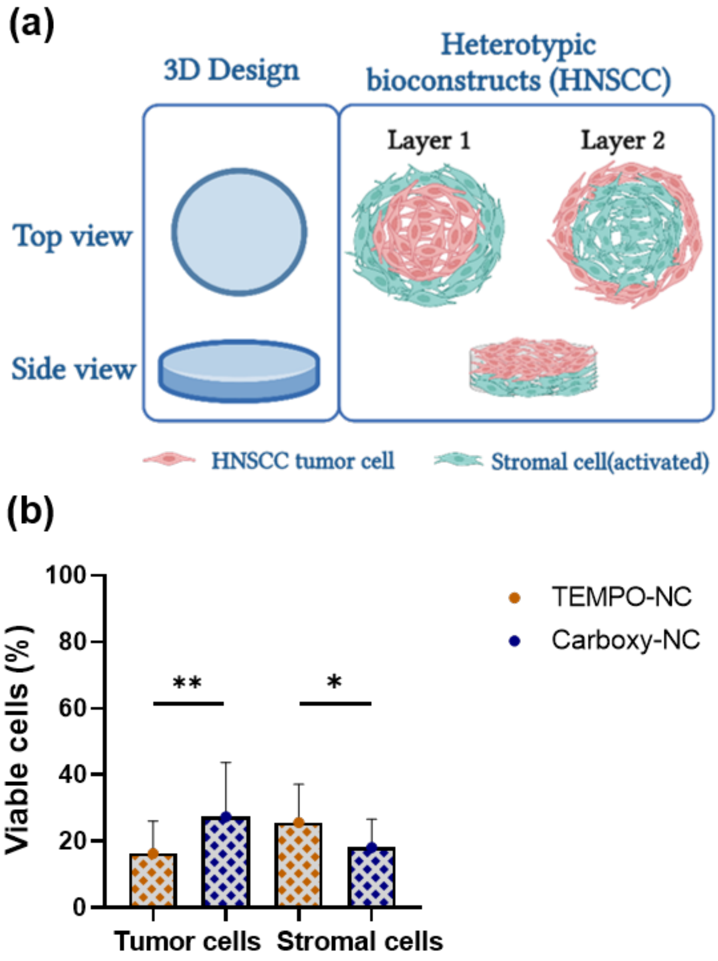

Figure 21 Heterotypic 3D bioprinted HNSCC model incorporating primary tumor and stromal cells within NC-based bioinks. *(a) The previously designed homotypic 3D structure was advanced to a heterotypic model by expanding the 3D cylinder's dimensions to 5 mm × 1 mm. The designed structure comprised two layers, where tumor and stromal cells were bioprinted alternately to allow for tumor-stromal cell interactions both within and between the layers. (b) Quantitative analysis of the heterotypic 3D bioprinted model using patient-derived HNSCC cells revealed a preference for Carboxy-NC bioink by tumor cells, whereas stromal cells exhibited a preference for TEMPO-NC bioink. Data represent N = 3 independent experiments with n = 3 samples per condition. Statistical analysis: two-way ANOVA;* *$^*p < 0.05$, $^{**}p < 0.005$.*

As a preliminary step towards the establishment of a heterotypic model mimicking the native TME, the compatibility of NC-based bioinks- specifically TEMPO-NC and Carboxy-NC- with primary HNSCC tumor and fibroblast cells was investigated. Heterotypic bioprinting was performed with primary tumor and stromal cells at cell densities of 5×10^6 and 1×10^6 cells/mL bioink, respectively, according to the specified 3D structural design (Figure 21a). The bioprinted constructs were cultured for 21 days, during which cell viability was assessed using Sytox live-dead staining. Fluorescence microscopy images were analyzed manually and quantified. The quantitative analysis of cell viability over the 21-day culture period revealed the cell-specific behavior of tumor and stromal cells cultured in TEMPO-NC and Carboxy-NC bioinks (Figure 21b). Stromal cells exhibited higher viability in TEMPO-NC bioink, whereas tumor cells showed a significant preference for Carboxy-NC bioink.

The viability of patient-derived HNSCC tumor and stromal cells was significantly influenced by the type of bioink used in the bioconstructs. Carboxy-NC bioconstructs supported the survival of 27.35% of tumor cells, whereas TEMPO-NC bioconstructs exhibited a lower tumor cell viability of 16.28%. Stromal cells demonstrated enhanced survival in TEMPO-NC bioconstructs, with 25.63% of cells remaining viable, compared to only 18.13% viability in Carboxy-NC bioconstructs. The obtained data confirms the importance of bioink selection in designing multicellular 3D bioprinted models, as the biochemical and structural properties of the bioinks differentially affect the viability and behavior of tumor and stromal cells.[23]

AIM 2: FUNCTIONAL VALIDATION OF THE ESTABLISHED 3D BIOPRINTED MODEL

3.8. RCT treatment reduces cellular viability significantly stronger than RT and Cis80 only treatments

Following the optimization of the 3D bioprinted model and confirmation of the bioink's cellular compatibility, the next phase focussed on assessing the functional response of the established 3D model. Clinically, advanced HNSCCs are predominantly treated with a combination of radiotherapy and chemotherapy. [6, 13] This therapeutic approach was replicated in the established 3D bioprinted model. At this stage, the homotypic 3D bioprinted HNSCC model was chosen to evaluate therapy responses.

The treatment regimen applied to the *in vitro* model was adopted from in-house protocols previously developed for 2D cultures, 3D spheroid models, and explant culture- HNSCC models. [63, 78] As an initial step, UM-SCC-22B cell-laden Carboxy-NC bioconstructs were subjected to fractionated irradiation (RT) over three days, followed by cisplatin-based chemotherapy for two consecutive days. Cisplatin was administered at a concentration of 80 µM (Cis80) to mimic clinically relevant dosing conditions (Figure 4b). The viability of the bioconstructs was investigated on D6, 8 and 10 of culture- 2hrs, 2days and 4 days after RCT treatment (Figure 22).

Two hours after Cis80 treatment, a 15.15% reduction in cell viability was observed, which progressed to 55.78% by D4. Meanwhile RT alone induced a modest 7.57% decrease in cell viability, which increased to 46.12% by D4. The combined radiochemotherapy (RCT) regimen resulted in a slightly higher initial decline of 22.71%, concluding in a 58.33% reduction in cell viability.

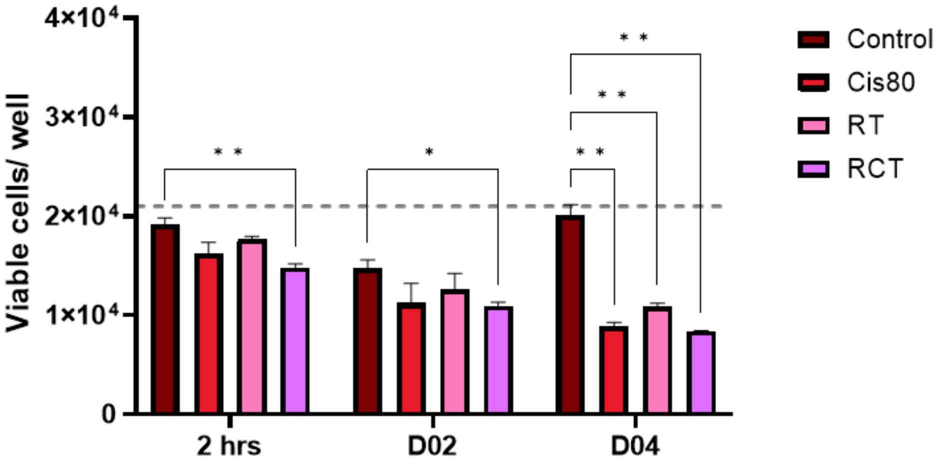

Figure 22 Functional validation demonstrates the efficacy of treatment modalities in 3D bioprinted HNSCC models. *Viability was measured at the indicated time points- 2hrs, D2 and D4 post-treatment, confirming the cytotoxic effect of RCT on the bioconstructs. The horizontal line represents the initial bioprinted cell number (21,000 cells/4.2 µL bioink). Data represent N = 3 independent experiments with n = 3 samples per condition. Statistical analysis: two-way ANOVA;* $^{*}p < 0.05$, $^{**}p < 0.005$, $^{***}p < 0.0005$, $^{****}p < 0.0001$. [75]

3.9. RCT reduced the proliferation rate and epithelial phenotype of HNSCC cells

IF analysis addressing Ki-67 and E-cadherin expression was performed on D4 post-treatment (Figure 23). The IF data indicated a substantial reduction in Ki-67 expression following combinational RCT treatment; however, the decrease was not statistically significant when compared to untreated controls (Figure 23b).

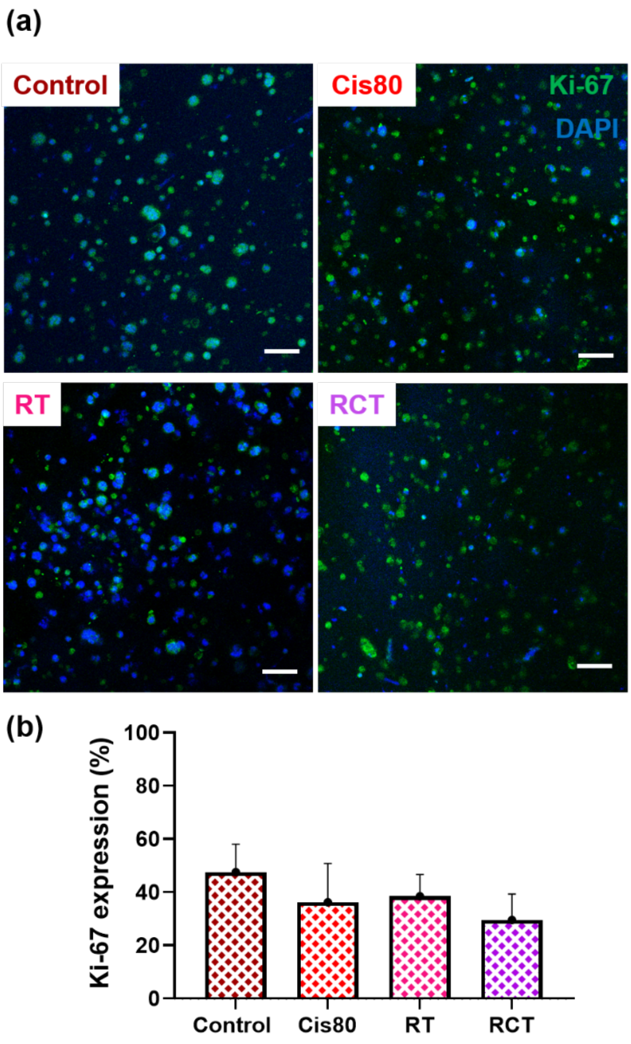

Figure 23 UM-SCC-22B Carboxy-NC bioconstructs exposed to RCT show a gradual reduction in proliferation rates. *(a) Immunofluorescence (IF) staining for Ki-67, a proliferation marker, was performed on differently treated UM-SCC-22B bioconstructs, followed by imaging using confocal microscopy (Ki-67 and DAPI). (b) Quantitative analysis of Ki-67 expression in the imaged constructs was conducted using ImageJ, and the results were presented as a bar graph. Data represent N = 3 independent experiments with n = 3 samples per condition. Statistical analysis: two-way ANOVA;* *$p < 0.05$, **$p < 0.005$, ***$p < 0.0005$, ****$p < 0.0001$. *Representative images are shown from n = 3 independent experiments with 3 samples per condition was considered for image analysis with ROI=3 per sample. (Scale bar: 100 µm)*

Ki-67 expression levels decreased in all treatment groups, with the most pronounced reduction observed in the RCT group with a 37.89% decline, followed by Cis80 and RT alone demonstrating a 23.82% and 19.15% drop respectively. Overall, the treatment itself accounted for 39.51% of total variance. Constructs treated with RCT displayed the clearest reduction in Ki-67 expression, while RT-treated constructs showed the least reduction (Figure 23b). This trend was consistent with the viability data presented in Figure 22, aligning with the cytotoxic and antiproliferative effects associated with RCT treatment.

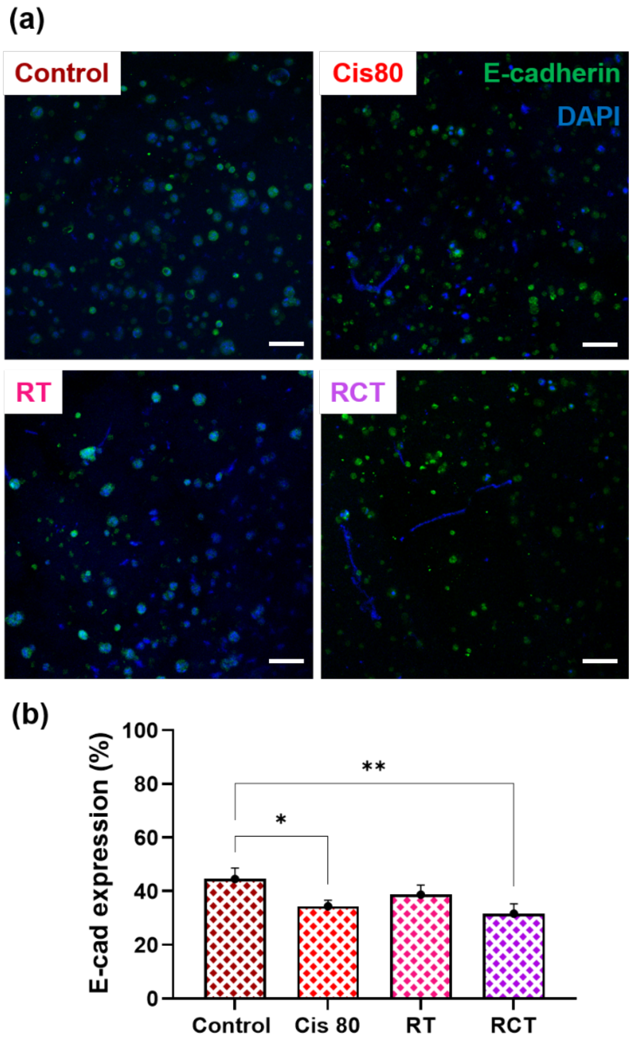

Figure 24 UM-SCC-22B Carboxy-NC bioconstructs exposed to RCT show a gradual reduction in E-cadherin expression rates. *(a) Immunofluorescence (IF) staining for E-cad, a characteristic epithelial biomarker, was performed on differently treated UM-SCC-22B bioconstructs, followed by imaging using confocal microscopy. (b) Quantitative analysis of Ki-67 expression in the imaged constructs was conducted using ImageJ, and the results were presented as a bar graph microscopy (E-cadherin and DAPI). Data represent N = 3 independent experiments with n = 3 samples per condition. Statistical analysis: two-way ANOVA; *p < 0.05, **p < 0.005, ***p < 0.0005, ****p < 0.0001. Representative images are shown from n = 3 independent experiments with 3 samples per condition was considered for image analysis with ROI=3 per sample. (Scale bar: 100 µm)*

At the morphological level, RT-treated cells appeared larger and more spherical in comparison to untreated controls. While a reduction in Ki-67-positive cells was evident in RT-treated constructs, the quantitative analysis suggested a delayed effectiveness of the treatment.

In contrast, bioconstructs subjected to RCT exhibited a markedly reduced number of proliferating cells. Morphologically, these constructs showed minimal clustering, a visible difference compared to the controls, which maintained prominent cellular aggregates. These observations confirm the enhanced antiproliferative effect of combinational RCT treatment.

As a continuation, the bioconstructs were investigated for their E-cadherin expression via IF staining (Figure 24). The quantitative analysis demonstrated that the RCT treatment had a stronger impact on the bioconstructs than the Cis80 and RT treatments alone (Figure 24b). While RCT treatment gave rise to a 29% decline in E-cad expression, Cis80 and RT treatments alone triggered a 22.74% and 13.13% E-cad expression decrease. RCT and Cis80 had a stronger effect than RT alone. Similar to the Ki-67-stained constructs, E-cadherin constructs appeared to project a similar trend (Figure 24a). Morphologically, the bioconstructs appeared alike in response to different treatments.

3.10. Chemotherapeutic treatment has a differential effect on the primary 3D bioprinted and 3D spheroidal systems

To enhance the clinical relevance of the model, patient-derived HNSCC cells from three independent donors were bioprinted in order to evaluate the model's potential as a high-throughput screening tool. The cells were obtained from distinct anatomical sites: the oral cavity, oropharynx, and larynx, ensuring representation of diverse tumor origins. Concurrently, a 3D spheroid model was fabricated using an in-house protocol to serve as a comparative benchmark. [78] Both 3D bioprinted constructs and spheroids derived from patient-derived HNSCC cells were subjected to Cis80 treatment (Figure 4c). Remarkably, the bioprinted constructs from all three patient-derived cell lines exhibited similar growth dynamics over the 10-day culture period (Figure 25), comparable to those observed in established cell lines (Figure 14 and Figure **15**).

Despite seeding equal cell numbers (both spheroids and bioconstructs), only 50% of the cells were successfully incorporated into the spheroids (Figure 25 and Figure **26**). Post-culture initiation, the viable cell counts in spheroids and bioconstructs differed significantly on day 3. The spheroid model accounted for an average of 9,836 viable cells per spheroid whereas the bioprinted model accounted for 19,186 viable cells per construct.

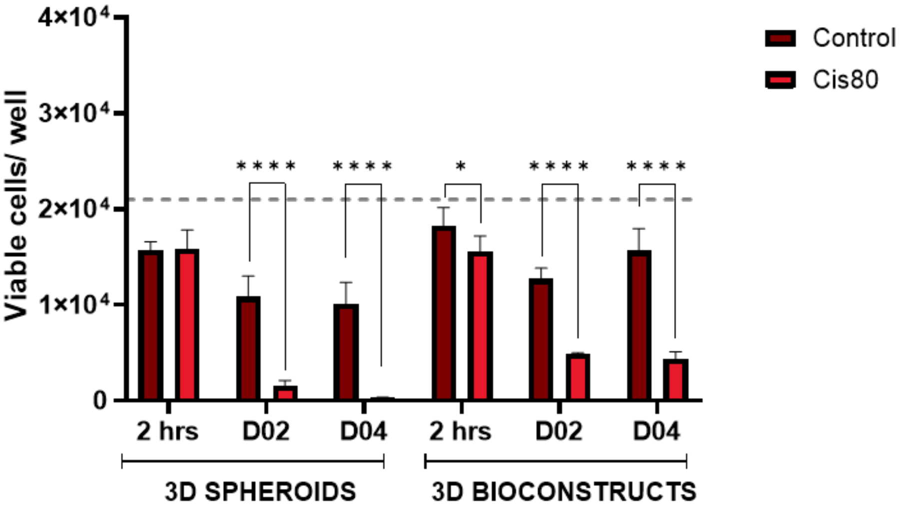

Figure 25 Functional validation demonstrates the efficacy of Cis80 in patient-derived 3D bioprinted HNSCC models compared to 3D spheroid models. *Viability was measured at the indicated time points- 2hrs, D2 and D4 post-treatment, highlighting the cytotoxic effect of cisplatin on the bioconstructs. The horizontal line represents the initial bioprinted cell number (21,000 cells/4.2 µL bioink). Data represent N = 3 independent experiments with n = 3 samples per condition. Statistical analysis: two-way ANOVA;* *$p < 0.05$, **$p < 0.005$, ***$p < 0.0005$, ****$p < 0.0001$. [75]

Upon evaluating the effects of Cis80 treatment, the 3D bioprinted model exhibited a measurable response as early as 2 hrs post-treatment, whereas the spheroid model demonstrated no observable effect at this early time point. Following three days of Cis80 treatment, cell viability in the spheroid system decreased by approximately 85.77% and 90.41% on days D2 and D4, respectively, compared to untreated controls. In contrast, the bioprinted models showed a more modest reduction in cell viability, with decreases of 61.68% and 71.99% collectively on D2 and D4 respectively.

In addition, differences in spheroid morphology were observed based on the donor origin. Spheroids derived from donor 3 (larynx origin) exhibited a dispersed, non-compact structure, whereas those from donor 1 (oral cavity origin) and donor 2 (oropharynx origin) displayed a more compact morphology (Figure Figure **26**a).

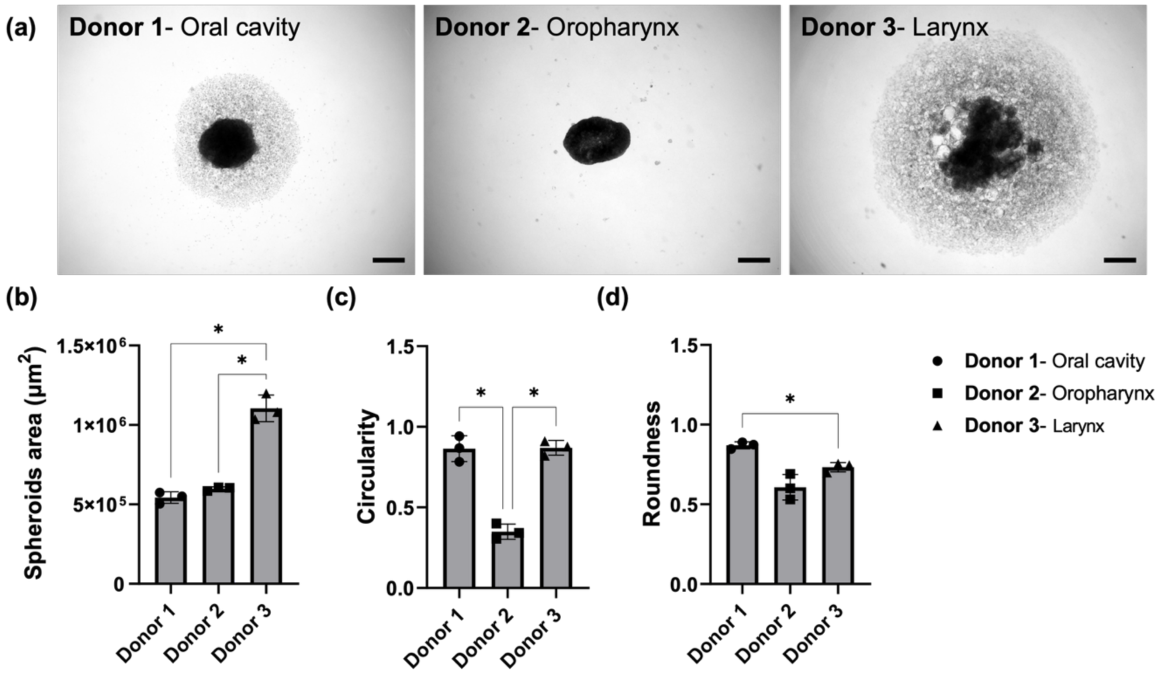

Figure 26 Patient-derived HNSCC cells from different tissue origins form spheroids of varying sizes. *(a) Microscopic images of D3 spheroids generated from tissues derived from three different donors. Quantitative analysis of the spheroids was performed based on (b) area, (c) circularity, and (d) roundness. Spheroids derived from Donor 3 exhibited the largest surface area (b). Spheroids from Donor 2 displayed an elliptical shape (c) and (d). There are variations in spheroid morphology (Scale: 1000 µm).* [75]

Quantitative analysis revealed that spheroids from donor 3 had a significantly larger surface area (1104,609 µm²) compared to spheroids from donor 1 and donor 2, which had surface areas of 543,048 µm² and 598,382 µm², respectively (Figure Figure **26**b). Furthermore, analysis of spheroid sphericity using circularity and roundness measurements demonstrated distinct morphological differences among donors. Spheroids derived from donor 2 exhibited an elliptical shape with a circularity of 0.034 units. In contrast, spheroids from donor 1 and donor 3 displayed a more rounded morphology, with circularities of 0.8643 and 0.8697, respectively (Figures Figure **26**c and d). While donor 3 spheroids had a relatively dispersed morphology, their compactness was visually lower in comparison to the other donor spheroids.

AIM 3: DEVELOPMENT OF XENO-FREE PATIENT-DERIVED 3D HNSCC EXPLANTS

3.11. HNSCC explants survived in xeno-free media expressing characteristic markers similar to FBS-grown tissues

To establish 3D *in vitro* models for HNSCC that are entirely xeno-free, an HNSCC explant model was developed evaluating its potential for culture in xeno-free media. The in-house established explant model in FBS-media was adapted for xeno-free growth media explant culture. Three different media conditions were used in this thesis: FBS-supplemented media, human platelet lysate (hPL)-supplemented media, and a commercial xeno-free medium optimized for mesenchymal stromal cells (StemMACS™ XF).

The initial critical culture parameters such as media volume, serum concentration, and media change frequency were systematically refined. Depending on the size of the procured tissue, the explants were assigned to either a single medium or multiple xeno-free media prone conditions for comparative analysis (Table 9). Following a 10-day culture period, histological evaluations were conducted and compared to native primary tissue to assess the reliability of the culture system (Figure 4d). The explants (*ex vivo* 03) enabled comparisons across three different media conditions (Figure 27). Among the total number of *ex vivo* samples collected from the patients, only 30% of the samples remained contamination free and utilized for further examination.

Although there was a relatively higher percentage of contamination in comparison to the 3D *in vitro* model, initial microscopic evaluation on the fidelity of patient-derived explant culture in xeno-free media reported successful sample survival in all three media. This demonstrated that HNSCC tissues can in principle be cultured under xeno-free conditions.

Subsequent analysis focused on evaluating relative proliferation rates and immune checkpoint marker expression. Histomorphological examination of H&E-stained sections revealed that while the tissues cultured in hPL and StemMACS™ XF media visually retained some structural characteristics comparable to those grown in FBS-supplemented media, noticeable differences were observed in cellular morphology and tissue organization. In addition, IHC staining results indicated varying degrees of immune checkpoint marker expression, with hPL and StemMACS™ XF media samples exhibiting reduced Ki-67 and PD-L1 expression when compared to their untreated, uncultured primary tumor counterparts (Figure 27). These findings suggest distinct media-dependent differences in tissue architecture and specific marker expressions.

Ki-67 expression was significantly lower in tissues cultured in StemMACS™ XF compared to those grown in FBS or hPL-supplemented media. Similarly, PD-L1 expression was consistently low in untreated primary tissues and similar to relatively low- leveled expression across samples cultured in all three media. Importantly, tissues cultured in StemMACS™ XF media displayed more pronounced morphological distortions, including necrotic features, compared to those in FBS or hPL media.

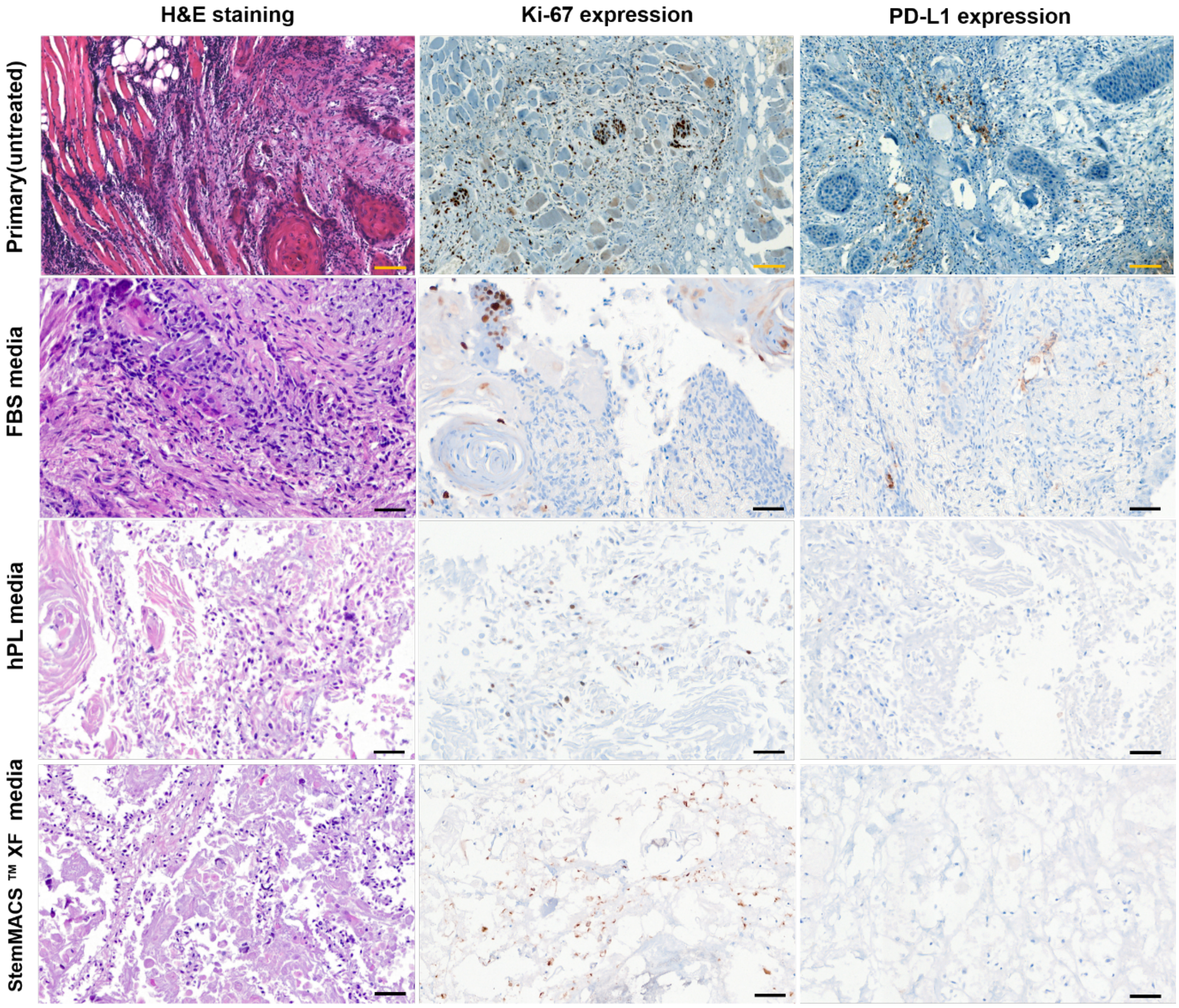

Figure 27 HNSCC explants cultured in different media exhibited varied tissue structural morphology and reduced Ki-67 and PD-L1 expression. *Comparison of tissue morphology across different media (FBS, hPL, and StemMACS™ XF) to untreated primaries, based on H&E staining, revealed a varied tissue structure in all conditions. Ki-67 (proliferation biomarker) and PD-L1 (immune checkpoint inhibitor biomarker) expression patterns were also variable across FBS, hPL, and StemMACS™ XF media-grown tissues. Scale: 100 µm for images from primary samples; 50 µm for images from tissues grown in different media.*

3.12. Chemotherapy exposure to HNSCC explants in xeno-free media behaved similar to FBS-serum prone cultures

To further assess the suitability of xeno-free media for HNSCC cultures, the 3D HNSCC explant model in xeno-free media was subjected to chemotherapy and compared with explants grown in FBS-supplemented media. The study focused on evaluating the impact of cisplatin on tissue viability, proliferation, and PD-L1 expression. Cisplatin treatment was administered on days 1, 3, 5, and 7, coinciding with media changes, at an optimized concentration of 80 µM (Cis80) (Figure 4d). This dosage was determined through iterative testing of different concentrations (40, 80, and 120 µM). Concentrations of 40 µM and 120 µM were deemed insufficiently effective and excessively cytotoxic, respectively, thus aligning with findings from prior studies. [63] The 80 µM dose was thus selected as optimal for further analyzes and was consistent with the dosage used in 2D and 3D HNSCC models. [63] The effects of Cis80 treatment were analyzed based on Ki-67 (proliferation) and PD-L1 (immune checkpoint) expression levels (Figure 29).

Although morphological changes following Cis80 treatment were consistent across all media types, the overall tissue architecture, followed a similar pattern to previous observations under xeno-free media culture (Figure 27). Untreated control tissues maintained a cuboidal cellular morphology, a characteristic of squamous epithelial cells (Figure 28), [80-82] while Cis80-treated tissues exhibited a rounded appearance and signs of cellular distress (Figure 28). [7, 80] Importantly, Ki-67 expression patterns remained consistent across media types, with a moderate reduction in proliferation observed following treatment. Conversely, PD-L1 expression showed a significant and consistent increase upon cisplatin exposure, irrespective of the growth media used.

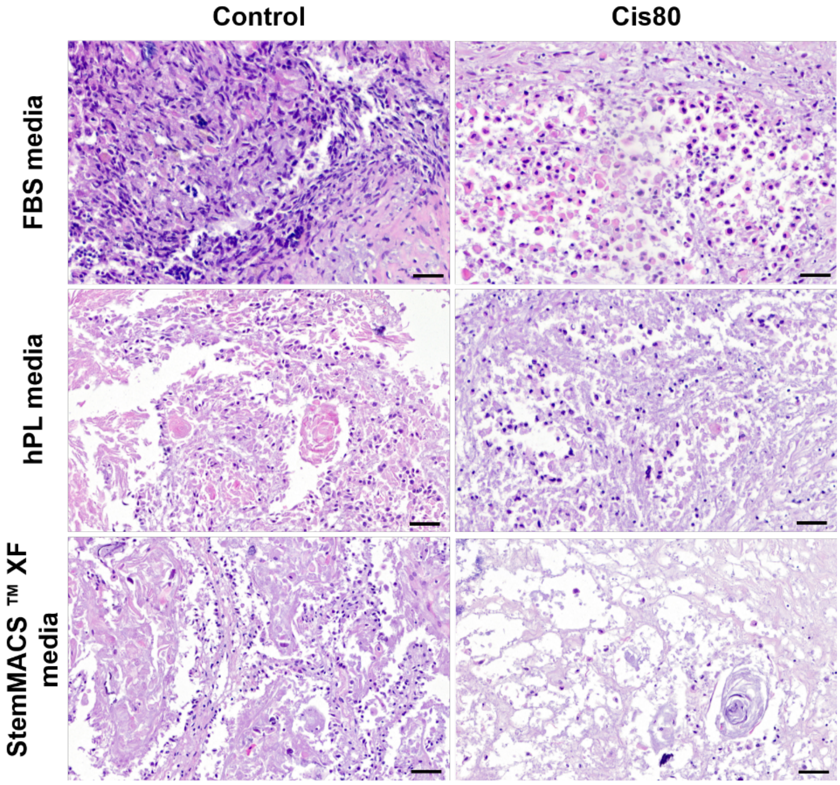

Figure 28 HNSCC tissues undergo significant morphological changes upon exposure to 80 μм Cisplatin. *The typical elongated HNSCC cell shape is altered to a more rounded morphology following cisplatin treatment. This change was consistently observed across all media. (Scale: 50 μm)*

Quantitative IHC analyses indicated that the type of growth media had a relatively small effect on the tissue response to Cis80 treatment, accounting for only 18.35% of total variance (p = 0.0246). However, cisplatin treatment itself had a significant impact, with PD-L1 expression increasing substantially (51.64% of total variance; p = 0.0007) and Ki-67 expression decreasing significantly (32.25% of total variance; p = 0.0045) (Figure 29a and b). These effects were consistent across all media types, with similar trends observed in both the tumor proportion score (TPS) and percentage of positive cells (P.P) metrics for Ki-67 and PD-L1 biomarkers across all *ex vivo* samples treated with 80 μM cisplatin (Figure 29c and d).

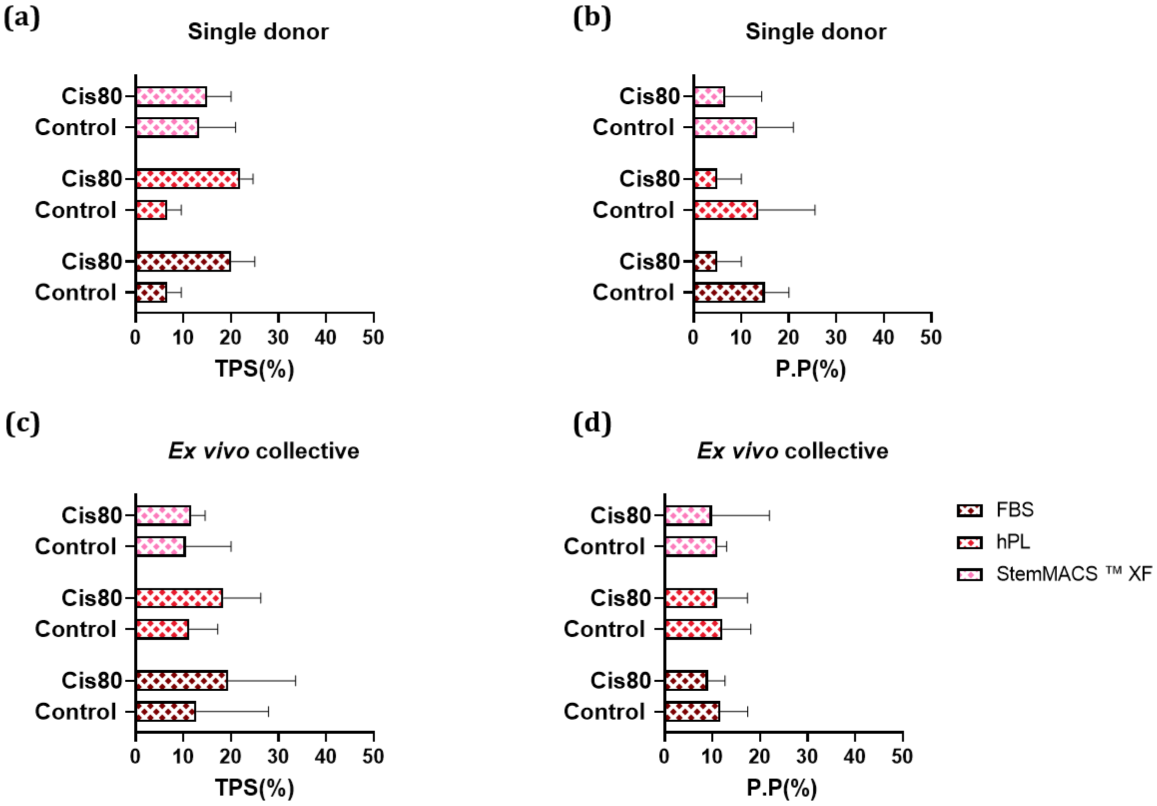

Figure 29 Cisplatin treatment induces upregulation of PD-L1 expression and a decrease in Ki-67 expression. *The tissue percentage score (TPS) for specimens treated with cisplatin in hPL and StemMACS™ XF media followed a similar trend to those in FBS media, with PD-L1 induction being notably higher in FBS and hPL media compared to StemMACS™ XF media (a). In contrast, the percentage of Ki-67 positive cells (P.P) significantly decreased after cisplatin treatment (b), a trend observed across all media conditions. Collectively, the TPS values across the ex vivo cohort showed a marked increase in PD-L1 expression following cisplatin exposure (c). Conversely, the P.P for Ki-67 decreased in samples from all media following cisplatin treatment (d). (Single donor for a & b: n = 1 (3 sections per donor), ROI = 3 per section; Ex-vivo 03 used. Ex-vivo collective for c & d: n = 8 (3 sections per donor), ROI = 3 per section; Ex-vivo 01-08 used. Statistical analysis: Two-way ANOVA).*

3.13. RCT promotes PD-L1 upregulation and suppression of proliferation in HNSCC explants cultured in xeno-free media similar to FBS-supplemented cultures

Building on the above findings, the study was extended to investigate the effects of RCT. Fractionated RT (2 Gy per fraction) was administered over five days (days 1, 2, 3, 6, and 7), delivering a cumulative dose of 10 Gy (Figure 4d). RT was combined with cisplatin (80 µᴍ) to simulate RCT conditions. Due to constraints in tissue availability, RCT experiments were exclusively conducted on explants maintained in xeno-free media.

Pronounced morphological alterations were observed in the xeno-free cultured explants post-RT. Irradiated samples exhibited significant cell enlargement, a hallmark of radiation-induced cellular stress as observed in the H&E-stained tissue samples (Figure 30a). When combined with Cis80, the explants displayed morphological features characteristic of necrosis and apoptosis, consistently observed in tissues cultured in both hPL and StemMACS™ XF media (Figure 28).

IHC analysis corroborated these morphological findings, revealing robust molecular responses to RT and RCT. In specific, microscopically, PD-L1 expression and Ki-67 expression did not show any significant modulations following RCT exposure (Figure 30b and c). These trends were consistently observed across both hPL- and StemMACS™ XF-based xeno-free media, demonstrating that the type of xeno-free media did not significantly influence the outcomes of RCT on PD-L1 and Ki-67 expression (Figure 30b and c). Previous studies have reported variability in PD-L1 modulation depending on the culture conditions, which aligns with the current observation. [83] The differential responses between hPL and StemMACS™ XF media highlight the critical role of culture conditions in modulating the therapeutic effects of these treatments.

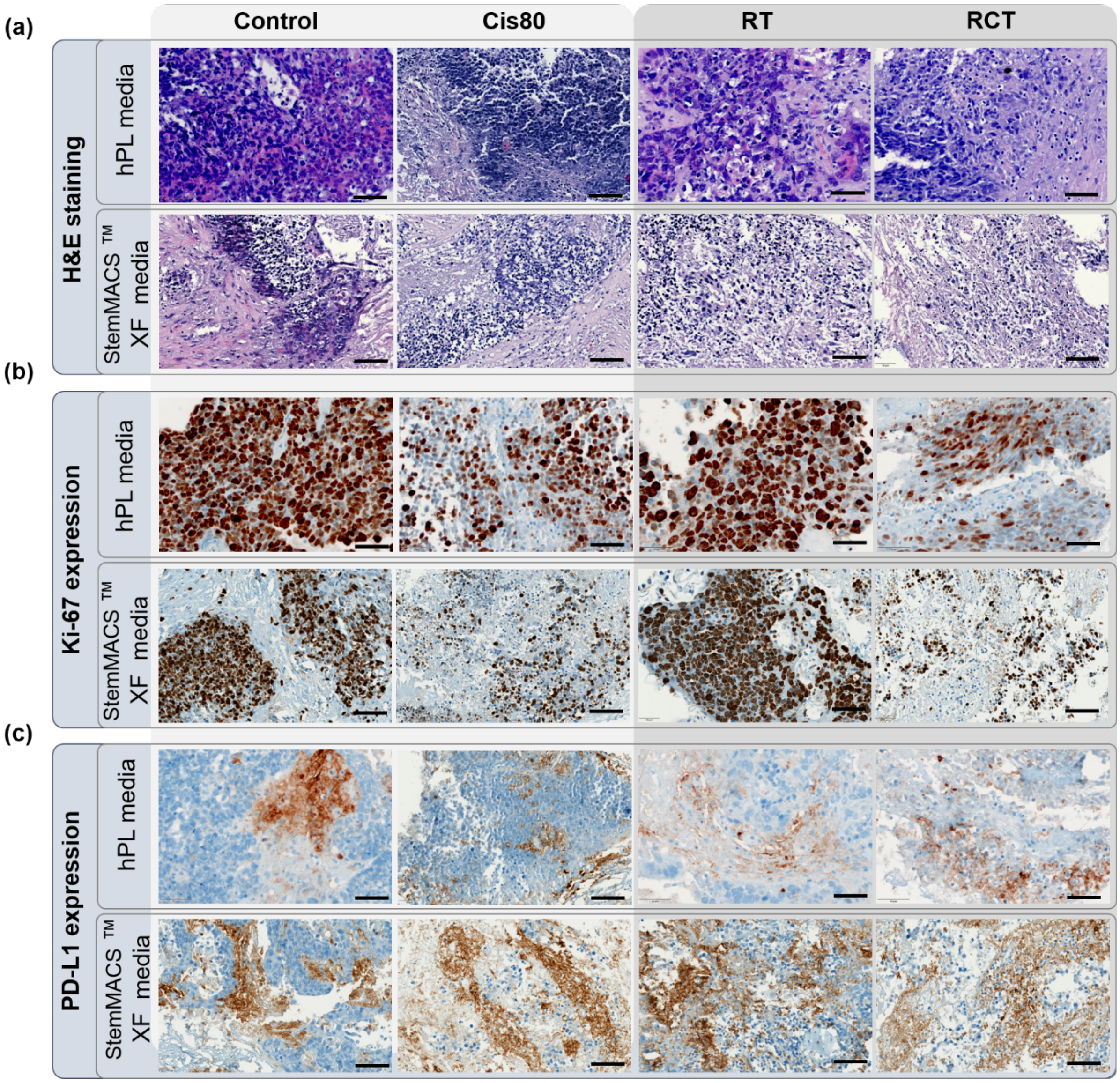

Figure 30 Haematoxylin and eosin (H&E) and immunohistochemical (IHC) staining demonstrate the impact of radio-chemotherapy (RCT) on HNSCC tissues. *RCT exposure led to consistent morphological changes in cells from ex vivo tissues cultured in both hPL and StemMACS™ XF media. (n = 2 (3 sections per donor); ROI = 3 per section; Ex-vivo 06 and 07 were used in this study). Scale: 50 µm.*

To explore the potential induction of EMT following treatment, vimentin expression was also analyzed via IHC staining (Figure 31). Tissues subjected to RCT exhibited a significant differences in vimentin expression compared to untreated controls. Tissues cultured in StemMACS™ XF media and treated with cisplatin alone or RCT showed signs of necrosis and structural disintegration. These observations may reflect intrinsic variability in tissue samples or heightened cytotoxicity induced by treatment.

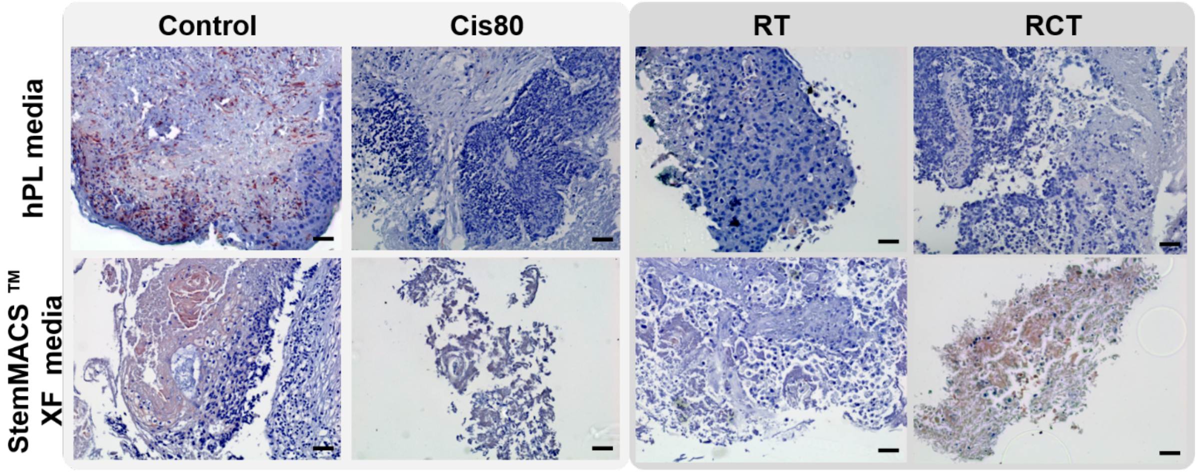

Figure 31 Immunohistochemical (IHC) analysis of irradiated HNSCC ex vivo tissues revealed a decrease in vimentin expression, an epithelial-mesenchymal transition (EMT) biomarker, following radio-chemotherapy (RCT) treatment. *The changes in vimentin expression induced by RCT were observed across both hPL and StemMACS™ XF media-grown samples. A marked variation in vimentin expression was observed in RCT-treated samples compared to their respective controls. (n = 3; ROI = 3 per sample per condition). Scale: 50 µm*

Collectively, these results indicate that RT and RCT elicit consistent molecular and morphological responses in *ex vivo* HNSCC cultures, dependent of the type of xeno-free media used or sample type.

AIM 1: 3D BIOPRINTED HNSCC MODEL ESTABLISHMENT

4. DISCUSSION

4.1. Designing and optimizing parameters for 3D model establishment

To establish a 3D bioprinted model for HNSCCs, a clear understanding of the original HNSCC TME and its spatial arrangement is necessary. *Jhaveri N et al.,* examined the histomorphology of primary HNSCC using H&E staining and spatial proteomics by mapping the protein distribution within native HNSCC samples. [72] The study revealed heterogeneity in tumor vascularization and immune cell infiltration presenting tumor regions in a stromal-matrix bed with some regions being highly infiltrated with immune cells while others with minimal to no immune cell invasion. [72] In addition, the vascular networks were far from the tumor-stroma zones. According to *Seshadri M et al.,* the HNSCCs with various tumor sites- oral cavity, larynx and base of the tongue showed significant variation in their pathology despite of their patient specific origin.[84] It is well-known that the HNSCCs exhibit considerable variation in clinical response, owing to the presence of such inter and intra-tumoral variation/ heterogeneity. To mimic such a heterogeneous TME mimic by 3D bioprinting would require a step-by-step incorporation of TME components. Hence, firstly, a homotypic 3D HNSCC model was designed and optimized before advancing it to a heterotypic model.

Although attaining a bioprintable and a bioavailable 3D HNSCC model that replicates the native TME is challenging, critical bioprinting parameters such as - printing temperature and speed, infill density, layer count, printing pattern, gelation time and temperature, nozzle diameter, and crosslinking method must be tailored to a particular system. As mentioned earlier, these parameters were optimized and tailored to our system through a series of trial and error experiments (Table 10). One such critical factor is defining the cell density used to create the bioink for the bioprinting process since it defines the cell-to-cell and cell-to-matrix interactions.

Having tested cell densities- 1 × 10^5, 1 × 10^6, and 1 × 10^7 UM-SCC-11B cells/mL bioink, it was observed that the cell-to-cell distance was minimal when bioprinted with 1 × 10^7 cells/ mL bioink (Figure 11). Most prevalently for the biofabrication of 3D bioprinted models many scientists have opted for the cell density 1 × 10^7 cells/ mL bioink to establish maximum cell-to-cell interaction. [25, 39, 61, 62, 85] However in such models, the model dimensions were in the range of 5 mm and above in gridded 3D rectangular constructs. For such high volumes per construct, it becomes essential to use higher cellular densities for attaining a higher number of cells per construct. [46, 48, 86] However in our model, occasional experimental hindrances such as nozzle clogging which limited the number of attainable bioprinted sample replicates was noted with cell density of 1 × 10^7 cells/mL bioink. Consequently, this adversely impacted the continuous bioprintablility and affected the construct's shape and structural fidelity. Hence, a cell density of 5 × 10^6 cells/mL was selected, as it did not compromise printability enabling the production of sufficient replicates for further investigation and data reproducibility.

4.2. Bioprinting reduces but retains HNSCC-cell type specific metabolic activity and viability

Once the bioprinting parameters were optimized, cell viability in the bioconstructs was determined by comparing the 3D model to the 2D *in vitro* model (Figure 12). There was a decrease in luminescence in 3D constructs compared to the 2D model. This observed difference may result from signal scattering or refraction within the hydrogel matrix or possibly reflect cells in distress from shear forces during bioprinting. [43, 59, 74]

The luminescence intensity, i.e., ATP production levels are specific to the cell type used. UM-SCC-22B cells had higher ATP RLU levels in comparison to the UM-SCC-14C and 11B. Generally, in accordance with 2D cultures, UM-SCC-14C and UM-SCC-11B cells showed a threefold faster doubling rate than UM-SCC-22B cells. This variation in metabolic activity might relate to the tumor tissue origin and malignancy grade of each cell line. [15] Elevated ATP levels, often observed in the TME, are associated with tumor metastasis, while lower ATP levels are linked to proliferation and immune suppression. [15]

Interestingly, UM-SCC-22B cells, derived from lymph node metastases, and UM-SCC-11B cells, originating from the larynx, exhibited distinct ATP profiles that may reflect their metastatic and proliferative characteristics, respectively. These observations may indicate that potentially metabolic activity might vary based on tumor stage and tissue origin.[87] This complexity likely arises from a combination of intrinsic cellular programs, microenvironmental constraints, and selective evolutionary pressures during tumor progression. [87-89]

One key metabolic shift in HNSCC is the elevated glutamate-to-glutamine ratio, largely driven by increased glutaminase activity, especially in metastatic lesions. [87-89] Early-stage tumors still maintain some balance between glycolysis (Warburg effect) and oxidative phosphorylation, as seen in nuclear magnetic resonance (NMR) metabolomics data. [87-89] But as the tumor advances, this balance shifts the metastatic HNSCC cells to elevate glutaminase expression, leading to excessive glutamate accumulation and glutamine depletion. This adaptation seems to help tumors survive under extreme conditions, like hypoxia and immune competition for glucose in the tumor microenvironment.

That said, the current observations and interpretations still need further validation, both in terms of metabolic profiling across different HNSCC subtypes and in relation to what's already reported in the literature. Further investigation is necessary to to correlate these metabolic patterns to actual tumor behavior and treatment responses. Expanding this study to include a larger sample size and additional tissue samples, particularly primary tissues, would enable a more comprehensive understanding of the correlation between tumor stage and ATP levels. In the current study, technical replicates were limited to n=12. Future studies should incorporate larger sample sizes and compare ATP levels with clinical pathology data to investigate the tumor stage-dependent metabolic activity more effectively. Such a comparative study could provide deeper insights into whether and how difference in metabolic profiles correlate with tumor progression and therapeutic outcomes.

4.3. Carboxy-NC supports long-term HNSCC cell survival in 3D bioprinted constructs comparable to GelMAA

With respect to hydrogel usability, NC-based bioinks exhibited greater stability and bioprintability compared to the standard GelMAA bioink. This enhanced performance is attributed to the nanocellulose (NC) component, which improves viscosity, shear-thinning behavior, and structural integrity post-bioprinting.[49, 52, 91-93] The superior mechanical properties of NC bioinks facilitate consistent extrusion, reduce nozzle clogging, and enhance the overall fidelity of printed constructs, making them a promising alternative for complex tissue engineering applications.

Moreover, the HNSCC cells bioprinted in GelMAA may be exposed them to additional stress beyond that associated with the extrusion process. This additional stress may arise from continuous temperature fluctuations inherent to GelMA-based bioprinting, particularly due to the gelation and extrusion cycle.[60, 94] These transitions introduce dynamic viscosity changes, which can elevate cellular stress responses, potentially impacting cell survival and function. Such effects are of particular concern when bioprinting highly sensitive or heterogeneous TME. [46, 73, 95]

To address these challenges, recent studies have explored surface modifications of GelMA, such as incorporating Laponite-RGD, which has been shown to improve rheological stability. [60] While improved cell viability was observed in MCF-7 cells post-bioprinting with such modifications, it is important to consider that the efficacy of these bioink surface alterations may vary depending on the specific cell type or tissue type, introducing additional variability in regard to multicellular- TME modeling. [46, 73, 95]

Quantitative analysis of cell viability, Ki-67 and E-cad expression suggested that the biochemical and mechanical properties of Carboxy-NC bioink may better support HNSCC cell proliferation and epithelial characteristics compared to TEMPO-NC. Interpreting the overall differences between TEMPO-NC and Carboxy-NC versus GelMAA suggested that the decrease in the viability, metabolic activity and proliferation could have been greatly impacted due to either the bioprinting process or the crosslinker concentration used. If it was due to the bioprinting process- all the different cell-laden TEMPO-NC and Carboxy-NC would have been affected equivalently, as the bioprinting conditions were the same for TEMPO-NC and Carboxy-NC constructs. However, it was clear that UM-SCC-14C and UM-SCC-11B specifically did not recover. The observed vacuole formation hinted the possibility of ionic oversaturation which could have eventually led to cell death in long-term. [47, 59, 74] Therefore, the chemical crosslinker $CaCl_2$'s concentration was reduced from 50 mM to 20 mM. Previous findings suggested that calcium ion-induced membrane damage and vacuolization can disrupt cellular homeostasis leading to cell death. [47, 59, 74] Reducing the crosslinker concentration to 20 mM significantly improved cell viability across all constructs, confirming that the higher crosslinker concentration was a key factor in cytotoxicity. [46, 73, 95] Nonetheless, further studies on ionic calcium levels within the bioconstructs and cells are required to further evaluate the current findings on viability due to the Ca^{2+} ion concentration.

The observed improvements in viability with reduced crosslinker concentrations were consistent with prior studies indicating that optimal crosslinker concentrations vary depending on cell type and hydrogel composition. [46, 47] While reduced crosslinker concentrations enhanced viability, GelMAA constructs still demonstrated the highest cell viability, followed by Carboxy-NC and TEMPO-NC constructs. This might indicate the sensitivity of HNSCC cells to the crosslinker, as well as the influence of hydrogel stiffness on cell viability. Interestingly, UM-SCC-22B cells showed a significant increase in viable cell numbers at the end of the culture period, exceeding the initial cell numbers post-bioprinting (Figure 14b). This finding reflects the higher ATP levels in UM-SCC-22B cells (Figure 12), which may explain the differential viability trends among the HNSCC cell lines.

To determine whether hydrogel compatibility is cell-specific, a comparative study was conducted using MCF-7 breast cancer cells. The results revealed a similar viability trend across all bioinks (Figure 15). However, MCF-7 cells showed a significantly higher number of viable cells at the end of the culture compared to HNSCC cells, which could be due to the intrinsic robustness of MCF-7 cells. [43, 74] These findings raise the question of why both HNSCC and breast cancer cells appear to favor Carboxy-NC over TEMPO-NC for supporting typical cellular behaviors, such as growth and proliferation. A closer examination of the physicochemical properties of the hydrogels revealed structural differences that may explain these observations. TEMPO-NC, with its carboxyl (-COOH) group, may be less conducive to surface modifications due to the steric hindrance imposed by the bulkier TEMPO functional group. This limitation could impede cell proliferation and migration.[48, 66] In contrast, Carboxy-NC, having a carboxymethyl ($-CH_2COOH$) backbone, offers enhanced biocompatibility and mechanical properties. Similarly, GelMAA's amine-conjugated structure provides greater mechanical flexibility, thus facilitating cell migration.

Advancing the model to a heterotypic model was performed by introducing the stromal component of the TME- i.e., bioprinting fibroblasts cells along with epithelial cells (Figure 21a). Quantitatively examining the viability of both the cell types in both NC-bioink construct, it has been revealed that the tumor cells were better compatible with Carboxy-NC bioink, meanwhile the stromal cells preferred TEMPO-NC bioink (Figure 21b). Even though there was a minor difference in stromal cells' preferability towards TEMPO-NC, the difference was not that prominent or significant.

On the other hand, the observed mild difference in stromal cell viability towards the two NC bioinks could be attributed to insufficient tumor cell-to-stromal cell interactions. In this thesis, tumor and stromal cells were combined in a 5:1 ratio for bioprinting, primarily due to limited availability of primary stromal cells. However, *in vivo* tumor-to-stromal cell ratios typically range from 2:3 to 2:1, depending on the tumor stage. [96, 97] Achieving physiologically relevant cell-to-cell interactions require adjusting both cell density and 3D model dimensions. Specifically, reducing the epithelial cell density from 5× 10^6 to 2× 10^6 cells/ mL necessitates modifications to the model's spatial parameters to maintain adequate cell-to-cell interaction. This discrepancy in cell rations may have hindered the establishment of adequate cell-to-cell interactions, which are critical for regulating cellular processes such as proliferation, migration, and the generation of biochemical and mechanical cues. To address this limitation, future experiments should explore increasing the stromal cell density from 1× 10^6 to a range of 2× 10^6 to 6× 10^6, thereby achieving a tumor-to-stromal cell ratio closer to the in vivo range of 2:3 to 2:1.

Additionally, differences in stromal cell viability may be caused by their reliance on adhesion proteins for optimal growth. [98] Cancer-associated fibroblast and stromal cells typically require adhesion-mediated signaling and substrate interactions, which may not have been fully supported by the bioink compositions chosen. [98]

In conclusion, Carboxy-NC is proposed as a favorable bioink for HNSCC bioprinting, given its biochemical and mechanical properties comparable to GelMAA while offering additional advantages such as natural derivation, lower bioburden, and reduced immunogenicity (Table 11). However, the observed preference of fibroblast cells for TEMPO-NC necessitates further investigation to determine its suitability for tumor-stromal modeling. Modification such as RGD peptides could provide additional adhesion sites, further improving stromal cell viability. [60]

4.4. Microstructural analysis of hydrogels revealed variations in pore size, which are correlated with cell distribution

The data so far showed a clear advantage for Carboxy-NC over TEMPO-NC, for HNSCC cells, at least. Interestingly, the findings were the opposite when printing fibroblast. The SEM analysis confirmed differences in the microstructure of the hydrogels used (Figure 16).

Previous studies have thoroughly documented the critical role of pore size and distribution in regulating cell positioning, interaction, and migration. [100, 101] Furthermore, the microstructure of NC-hydrogels, including TTC and CTC, exhibits distinct differences compared to TEMPO-NC and Carboxy-NC hydrogels (Figure 17b and Figure **16**a, c). Specifically, TTC hydrogels demonstrate a more open pore structure compared to TEMPO-NC and Carboxy-NC hydrogels, while the microstructure of CTC hydrogels closely resembles that of GelMAA. These observations suggest that the alginate ratio used in the preparation of NC bioinks may have influenced pore distribution in the resulting hydrogels. [33, 50, 55, 57] To address this limitation, it is vital to reduce the alginate content and evaluate the stability of the bioprinted constructs over a 21-day period. Additionally, optimizing the bioink concentration could significantly enhance HNSCC cell survival. While this thesis has not explored varying bioink concentrations, this highlights an important trajectory for future investigations.

Ideally, for the development of a robust high-throughput drug testing tumor model it is necessary to opt for a hydrogel that possesses well-distributed pores and remain stable throughout the culture period. In this context, GelMAA exhibited the lowest structural stability, indicated by degraded edges within two weeks of culture. This observation correlated to the previous reports on the long-term instability of GelMAA structure. [49, 67, 94] Compared to GelMAA, NC-hydrogels demonstrated superior structural fidelity, as apparent from their improved initial handling and ease of maintenance during post-print culture.

Although the freeze-drying process used for sample preparation may introduce artifacts into the pore structures, I assume that its effects are uniform across all hydrogel types. This assumption obviates the need for more elaborate fixation techniques, such as those utilizing tannic acid and osmium tetroxide. [99]

For now, the closed pores of TEMPO-NC have been assumed to serve as an adhesion platform promoting cell cluster formation. Stromal cells' slight preference for TEMPO-NC bioink aligns with these observations, that the closed pores might promote cell attachment and growth. Interestingly, SEM analysis also showed that TEMPO-NC bioink had a smaller average pore area compared to Carboxy-NC bioink (Figure **16**). This observed trait, while beneficial for cell adhesion, might restrict cell migration and limit cell-to-cell interactions between printed layers. Importantly, fibroblasts and stromal cells tend to migrate and establish spindle-shape like structures to communicate between adjacent cellular pools in the TME. [43, 55, 95] Such a limitation in the TEMPO-NC could restricts the characteristic cellular behavior of the stromal cells.[43, 55, 95] To address these limitations, surface modification of Carboxy-NC bioink with adhesion proteins could enhance hydrogel properties, offering a cell-friendly environment while maintaining structural fidelity.

Expanding the model further requires examining the cell adhesion onto the hydrogel becomes vital particularly, to understand the interactions between different cell types including, stromal, endothelial and immune cells. Examining these interactions is critical for capturing the complexity of the TME. Future experiments must focus on investigating cell-laden bioconstructs within different bioinks, aiming to elucidate the variations in cell adherence across various hydrogels. [43, 44, 46-48, 95] The experiments must be designed with a particular emphasis on tumor-stroma, tumor-vascular and immune-tumor interactions. To accurately assess these multicellular interactions, the SEM sample preparation protocol must be specifically adapted for embedded cells. Utilizing advanced fixation techniques such as tannic acid and osmium tetroxide are necessary to enhance structural preservation and improve visualization. [99] This protocol modification becomes crucial for preserving the cells within the construct while ensuring that important cell-hydrogel matrix interactions are not overlooked. [46] Implementing these refinements will provide a more comprehensive understanding of how different cell types interact within engineered tumor constructs.

I assume that every cell-type would require specific bioinks that meet their respective requirements to precisely mimic the TME. For example, laponite-RGD-modified GelMA has been used to support adherence-dependent cell types, such as MCF-7 and fibroblasts, while VEGF modification is commonly used to enhance endothelial cell function, and M1 macrophage-specific modifications are applied to promote monocyte behavior. [26, 33, 60, 92, 102] Ideally, it is best to employ one hydrogel for all cell types to avoid hydrogel-to-hydrogel related impact on the model viability. However, these crucial points must be considered for replicating the relevant cell specific biochemical and biomechanical cues.

4.5. HNSCC cells proliferate in all bioinks, maintaining epithelial phenotypes while exhibiting a distinct bioink specific cell distribution

The IF data indicated that the HNSCC cells survived and proliferated within all bioinks while maintaining their characteristic epithelial biomarker expression (Figure 18 and Figure **19**). Although the cell viability data indicated variability in HNSCC survival across different hydrogels with GelMAA and Carboxy-NC demonstrating better viabilities than TEMPO-NC, IF data further substantiated this pattern by confirming consistent proliferation within the bioconstructs.

Compared to the presented viability data, the percentage of Ki-67 positive cells within the constructs differed significantly. The observed discrepancies in the IF results against Ki-67 could be attributed due to the region of interest (ROI) chosen for visualisation. Experimentally, for each condition, three samples were stained, and three distinct ROIs (centre, intermediate, and outer regions) of 200 µm z-stacks per sample were analyzed. These ROIs were chosen to capture the native situation’s characteristic tumor zonal architecture containing necrotic, quiescent, and proliferative zones. [61] However, not all metabolically active cells within the constructs may have been proliferating during the imaging period, introducing potential variability in the Ki-67 staining results. Despite this, the observed Ki-67 expression aligned with the trends observed in cell viability assessments. In accordance with the E-cad expression between 2D and 3D cultures there was a huge variation in the percentage of cells tested positive. This difference may stem from the inherent limitations of the imaging methodology. [48]

To address the limitations imposed by current imaging and image analysis methods, the development of more advanced and sophisticated 3D imaging and analytical tools tailored specifically to 3D bioprinted systems is essential. [103] In this study, the bioconstructs were imaged using confocal microscopy, generating z-stack images with a thickness of 200 µm per sample. However, this approach may have been insufficient to capture cells located between slices within the stack, potentially resulting in partial data loss. Also, the current image analysis method relied primarily on manual cell counting in the z-stack using maximum projection, which may have further limited the accuracy and depth of the analysis. To tackle these limitations- advanced image analysis techniques must be explored using software Imaris or Arivis. [103] New methods should incorporate comprehensive examination of every slice within the z-stack, enabling accurate tracking of cellular distribution and expression scalable across the entire construct. Such advanced techniques would require the development of a machine learning algorithm to create volumetric reconstruction of the z-stack to track every cell expressing their respective markers. This would improve the predictability of the expression throughout the construct thus allowing a quicker processing and automation. [103]

The observed decrease in E-cad expression might also indicate the initiation of EMT with cells progressively loosing their respective epithelial properties acquiring mesenchymal characteristics.[104] Co-staining for E-cadherin and vimentin- a typical EMT marker, revealed co-expression in both 3D and 2D cultures (Figure 18 and Figure **20**). This observation supports recent evidence suggesting that HNSCC cells may undergo partial EMT, resulting in a metastable state characterised by simultaneous epithelial and mesenchymal marker expression. [105]

Additionally, the cell clusters observed in both Ki-67 and E-cad immunostained constructs revealed significant variations in cell distribution across the different bioinks. The SEM analysis revealed large, rough surfaces with closed pores in TEMPO-NC bioinks, resembling the microenvironment of 2D culture systems which could potentially support monolayer like cell growth patterns. [33, 57] These structural characteristics explains the formation of relatively larger cell clusters in TEMPO-NC bioconstructs than in Carboxy-NC and GelMAA constructs. This contrasts with the more typical 3D proliferation observed in the other bioinks. To illustrate better how the cells are distributed within the hydrogel matrix over 21-days of culture, SEM characterization should be performed on the same days as IF staining. This could reveal deeper insights on the cell growth and proliferation pattern within the matrix, especially crucial for advancing the homotypic 3D model to a heterotypic model. [71-73] As stated in the section 4.4., to study tumor-stroma, tumor-vascular and immune-tumor interactions replicating the native TME, such a detailed investigation on the behavior of different cell's growth pattern within different hydrogels is vital.

AIM 2: FUNCTIONAL VALIDATION OF THE ESTABLISHED 3D BIOPRINTED MODEL

4.6. RCT treatment significantly reduced the viability of HNSCC as opposed to RT or Cis80 treatment

Following the establishment of the 3D bioprinted model for HNSCC, the model was tested for its functionality by treating the established 3D homotypic bioprinted HNSCC model with RCT. RCT had a larger impact compared to samples treated with one modality only. Also, it was revealed that the efficacy of RT alone was relatively lower compared to Cis80 (Figure 22).

While RT has been widely reported to induce rapid cell death in HNSCC cells in 2D cultures, 3D spheroids, and explant models, [106] its effectiveness was delayed in the 3D bioprinted constructs. This discrepancy may be attributed to the unique characteristics of the bioprinted model, particularly the physical and optical properties of the hydrogel matrix. These properties could influence radiation exposure by limiting its penetration depth and providing inherent radioprotective effects, which shield the embedded cells from the full intensity. [106]

In contrast to traditional 2D and explant models, Cis80 induced cell death in a more pronounced manner in the 3D bioprinted constructs. [106] This demonstrates the influence of model-specific factors, such as hydrogel-mediated radiation reduction and drug diffusion patterns, which might better mimic the *in vivo* tumor microenvironment as opposed to 2D and explant models. [2, 14] The bioconstructs' behavior in response to RCT better reflects the clinical effects than in 2D and explant models. To investigate these observations in more detail, the RCT data must be compared to the clinical outcome in a patient specific manner.

In this study, bioprinted constructs were cultured in polystyrene-based 96-well flat-bottom plates, with 200 µL of growth medium per well. The RT dose of 2 Gy, standardized for 2D and 3D spheroidal cultures, may not have achieved comparable intensity within the bioprinted constructs. The RT beam traversed multiple layers, including the plastic plate, the growth medium, and the hydrogel matrix, before reaching the embedded cells. While 3D spheroids and bioprinted constructs share the plastic plate and growth medium, the hydrogel matrix in bioprinted constructs introduces scattering and attenuation, reducing the effective dose.[39]

Physical interactions such as reflection, refraction, total internal reflection, and beam scattering lead to energy redistribution and reduced RT intensity at the cellular level. [106] These effects impact RT specificity and efficacy in 3D bioprinted models.[39, 107] Accurate dose estimation for 3D bioconstructs may require Monte Carlo simulations to account for complex geometries, hydrogel composition, and material interfaces. [39, 107] Standardization challenges may persist, as bioprinted constructs may need higher RT doses for comparable in vitro therapeutic effects.

While the hydrogel matrix effectively mimics the native extracellular environment, supporting cell viability and growth, its shielding properties might slightly alter the therapeutic dynamics of RT. [47, 66] This highlights the importance of accounting for beam-material interactions when optimizing 3D bioprinted models for radiation-based studies. Further research is required to refine the model, particularly by addressing the complexities of radiation delivery and its interactions with hydrogel matrices. Additionally, the continuous presence of cisplatin in the growth medium for 48 hrs post-treatment, combined with the timing of viability assessments, likely contributed to its enhanced cytotoxic efficacy in the 3D bioprinted constructs. These findings emphasize the unique therapeutic response characteristics of the bioprinted model, driven by its matrix composition and architectural fidelity. Overall, the observed differential sensitivity of the 3D bioprinted model to RCT highlights its potential utility in simulating *in vivo*-like therapeutic responses.

4.7. RCT reduced the proliferation rate and epithelial phenotype of HNSCC cells

Having investigated the survival of UM-SCC-22B cells in Carboxy-NC bioink constructs in response to RCT treatment, the next step was to gain insights on their proliferation rates and their characteristic biomarker expression maintenance. IF staining for Ki-67 and E-cad confirmed that the combinational treatment had a stronger impact than the Cis80 and RT treatments alone (Figure 23 & Figure **24**).

Although the observed reduction in Ki-67 expression aligned with the viability results, the lack of statistical significance suggests potential variability in cellular responses. Such variations could arise from differences in treatment sensitivity, experimental conditions, or the timepoint selected for analysis. A study conducted by *Mei et al.,* reported that the effects of RT on bioconstructs were rather acute. [12, 108] The study further extended its investigation to evaluate DNA damage post-RT treatment and demonstrated that RT-induced DNA damage contributed to a reduced proliferation rate, albeit in a delayed manner. [108] Drawing parallels with these findings, the delayed response observed in the current 3D bioprinted HNSCC model may similarly involve DNA damage mechanisms induced by the RCT treatment. A study conducted but *Affolter et. al.,* on the post-RT DNA damage using a 2D *in vitro* model reported similar findings to the current study (Publication in preparation). [17, 63]

To validate the findings in the 3D bioprinted model, further studies are necessary to investigate the DNA damage response and its role in the delayed impact of RT treatment. This emphasizes the importance of optimizing experimental conditions and broadening the temporal scope of assessments to capture a more comprehensive understanding of cellular dynamics post-treatment.

As discussed earlier, the prolonged presence of Cis80 in the culture media could have enhanced the efficacy of the chemotherapy treatment compared to RT. While the proliferation rate data (Figure 23b) aligned well with the viability results (Figure 22), a noticeable difference between the Cis80 and RCT-treated samples was evident. To explore this further, it would be beneficial to evaluate proliferation rates at more frequent intervals, starting from 2 hrs post-treatment, to obtain a consolidated overview of treatment progression and its effects. [11, 12, 19]

Additionally, the observed decline in E-cadherin expression with combinational treatment was more pronounced than with Cis80 or RT alone. This suggests that RCT treatment may accelerate the onset of EMT. As discussed in section 4.5, HNSCC cells are known to undergo partial EMT in 3D culture systems. [105] Prolonged culture periods in the hydrogel matrix may facilitate this transition. The immediate decline in E-cadherin levels in the RCT-treated bioconstructs suggests an earlier onset of EMT. To further investigate this, bioconstructs should be stained for vimentin, on D4 post-treatment to confirm EMT progression. [14, 109] The inclusion vimentin staining results offers a more comprehensive evaluation of the mesenchymal transition in our 3D bioprinted model under RCT conditions.

Moreover, as stated in section 4.5, imaging and image analysis may introduce variability in the current observations. Manual errors during imaging and subsequent analysis could have contributed to discrepancies in the results. Future studies should address these limitations by adopting more robust methodologies, including extended culture durations, optimizing treatment dosages, and employing additional EMT markers such as vimentin. Enhanced imaging techniques and quantitative image analysis methods tailored for 3D bioprinted models are crucial to delineate the effects of RCT on proliferation and biomarker expression with greater accuracy. In conclusion, as a proof-of-principle, the established model has proven its functional validation in terms of its response to RCT.

4.8. Chemotherapeutic treatment has a differential effect on the primary 3D bioprinted and 3D spheroidal systems

Once the established 3D bioprinted model demonstrated its potential functional use as a HTS tool, the clinical relevance of the system was further studied by bioprinting patient-derived HNSCC cells and treating them with Cis80. The performance of the bioprinted model was compared with a spheroid model (Figure 25). [63, 78] Viability results revealed a distinct and varied response between the two models which highlighted a significant advantage of the 3D bioprinted constructs over spheroids.

A key strength of the 3D bioprinted model lies in its capacity to integrate all seeded cells directly into the hydrogel matrix. In contrast, cell seeding in spheroids or the culture of patient-derived organoids often resulted in the preferential selection of specific subpopulations, such as stem-like cell subtypes, as previously reported for patient-derived organoids. [79] This difference might have contributed to the responses observed in the bioprinted constructs which did not exhibit such a selective cell growth within the hydrogel matrix.

Additionally, HNSCC cells derived from different donors formed spheroids of varying sizes, leading to noticeable differences in spheroid morphology. These structural variations influence nutrient and oxygen transfer rates, potentially compromising the consistency and reproducibility of HTS studies. [4, 25, 79] Unequal transfer rates could result in differential drug activity, thereby limiting the alignment of spheroid-based findings with *in vivo* drug responses.

While neither model can fully replicated *in vivo* drug efficacy, the 3D bioprinted model might provide a closer approximation to *in vivo* conditions- including RCT responses.

3D spheroid or organoid models have been reported to be closer to the native than the conventional 2D *in vitro* cultures, although the spheroid model might overestimate drug-induced cytotoxicity, a phenomenon consistent with prior reports. [4, 25] The observed size-related differences in the spheroid model were not a feature of the 3D bioprinted model. [61] The even distribution of cells within the bioprinted constructs eliminates size-related limitations on nutrient and oxygen diffusion, which are often encountered in spheroid systems. This uniformity establishes a more stable and physiologically relevant environment conducive to long-term monitoring of drug effects.

Such a consistent and replicable system provides a robust platform for investigating drug resistance, toxicity, and activity, closely mimicking the native TME. However, further characterization of drug effects at the morphological, protein, and genetic levels is essential to comprehensively compare the spheroid and bioprinted models.

By overcoming the inherent limitations of spheroid-based models, the 3D bioprinted constructs might offer a more reliable system for clinically relevant investigations. While spheroids remain valuable for initial HTS applications, the 3D bioprinted model demonstrated superior translational potential, particularly for extended and detailed evaluations of drug responses, highlighting its suitability for advancing precision oncology, bridging the gap between *in vitro* systems and *in vivo* outcomes. [25, 39]

AIM 3: DEVELOPMENT OF XENO-FREE 3D PATIENT-DERIVED HNSCC EXPLANT MODEL

4.9. HNSCC explants survived in xeno-free media expressing characteristic markers

This study demonstrated that HNSCC explants can be successfully cultured under xeno-free conditions, demonstrating survival in both hPL and StemMACS™ XF media. This adaptation of the in-house established explant model to xeno-free conditions emphasizes its potential to reduce reliance on animal-derived supplements, aligning with ethical and regulatory shifts toward xeno-free preclinical research systems.

Histological analyses confirmed that tissues cultured in xeno-free media, particularly hPL and StemMACS™ XF media, preserved key histomorphological features comparable to FBS-supplemented conditions and native primary tissues (Figure 27). However, this preservation was not uniform across all media types. Specifically, increased morphological distortions and necrotic features were observed in StemMACS™ XF samples, suggesting potential limitations in nutrient composition, growth factor availability, or metabolic waste management, which may contribute to tissue damage and necrosis. Optimizing these factors are critical to minimizing necrosis and maintaining tissue viability. [110-112] While the data suggest that hPL and FBS-supplemented media relatively better support tissue morphology, direct comparative analyses including proliferation and viability markers are required to draw conclusions about their relative efficacy. [110-112]

The observed results for *ex vivo* sample number 3, derived from an oropharyngeal tumor with a TPS score of 5%, suggest that intrinsic tumor characteristics might have influenced the culture outcomes. Specifically, samples cultured in StemMACS™ XF media exhibited the most pronounced morphological distortions. These distortions could be attributed to media-specific limitations in nutrient availability, oxygenation, or metabolite clearance, emphasizing the necessity for systemic model refinement. [18, 63, 76] Moreover, the selection of tissue for culture necessitates a site-specific assessment to distinguish tumor from non-tumor regions. The observed morphological alterations may also indicate the presence of muscle tissue or other non-tumor components, which could influence the overall culture response. The reduced Ki-67 and PD-L1 expression observed in StemMACS™ XF media may indicate diminished proliferative capacity and altered immune checkpoint regulation, respectively. To ensure the reliability of the explant model in mimicking native tumor characteristics, the clinical attributes of *ex vivo* sample number 3 must be cross validated with the explant culture.

The differential expression of Ki-67 and PD-L1 biomarkers across media types highlights the functional implications of media composition on tumor biology. Lower Ki-67 expression in StemMACS™ XF media might suggest reduced proliferative activity, which may indicate suboptimal support for active cell division in this media type. In contrast, the consistent PD-L1 expression across cultured and uncultured tissues implies that immune checkpoint marker expression is less sensitive to variations in media composition under the tested conditions. These findings further hint the need to correlate media effects with specific molecular and cellular pathways to gain a deeper understanding of their influence on tumor biology.

Establishing patient-derived explants with minimal bacterial and fungal contamination is crucial, as contamination can significantly alter drug response and other experimental outcomes. [111] The observed 30% contamination rate highlights the critical importance of optimizing sterilization protocols and aseptic techniques specific to patient-derived explant cultures. In accordance with the HNSCC explants in this study, the contamination rates are likely influenced by the anatomical site of tumor resection, with tumors from the oral cavity being particularly susceptible due to the high microbial load inherent to this region. [111] Also, the lack of standardized protocols for *ex vivo* model development poses a significant challenge. To address this, stringent tumor-specific workflow should be established, encompassing all stages from surgical resection to laboratory processing, to ensure consistency and reproducibility. Such refinements can enhance the success rate of patient-derived tissue cultures, thereby improving data collection from diverse tissue types. Additionally, improved protocols may facilitate the successful culture of tissues across various media conditions (as in FBS-serum vs xeno-free media), enabling comprehensive comparative analyses from a single donor. [113]

4.10. HNSCC explants in xeno-free media behaved similar to FBS-containing cultures following chemotherapy exposure

With evidence demonstrating that HNSCC tissues can survive in xeno-free media while maintaining the expression of PD-L1 and Ki-67 biomarkers over a 10-day culture period, subsequent experiments investigated the effects of Cis80 treatment. Cisplatin exposure elicited comparable responses in both xeno-free and FBS-based cultures, including similar morphological changes, moderate reductions in Ki-67 expression (indicative of proliferation), and significant increases in PD-L1 expression (Figure 29).

The lack of a substantial reduction in Ki-67 expression or increase in PD-L1 expression following Cis80 treatment suggested the need for further optimization of the experimental design. In principle, the sample size considered in this thesis was n=8. Expanding the study with a larger cohort might significantly increase the percentage of samples cultured in all the media, which would lead to a more precise quantitative interpretation of the drug effectivity. This is one major experimental design alteration is needed in the development xeno-free systems.

Clinically, platinum-based therapeutics, including cisplatin, were often prescribed as first-line adjuvant treatments for HNSCC. However, their efficacy is frequently undermined by the development of robust DNA damage repair mechanisms, which enable cancer cells to evade apoptosis. Translating these clinical phenomena into *in vitro* systems necessitates a more detailed investigation of apoptotic and DNA damage biomarkers. [1] In addition, clinically, increase in the PD-L1 expression coupled with the activation of MEK/ ERK pathway has been reported in response to cisplatin in HNSCC. [114] These definitive alterations modify the treatment responses. Hence IHC staining on caspase-cleaved CK18 for apoptosis; phosphorylated-H2AX for DNA damage; p-MEK expression for MEK pathway activation in parallel with Ki-67 biomarker- for cell proliferation and PD-L1 biomarker- for PD-1/ PD-L1 blocking agent must be performed to gain more insights on the effects of Cis80 to the HNSCC explants. [114, 115]

While this study observed an upregulation of PD-L1 expression in response to Cis80 (Figure 29a and c), the increase was moderate, aligning with previous in-house findings. [63, 68] Existing literature suggests that PD-L1 upregulation in tumor cells is influenced by factors such as tumor-infiltrating lymphocytes, mutational burden, and tumor cell viability. [18, 76, 116] For example, *Lin et al.,* reported that elevated PD-L1 expression correlates with sensitivity to checkpoint inhibitors, particularly in tumors with high mutational burden. [117] This context-dependent variability in PD-L1 expression underscores the need for larger cohort studies to elucidate the precise relationship between cisplatin exposure and PD-L1 modulation. [117]

In conventional 2D *in vitro* systems, cisplatin induced a rapid and pronounced decline in proliferation and an immediate upregulation in PD-L1 expression. [63, 115] For advanced *in vitro* models, such as 3D spheroids, bioconstructs, or explants, the immediate effects of cisplatin on proliferation and PD-L1 expression were less pronounced compared to traditional 2D systems. [118] In the previous study using a 3D bioprinted HNSCC model, patient-derived cells exhibited a more gradual decline in proliferation compared to patient-derived spheroids (Figure 25).

Given that explant models more closely recapitulate the pathophysiological behavior of the native TME, the moderate decline in Ki-67 expression observed in this study may better represent the *in vivo* response to cisplatin.

As discussed earlier, a detailed time-course analysis of Ki-67 expression is essential to capture the temporal dynamics of proliferation under cisplatin treatment. Additionally, studies incorporating apoptotic and DNA damage biomarkers will provide a comprehensive understanding of the mechanistic effects of cisplatin on HNSCC explants. [17]

4.11. Evaluation of RCT effects on HNSCC explants in xeno-free media

With the confirmation that chemotherapy-induced effects on Ki-67 and PD-L1 expression in xeno-free media were comparable to those observed in FBS-grown tissues, HNSCC explants cultured in xeno-free media were further exposed to RCT (Figure 30). Post-treatment analysis revealed an upregulation of PD-L1 expression across both hPL and StemMACS™ XF media, with StemMACS™ XF cultures exhibiting a higher rate of PD-L1 expression. This observation aligned with literature and previous observations that PD-L1 modulation is highly tumor-stage-dependent and varies based on the treatment regimen, particularly in response to platinum-based therapies combined with irradiation. [1, 118] Interestingly, media composition significantly influences responses of tumor explants. This was highlighted in a study by *Jakl et al.*, who demonstrated StemMACS-based media not only affected cell proliferation but also modulated immune marker expression, including PD-L1, across different cancer models.[119] This suggests the media composition could modulate immune evasion mechanisms in tumor tissues, potentially altering the tumor microenvironment and its response to treatment. [119]

PD-L1 upregulation, often associated with immune evasion, is linked to RT-induced DNA damage response, which activates pathways such as STING and NF-κB signaling, promoting the immune-modulatory effects of RT. [83] The media-specific differences in PD-L1 expression observed in this study may be partially due to the distinct growth factors and cytokines present in the hPL and StemMACS™ XF media. While StemMACS™ XF may contain similar growth factors to hPL such as, FGF-2, PDGF, TGFβ, hPL media are known to exhibit batch to batch variability. [119] This might have further induced immune modulation. To better explore such RCT induced responses, performing IHC and genetic expression analysis for these biomarkers would give valuable insights in the potential therapeutic responses. [120]

In addition to PD-L1 upregulation, RCT exposure led to a significant reduction in proliferation, indicated by the downregulation of Ki-67 expression. This decline was more pronounced in StemMACS™ XF -grown samples, potentially reflecting a greater induction of apoptosis or enhanced anti-proliferative effects. This finding is consistent with the well-documented role of RT in causing DNA damage, leading to cell cycle arrest and apoptosis. [2] Previous studies by *Jung et al*. and *Ward et al.* have similarly reported the anti-proliferative effects of RCT in various cancer models, which support the observations of this study. [121, 122] The potential interplay between treatment regimens and tumor-specific responses underscores the utility of this model for evaluating complex therapeutic interactions. Notably, the impact of the media composition, particularly serum free/ xeno free formulations, on tumor proliferation and apoptosis could offer a deeper understanding of how tumor-specific responses may interact with different treatment regimens.

As discussed earlier in section 4.10, expanding the sample size is imperative to study tumor-origin- and site-dependent variations in therapy response. Tumor heterogeneity, influenced by the anatomical location and cellular microenvironment, has been shown to affect biomarker expression and treatment outcomes. [83] This heterogeneity is particularly relevant in solid tumors like HNSCC, where the TME varies substantially across different sites, influencing both tumor behavior and treatment responses.[8, 87, 90] The variability in therapeutic outcomes may also be further exacerbated by the choice of culture media, as demonstrated by studies showing that StemMACS™ XF-based media can alter cellular behavior, including proliferation and immune responses, in cancer models. [119] For example, EGFR overexpression and apoptotic resistance, frequently observed in HNSCC, can modulate responses to cisplatin and RT. [16, 17] Expanding the sample size would help capture a more comprehensive range of tumor-specific variations, particularly when evaluating biomarkers such as EGFR, cleaved caspase-3, Ki-67, and PD-L1, which are site- and tumor-type-dependent. [63, 123] A broader sample set would enable the identification of molecular signatures associated with differential responses, thus providing deeper mechanistic insights that drive tumor-specific therapeutic outcomes.

A significant finding of this study was the downregulation of vimentin expression across all samples and media types following RCT (Figure 31). Vimentin, a canonical mesenchymal marker, is associated with EMT, which has been implicated in cancer progression, metastasis, and therapeutic resistance. [77, 105] The observed reduction in vimentin expression may reflect suppression of EMT pathways, potentially linked to RT-induced modulation of the TME. Studies by *Diepenbruck et al.* and *Dongre et al.* have highlighted the dynamic and reversible nature of EMT, with partial-EMT states often observed in site-specific tumor regions. [124, 125] This is consistent with reports suggesting that RCT can inhibit EMT by altering the expression of key transcription factors, such as ZEB1 and SNAIL, as well as downstream markers like vimentin. [125] To further elucidate the interplay between epithelial and mesenchymal states during treatment, future studies should incorporate single-cell transcriptomics and evaluate epithelial markers, such as E-cadherin, in conjunction with vimentin. [11, 72, 105]

A key achievement of this work was the establishment and validation of a xeno-free culture system for preclinical HNSCC research. The results demonstrated that xeno-free media- hPL and StemMACS™ XF-based formulations, can serve as viable alternatives to FBS-supplemented media, supporting the short-term growth and maintenance of HNSCC explants while preserving their structural and functional integrity over a 10-day culture period. This approach contributes to the development of fully humanized models that minimize reliance on animal-derived supplements.

Previous advancements in xeno-free culture systems, as reported by *Lensch et al.*, have emphasized their potential to improve cell viability and proliferation, particularly for mesenchymal cell cultures. [110] However, maintaining cellular heterogeneity and tissue complexity over extended culture periods remains a persistent challenge. Specifically, this is critical for personalized medicine applications, where accurate modeling of patient-specific tumor characteristics is essential. [126]

Building upon an established ex vivo HNSCC model, [63, 68] this study demonstrated that xeno-free media could sustain tissue cultures while partially recapitulating key features of primary tumors, including consistent PD-L1 and Ki-67 expression levels. However, challenges such as tissue contamination and limited sample availability persisted. Microbial contamination, particularly in oral cavity-derived tumors, remains as an inherent limitation due to their anatomical location and cannot be fully eliminated. In this study, contamination contributed to reduced viability of *ex vivo* samples, with only 30% of explants remaining viable, a challenge that has also been reported in other studies. [111] As discussed in section 4.9, addressing this issue will require the optimizing aseptic techniques to minimize contamination. Additionally, the establishment of multicentre cohort studies would not only enhance tissue availability but also facilitate the standardization of xeno-free protocols across research units, as highlighted by *Gstraunthaler et al.* [126, 127] Expanding the patient cohort size will be crucial for improving the statistical robustness of histochemical and molecular analyzes, enabling a more comprehensive characterization of PD-L1, vimentin, and E-cadherin expression dynamics during RCT.

Another critical future direction is the transition of all experimental components to xeno-free alternatives, including antibodies and supplements, while systematically comparing these approaches to conventional methods, such as H&E and IHC staining. This transition will be essential for fully utilising the clinical translatability of xeno-free and humanized models.

Although considerable work remains in this area, the xeno-free HNSCC explant model established in this study represents a significant advancement in the development of humanized culture systems with enhanced clinical relevance. Its potential as a platform for drug sensitivity testing and the development of novel therapeutic strategies underscores its value for precision medicine. By addressing the current challenges and building on the findings presented here, this model could play a pivotal role in the broader effort to establish fully humanized and clinically translatable HNSCC systems.

In the future, transitioning the already established 3D bioprinted HNSCC model to xeno-free media could further advance its applicability in precision medicine. Such a development would enhance its utility as a humanized preclinical system, enabling the evaluation of drug efficacy and therapy resistance in a setting that closely replicates native tumor biology.

5. SUMMARY

This thesis demonstrates the successful establishment of a long-term culturable 3D bioprinted HNSCC model using NC bioinks. The study provides evidence that HNSCC cells, derived from different anatomical sites, exhibit distinct behaviors when bioprinted in various NC and gelatin-based bioinks. Using Ki-67 and E-cadherin IF staining, it was confirmed that these cells could sustain proliferation and preserve intrinsic cellular characteristics within bioprinted constructs for up to 21 days. Tunicate-derived Carboxy-NC bioink demonstrated comparable outcomes to GelMA bioink and was effective in supporting the proliferation of both HNSCC and breast cancer (MCF-7) cells, signifying its versatility. Importantly, all tested cell lines survived the bioprinting process. Variations in their viability might reflect potential correlations with tumor-specific characteristics such as metastatic potential or tumor mitotic rate (TMR).

A significant contribution of this thesis is the optimization of NC bioinks tailored to epithelial and stromal cells within the HNSCC TME. While epithelial cells preferred Carboxy-NC, stromal cells such as cancer-associated fibroblasts favored TEMPO-NC, as revealed by SEM analysis. However, limitations such as suboptimal tumor-to-stromal cell ratios might have influenced the outcomes. Future refinements must be directed towards scaling down model dimensions and enhancing stromal cell density to better replicate native tumor conditions.

Bioink modifications such as functionalization with adhesion promoting ligands such as RGD peptides could enhance multicellular interactions while maintaining bioink compatibility and shape fidelity. NC-based hydrogels present significant advantages, including tunability, stability, and reduced contamination risks, positioning them as a promising alternative for constructing clinically relevant HNSCC models as opposed to GelMAA. [61, 62]

Functional validation of the 3D bioprinted model using RCT treatment revealed responses resembling *in vivo* behavior. Patient-derived HNSCC cells exhibited bioprintability and consistent growth behavior over 10 days. Notably, drug response assays indicated that the bioprinted model better reflected *in vivo* drug efficacy compared to 3D spheroid models, which tended to overestimate drug toxicity.

Given the xeno-free HNSCC explant model portrayed comparable behavior to FBS-grown tissues, future work will focus on advancing this xeno-free, humanized model for translational applications. By incorporating patient-derived cells and evaluating responses to therapeutic interventions, the established bioprinted model in NC-bioink holds significant potential as a robust platform for personalized therapeutic testing and the development of novel strategies for HNSCC treatment.

Future Perspectives

The model demonstrates significant promise as a high-throughput platform for drug efficacy and toxicology studies, offering functional relevance through its response to clinical treatment regimens like radiochemotherapy. Despite this progress, further advancements are essential to enhance the physiological complexity, scalability, and translational potential of the model.

Future research should prioritize incorporating advanced cellular components to better replicate the TME. Integration of immune cells, cancer-associated fibroblasts, and endothelial cells will improve cellular heterogeneity and physiological accuracy. Moreover, reproducing key biochemical and mechanical cues, such as gradients of signalling molecules and ECM stiffness, is vital for studying tumor progression and therapy resistance. Transitioning the current static model into a dynamic system, such as combining microfluidic technologies, will facilitate real-time analysis of cell-to-cell and cell-to-matrix interactions. [25, 39, 42]

Establishing functional vasculature within the bioprinted constructs remains a critical challenge. Developing a vascular network to supply nutrients and oxygen mightenhance the model’s utility for studying intra- and inter-tissue transport mechanisms. [25, 39, 42] This step would require iterative optimization of bioink formulations and bioprinting parameters to accommodate the diverse needs of multicellular systems, maintaining a balance between increased complexity and usability.

Another priority is exploring xeno-free culture systems to improve the translational relevance of preclinical tools. Transferring the model to a xeno-free one would eliminate potential biases introduced by animal-derived components, paving the way for more humanized models. [28, 29, 112, 126] Immediate next steps include refining cell-specific bioink formulations, optimizing cell densities, and tailoring printing parameters to align with the TME's native structure and function. [44-46, 48, 59, 95]

While this thesis established a proof-of-concept for bioprinted HNSCC models, further advancements are necessary to expand their application in precision medicine. Enhancing functional assessments and exploring personalized therapeutic responses using patient-derived cells will improve the predictiveness of the heterotypic model. [2, 37] These efforts will not only deepen the understanding of tumor biology but also drive the development of effective, personalized therapeutic strategies for HNSCC.

In conclusion, the tunicate-derived NC-based 3D bioprinted HNSCC model represents a significant step forward in preclinical cancer research. By addressing the outlined challenges and opportunities, this model can bridge the gap between experimental systems and clinical reality, providing a robust platform for advancing precision medicine and improving patient outcomes.

6. REFERENCES

[1]Arutyunyan I, Jumaniyazova E, Makarov A, Fatkhudinov T. In Vitro Models of Head and Neck Cancer: From Primitive to Most Advanced. Journal of Personalized Medicine. 2023;13(11):1575.

[2]Chaves P, Garrido M, Oliver J, Pérez-Ruiz E, Barragan I, Rueda-Domínguez A. Preclinical models in head and neck squamous cell carcinoma. British Journal of Cancer. 2023;128(10):1819-27.

[3]Bonartsev AP, Lei B, Kholina MS, Menshikh KA, Svyatoslavov DS, Samoylova SI, et al. Models of head and neck squamous cell carcinoma using bioengineering approaches. Critical Reviews in Oncology/Hematology. 2022;175:103724.

[4]Affolter A, Lammert A, Kern J, Scherl C, Rotter N. Precision Medicine Gains Momentum: Novel 3D Models and Stem Cell-Based Approaches in Head and Neck Cancer. Frontiers in Cell and Developmental Biology. 2021;9.

[5]Mody MD, Rocco JW, Yom SS, Haddad RI, Saba NF. Head and neck cancer. The Lancet. 2021;398(10318):2289-99.

[6]Johnson DE, Burtness B, Leemans CR, Lui VWY, Bauman JE, Grandis JR. Head and neck squamous cell carcinoma. Nature Reviews Disease Primers. 2020;6(1):92.

[7]Wang G, Zhang M, Cheng M, Wang X, Li K, Chen J, et al. Tumor microenvironment in head and neck squamous cell carcinoma: Functions and regulatory mechanisms. Cancer Letters. 2021;507:55-69.

[8]Canning M, Guo G, Yu M, Myint C, Groves MW, Byrd JK, et al. Heterogeneity of the Head and Neck Squamous Cell Carcinoma Immune Landscape and Its Impact on Immunotherapy. Frontiers in Cell and Developmental Biology. 2019;7.

[9]Zhou T, Huang W, Wang X, Zhang J, Zhou E, Tu Y, et al. Global burden of head and neck cancers from 1990 to 2019. iScience. 2024;27(3).

[10]Curry JM, Sprandio J, Cognetti D, Luginbuhl A, Bar-ad V, Pribitkin E, et al. Tumor Microenvironment in Head and Neck Squamous Cell Carcinoma. Seminars in Oncology. 2014;41(2):217-34.

[11]Guan Z, Liu J, Zheng L. Effect of radiotherapy on head and neck cancer tissues in patients receiving radiotherapy: a bioinformatics analysis-based study. Sci Rep. 2024;14(1):6304.

[12]Baker-Groberg SM, Bornstein S, Zilberman-Rudenko J, Schmidt M, Tormoen GW, Kernan C, et al. Effect of Ionizing Radiation on the Physical Biology of Head and Neck Squamous Cell Carcinoma Cells. Cellular and Molecular Bioengineering. 2015;8(3):517-25.

[13]Mei Z, Huang J, Qiao B, Lam AK-y. Immune checkpoint pathways in immunotherapy for head and neck squamous cell carcinoma. International Journal of Oral Science. 2020;12(1):16.

[14]Zamulaeva I, Matchuk O, Selivanova E, Mkrtchian L, Yakimova A, Gusarova V, et al. Effects of Fractionated Radiation Exposure on Vimentin Expression in Cervical Cancers: Analysis of Association with Cancer Stem Cell Response and Short-Term Prognosis. International Journal of Molecular Sciences [Internet]. 2023; 24(4).

[15]Zhou Q, Liu S, Kou Y, Yang P, Liu H, Hasegawa T, et al. ATP Promotes Oral Squamous Cell Carcinoma Cell Invasion and Migration by Activating the PI3K/AKT Pathway via the P2Y2-Src-EGFR Axis. ACS Omega. 2022;7(44):39760-71.

[16]Rong C, Muller MF, Xiang F, Jensen A, Weichert W, Major G, et al. Adaptive ERK signalling activation in response to therapy and in silico prognostic evaluation of EGFR-MAPK in HNSCC. British Journal of Cancer. 2020;123(2):288-97.

[17]Hutchinson M-KND, Mierzwa M, D’Silva NJ. Radiation resistance in head and neck squamous cell carcinoma: dire need for an appropriate sensitizer. Oncogene. 2020;39(18):3638-49.

[18]Steen S, Semmelmayer K, Flechtenmacher C, Hoffmann J, Freier K, Horn D, et al. Dynamic Up-Regulation of PD-L1 in the Progression of Oral Squamous Cell Carcinoma. International Journal of Molecular Sciences [Internet]. 2023; 24(22).

[19]Elmusrati A, Wang J, Wang C-Y. Tumor microenvironment and immune evasion in head and neck squamous cell carcinoma. International Journal of Oral Science. 2021;13(1):24.

[20]Quail DF, Joyce JA. Microenvironmental regulation of tumor progression and metastasis. Nature Medicine. 2013;19(11):1423-37.

[21]Peltanova B, Raudenska M, Masarik M. Effect of tumor microenvironment on pathogenesis of the head and neck squamous cell carcinoma: a systematic review. Molecular Cancer. 2019;18(1):63.

[22]Neufeld L, Yeini E, Pozzi S, Satchi-Fainaro R. 3D bioprinted cancer models: from basic biology to drug development. Nature Reviews Cancer. 2022;22(12):679-92.

[23]Méry B, Rancoule C, Guy J-B, Espenel S, Wozny A-S, Battiston-Montagne P, et al. Preclinical models in HNSCC: A comprehensive review. Oral Oncology. 2017;65:51-6.

[24]Bernal PN. Crafting Tissue Complexity: Pioneering Layerwise and Volumetric Biofabrication Strategies for Advanced In Vitro Models. UMC Repository: Utrecht University; 2024.

[25]Augustine R, Kalva SN, Ahmad R, Zahid AA, Hasan S, Nayeem A, et al. 3D Bioprinted cancer models: Revolutionizing personalized cancer therapy. Translational Oncology. 2021;14(4):101015.

[26]Meng F, Meyer CM, Joung D, Vallera DA, McAlpine MC, Panoskaltsis-Mortari A. 3D Bioprinted In Vitro Metastatic Models via Reconstruction of Tumor Microenvironments. Advanced Materials. 2019;31(10):1806899.

[27]Graham ML, Prescott MJ. The multifactorial role of the 3Rs in shifting the harm-benefit analysis in animal models of disease. European Journal of Pharmacology. 2015;759:19-29.

[28]Duarte AC, Costa EC, Filipe HAL, Saraiva SM, Jacinto T, Miguel SP, et al. Animal-derived products in science and current alternatives. Biomaterials Advances. 2023;151:213428.

[29]Grimm H, Biller-Andorno N, Buch T, Dahlhoff M, Davies G, Cederroth CR, et al. Advancing the 3Rs: innovation, implementation, ethics and society. Frontiers in Veterinary Science. 2023;10.

[30]Cederroth CR, Sandström J. Editorial: Towards a new 3Rs era in experimental research. Frontiers in Behavioral Neuroscience. 2024;18.

[31]Melissaridou S, Wiechec E, Magan M, Jain MV, Chung MK, Farnebo L, et al. The effect of 2D and 3D cell cultures on treatment response, EMT profile and stem cell features in head and neck cancer. Cancer Cell International. 2019;19(1):16.

[32]Kapałczyńska M, Kolenda T, Przybyła W, Zajączkowska M, Teresiak A, Filas V, et al. 2D and 3D cell cultures – a comparison of different types of cancer cell cultures. Arch Med Sci. 2018;14(4):910-9.

[33]Apelgren P, Sämfors S, Säljö K, Mölne J, Gatenholm P, Troedsson C, et al. Biomaterial and biocompatibility evaluation of tunicate nanocellulose for tissue engineering. Biomaterials Advances. 2022;137:212828.

[34]Adriani G, Cappello P, Lovisa S. Editorial: Preclinical models and emerging technologies to study the effects of the tumor microenvironment on cancer heterogeneity and drug resistance. Frontiers in Oncology. 2023;13.

[35]Foglietta F, Serpe L, Canaparo R. The Effective Combination between 3D Cancer Models and Stimuli-Responsive Nanoscale Drug Delivery Systems. Cells. 2021;10(12):3295.

[36]Bērziņa S, Harrison A, Taly V, Xiao W. Technological Advances in Tumor-On-Chip Technology: From Bench to Bedside. Cancers [Internet]. 2021; 13(16).

[37]Law AMK, Rodriguez de la Fuente L, Grundy TJ, Fang G, Valdes-Mora F, Gallego-Ortega D. Advancements in 3D Cell Culture Systems for Personalizing Anti-Cancer Therapies. Frontiers in Oncology. 2021;11.

[38]Arakaki AKS, Szulzewsky F, Gilbert MR, Gujral TS, Holland EC. Utilizing preclinical models to develop targeted therapies for rare central nervous system cancers. Neuro-Oncology. 2021;23(Supplement_5):S4-S15.

[39]Datta P, Dey M, Ataie Z, Unutmaz D, Ozbolat IT. 3D bioprinting for reconstituting the cancer microenvironment. npj Precision Oncology. 2020;4(1):18.

[40]Heinrich MA, Liu W, Jimenez A, Yang J, Akpek A, Liu X, et al. 3D Bioprinting: from Benches to Translational Applications. Small. 2019;15(23):1805510.

[41]Bojin F, Robu A, Bejenariu MI, Ordodi V, Olteanu E, Cean A, et al. 3D Bioprinting of Model Tissues That Mimic the Tumor Microenvironment. Micromachines. 2021;12(5):535.

[42]Parodi I, Di Lisa D, Pastorino L, Scaglione S, Fato MM. 3D Bioprinting as a Powerful Technique for Recreating the Tumor Microenvironment. Gels [Internet]. 2023; 9(6).

[43]Schwab A, Levato R, D'Este M, Piluso S, Eglin D, Malda J. Printability and Shape Fidelity of Bioinks in 3D Bioprinting. Chemical Reviews. 2020;120(19):11028-55.

[44]Hölzl K, Lin S, Tytgat L, Van Vlierberghe S, Gu L, Ovsianikov A. Bioink properties before, during and after 3D bioprinting. Biofabrication. 2016;8(3):032002.

[45]Gillispie GJ, Han A, Uzun-Per M, Fisher J, Mikos AG, Niazi MKK, et al. The Influence of Printing Parameters and Cell Density on Bioink Printing Outcomes. Tissue Engineering Part A. 2020;26(23-24):1349-58.

[46]Webb B, Doyle BJ. Parameter optimization for 3D bioprinting of hydrogels. Bioprinting. 2017;8:8-12.

[47]Mancha Sánchez E, Gómez-Blanco JC, López Nieto E, Casado JG, Macías-García A, Díaz Díez MA, et al. Hydrogels for Bioprinting: A Systematic Review of Hydrogels Synthesis, Bioprinting Parameters, and Bioprinted Structures Behavior. Frontiers in Bioengineering and Biotechnology. 2020;8.

[48]Deo KA, Singh KA, Peak CW, Alge DL, Gaharwar AK. Bioprinting 101: Design, Fabrication, and Evaluation of Cell-Laden 3D Bioprinted Scaffolds. Tissue Engineering Part A. 2020;26(5-6):318-38.

[49]Kim H, Dutta SD, Randhawa A, Patil TV, Ganguly K, Acharya R, et al. Recent advances and biomedical application of 3D printed nanocellulose-based adhesive hydrogels: A review. International Journal of Biological Macromolecules. 2024;264:130732.

[50]Liu D, Meng Q, Hu J. Bacterial Nanocellulose Hydrogel: A Promising Alternative Material for the Fabrication of Engineered Vascular Grafts. Polymers. 2023;15(18):3812.

[51]Patil TV, Patel DK, Dutta SD, Ganguly K, Santra TS, Lim K-T. Nanocellulose, a versatile platform: From the delivery of active molecules to tissue engineering applications. Bioactive Materials. 2022;9:566-89.

[52]Huo Y, Liu Y, Xia M, Du H, Lin Z, Li B, et al. Nanocellulose-Based Composite Materials Used in Drug Delivery Systems. Polymers. 2022;14(13):2648.

[53]Thakur V, Guleria A, Kumar S, Sharma S, Singh K. Recent advances in nanocellulose processing, functionalization and applications: a review. Materials Advances. 2021;2(6):1872-95.

[54]Raghav N, Sharma MR, Kennedy JF. Nanocellulose: A mini-review on types and use in drug delivery systems. Carbohydrate Polymer Technologies and Applications. 2021;2:100031.

[55]Wang X, Wang Q, Xu C. Nanocellulose-Based Inks for 3D Bioprinting: Key Aspects in Research Development and Challenging Perspectives in Applications—A Mini Review. Bioengineering [Internet]. 2020; 7(2).

[56]Bacakova L, Pajorova J, Bacakova M, Skogberg A, Kallio P, Kolarova K, et al. Versatile Application of Nanocellulose: From Industry to Skin Tissue Engineering and Wound Healing. Nanomaterials. 2019;9(2):164.

[57]Martínez Ávila H, Schwarz S, Rotter N, Gatenholm P. 3D bioprinting of human chondrocyte-laden nanocellulose hydrogels for patient-specific auricular cartilage regeneration. Bioprinting. 2016;1-2:22-35.

[58]Choi SY, Shim J, Gu D-e, Kim SY, Kim HJ, Shin D-Y, et al. Clonal evolution of long-term expanding head and neck cancer organoid: Impact on treatment response for personalized therapeutic screening. Oral Oncology. 2023;146:106571.

[59]GhavamiNejad A, Ashammakhi N, Wu XY, Khademhosseini A. Crosslinking Strategies for 3D Bioprinting of Polymeric Hydrogels. Small. 2020;16(35):2002931.

[60]Davern JW, Hipwood L, Bray LJ, Meinert C, Klein TJ. Addition of Laponite to gelatin methacryloyl bioinks improves the rheological properties and printability to create mechanically tailorable cell culture matrices. APL Bioengineering. 2024;8(1).

[61]Kort-Mascort J, Shen ML, Martin E, Flores-Torres S, Pardo LA, Siegel PM, et al. Bioprinted cancer-stromal in-vitro models in a decellularized ECM-based bioink exhibit progressive remodeling and maturation. Biomedical Materials. 2023;18(4):045022.

[62]Kort-Mascort J, Bao G, Elkashty O, Flores-Torres S, Munguia-Lopez JG, Jiang T, et al. Decellularized Extracellular Matrix Composite Hydrogel Bioinks for the Development of 3D Bioprinted Head and Neck in Vitro Tumor Models. ACS Biomaterials Science & Engineering. 2021;7(11):5288-300.

[63]Affolter A, Liebel K, Tengler L, Seiz E, Tiedtke M, Azhakesan A, et al. Modulation of PD-L1 expression by standard therapy in head and neck cancer cell lines and exosomes. Int J Oncol. 2023;63(3):102.

[64]Brenner JC, Graham MP, Kumar B, Saunders LM, Kupfer R, Lyons RH, et al. Genotyping of 73 UM-SCC head and neck squamous cell carcinoma cell lines. Head & Neck. 2010;32(4):417-26.

[65]Missoum K, Belgacem MN, Bras J. Nanofibrillated Cellulose Surface Modification: A Review. Materials [Internet]. 2013; 6(5):[1745-66 pp.].

[66]Nikolits I, Radwan S, Liebner F, Dietrich W, Egger D, Chariyev-Prinz F, et al. Hydrogels from TEMPO-Oxidized Nanofibrillated Cellulose Support In Vitro Cultivation of Encapsulated Human Mesenchymal Stem Cells. ACS Applied Bio Materials. 2023;6(2):543-51.

[67]Pepelanova I, Kruppa K, Scheper T, Lavrentieva A. Gelatin-Methacryloyl (GelMA) Hydrogels with Defined Degree of Functionalization as a Versatile Toolkit for 3D Cell Culture and Extrusion Bioprinting. Bioengineering. 2018;5(3):55.

[68]Affolter A, Muller M-F, Sommer K, Stenzinger A, Zaoui K, Lorenz K, et al. Targeting irradiation-induced mitogen-activated protein kinase activation in vitro and in an ex vivo model for human head and neck cancer. Head & Neck. 2016;38(S1):E2049-E61.

[69]Bieback K, Fernandez-MuÑOz B, Pati S, SchÄFer R. Gaps in the knowledge of human platelet lysate as a cell culture supplement for cell therapy: a joint publication from the AABB and the International Society for Cell & Gene Therapy. Cytotherapy. 2019;21(9):911-24.

[70]Bieback K. Platelet Lysate as Replacement for Fetal Bovine Serum in Mesenchymal Stromal Cell Cultures. Transfusion Medicine and Hemotherapy. 2013;40(5):326-35.

[71]Hojat N, Gentile P, Ferreira AM, Šiller L. Automatic pore size measurements from scanning electron microscopy images of porous scaffolds. Journal of Porous Materials. 2023;30(1):93-101.

[72]Jhaveri N, Ben Cheikh B, Nikulina N, Ma N, Klymyshyn D, DeRosa J, et al. Mapping the Spatial Proteome of Head and Neck Tumors: Key Immune Mediators and Metabolic Determinants in the Tumor Microenvironment. GEN Biotechnology. 2023;2(5):418-34.

[73]Cheng J, Lin F, Liu H, Yan Y, Wang X, Zhang R, et al. Rheological Properties of Cell-Hydrogel Composites Extruding Through Small-Diameter Tips. Journal of Manufacturing Science and Engineering. 2008;130(2).

[74]Vernerey FJ, Lalitha Sridhar S, Muralidharan A, Bryant SJ. Mechanics of 3D Cell–Hydrogel Interactions: Experiments, Models, and Mechanisms. Chemical Reviews. 2021;121(18):11085-148.

[75]Azhakesan A, Kern J, Mishra A, Selhuber-Unkel C, Affolter A, Gatenholm P, et al. 3D Bioprinted Head and Neck Squamous Cell Carcinoma (HNSCC) Model Using Tunicate Derived Nanocellulose (NC) Bioink. Advanced Healthcare Materials. 2025;n/a(n/a):2403114.

[76]Akinleye A, Rasool Z. Immune checkpoint inhibitors of PD-L1 as cancer therapeutics. Journal of Hematology & Oncology. 2019;12(1):92.

[77]Brylka S, Böhrnsen F. EMT and Tumor Turning Point Analysis in 3D Spheroid Culture of HNSCC and Mesenchymal Stem Cells. Biomedicines. 2022;10(12):3283.

[78]Engelmann L, Thierauf J, Koerich Laureano N, Stark H-J, Prigge E-S, Horn D, et al. Organotypic Co-Cultures as a Novel 3D Model for Head and Neck Squamous Cell Carcinoma. Cancers [Internet]. 2020; 12(8).

[79]Huang Y, Huang Z, Tang Z, Chen Y, Huang M, Liu H, et al. Research Progress, Challenges, and Breakthroughs of Organoids as Disease Models. Frontiers in Cell and Developmental Biology. 2021;9.

[80]Fernandez-Rebollo E, Mentrup B, Ebert R, Franzen J, Abagnale G, Sieben T, et al. Human Platelet Lysate versus Fetal Calf Serum: These Supplements Do Not Select for Different Mesenchymal Stromal Cells. Sci Rep. 2017;7(1):5132.

[81]Panella S, Muoio F, Jossen V, Harder Y, Eibl-Schindler R, Tallone T. Chemically Defined Xeno- and Serum-Free Cell Culture Medium to Grow Human Adipose Stem Cells. Cells [Internet]. 2021; 10(2).

[82]González Hernández Y, Fischer RW. Serum-free culturing of mammalian cells - adaptation to and cryopreservation in fully defined media. ALTEX - Alternatives to animal experimentation. 2007;24(2):110-6.

[83]Glastonbury CM, Parker EE, Hoang JK. The Postradiation Neck: Evaluating Response to Treatment and Recognizing Complications. American Journal of Roentgenology. 2010;195(2):W164-W71.

[84]Seshadri M, Merzianu M, Tang H, Rigual NR, Sullivan-Nasca M, Loree TR, et al. Establishment and characterization of patient tumor-derived head and neck squamous cell carcinoma xenografts. Cancer Biology & Therapy. 2009;8(23):2273-81.

[85]Kurzyk A, Szumera-Ciećkiewicz A, Miłoszewska J, Chechlińska M. 3D modeling of normal skin and cutaneous squamous cell carcinoma. A comparative study in 2D cultures, spheroids, and 3D bioprinted systems. Biofabrication. 2024;16(2):025021.

[86]Pössl A, Hartzke D, Schmidts TM, Runkel FE, Schlupp P. A targeted rheological bioink development guideline and its systematic correlation with printing behavior. Biofabrication. 2021;13(3):035021.

[87]Galber C, Acosta MJ, Minervini G, Giorgio V. The role of mitochondrial ATP synthase in cancer. 2020;401(11):1199-214.

[88]Li W-C, Huang C-H, Hsieh Y-T, Chen T-Y, Cheng L-H, Chen C-Y, et al. Regulatory Role of Hexokinase 2 in Modulating Head and Neck Tumorigenesis. Frontiers in Oncology. 2020;10.

[89]Kamarajan P, Rajendiran TM, Kinchen J, Bermúdez M, Danciu T, Kapila YL. Head and Neck Squamous Cell Carcinoma Metabolism Draws on Glutaminolysis, and Stemness Is Specifically Regulated by Glutaminolysis via Aldehyde Dehydrogenase. Journal of Proteome Research. 2017;16(3):1315-26.

[90]Li Q, Tie Y, Alu A, Ma X, Shi H. Targeted therapy for head and neck cancer: signaling pathways and clinical studies. Signal Transduction and Targeted Therapy. 2023;8(1):31.

[91]Lin N, Dufresne A. Nanocellulose in biomedicine: Current status and future prospect. European Polymer Journal. 2014;59:302-25.

[92]Liu J, Cheng F, Grénman H, Spoljaric S, Seppälä J, E. Eriksson J, et al. Development of nanocellulose scaffolds with tunable structures to support 3D cell culture. Carbohydrate Polymers. 2016;148:259-71.

[93]Kupnik K, Primožič M, Kokol V, Leitgeb M. Nanocellulose in Drug Delivery and Antimicrobially Active Materials. Polymers [Internet]. 2020; 12(12).

[94]Lv B, Lu L, Hu L, Cheng P, Hu Y, Xie X, et al. Recent advances in GelMA hydrogel transplantation for musculoskeletal disorders and related disease treatment. Theranostics. 2023;13(6):2015-39.

[95]Paxton N, Smolan W, Böck T, Melchels F, Groll J, Jungst T. Proposal to assess printability of bioinks for extrusion-based bioprinting and evaluation of rheological properties governing bioprintability. Biofabrication. 2017;9(4):044107.

[96]Almangush A, Alabi RO, Troiano G, Coletta RD, Salo T, Pirinen M, et al. Clinical significance of tumor-stroma ratio in head and neck cancer: a systematic review and meta-analysis. BMC Cancer. 2021;21(1):480.

[97]Kaufmann J, Haist M, Kur I-M, Zimmer S, Hagemann J, Matthias C, et al. Tumor-stroma contact ratio - a novel predictive factor for tumor response to chemoradiotherapy in locally advanced oropharyngeal cancer. Translational Oncology. 2024;46:102019.

[98]Ho NCW, Yap JYY, Zhao Z, Wang Y, Fernando K, Li CH, et al. Bioengineered Hydrogels Recapitulate Fibroblast Heterogeneity in Cancer. Advanced Science. 2024;11(20):2307129.

[99]Spratte T, Geiger S, Colombo F, Mishra A, Taale M, Hsu L-Y, et al. Increasing the Efficiency of Thermoresponsive Actuation at the Microscale by Direct Laser Writing of pNIPAM. Advanced Materials Technologies. 2023;8(1):2200714.

[100]Raic A, Rödling L, Kalbacher H, Lee-Thedieck C. Biomimetic macroporous PEG hydrogels as 3D scaffolds for the multiplication of human hematopoietic stem and progenitor cells. Biomaterials. 2014;35(3):929-40.

[101]Siemsen K, Rajput S, Rasch F, Taheri F, Adelung R, Lammerding J, et al. Tunable 3D Hydrogel Microchannel Networks to Study Confined Mammalian Cell Migration. Advanced Healthcare Materials. 2021;10(23):2100625.

[102]Donaldson AR, Tanase CE, Awuah D, Vasanthi Bathrinarayanan P, Hall L, Nikkhah M, et al. Photocrosslinkable Gelatin Hydrogels Modulate the Production of the Major Pro-inflammatory Cytokine, TNF-α, by Human Mononuclear Cells. Frontiers in Bioengineering and Biotechnology. 2018;6.

[103]Maharjan S, Ma C, Singh B, Kang H, Orive G, Yao J, et al. Advanced 3D imaging and organoid bioprinting for biomedical research and therapeutic applications. Advanced Drug Delivery Reviews. 2024;208:115237.

[104]Pawlicka M, Gumbarewicz E, Błaszczak E, Stepulak A. Transcription Factors and Markers Related to Epithelial–Mesenchymal Transition and Their Role in Resistance to Therapies in Head and Neck Cancers. Cancers [Internet]. 2024; 16(7).

[105]Pal A, Barrett TF, Paolini R, Parikh A, Puram SV. Partial EMT in head and neck cancer biology: a spectrum instead of a switch. Oncogene. 2021;40(32):5049-65.

[106]Antonelli F. 3D Cell Models in Radiobiology: Improving the Predictive Value of In Vitro Research. International Journal of Molecular Sciences. 2023;24(13):10620.

[107]Spałek MJ, Bochyńska A, Borkowska A, Mroczkowski P, Szostakowski B. Challenges and solutions in 3D printing for oncology: a narrative review. Chinese Clinical Oncology. 2024;13(4):49.

[108]Mei Y, Lakotsenina E, Wegner M, Hehne T, Krause D, Hakimeh D, et al. Three-Dimensional-Bioprinted Non-Small Cell Lung Cancer Models in a Mouse Phantom for Radiotherapy Research. International Journal of Molecular Sciences [Internet]. 2024; 25(19).

[109]Liu S, Liu L, Ye W, Ye D, Wang T, Guo W, et al. High Vimentin Expression Associated with Lymph Node Metastasis and Predicated a Poor Prognosis in Oral Squamous Cell Carcinoma. Sci Rep. 2016;6(1):38834.

[110]Lensch M, Muise A, White L, Badowski M, Harris D. Comparison of Synthetic Media Designed for Expansion of Adipose-Derived Mesenchymal Stromal Cells. Biomedicines [Internet]. 2018; 6(2).

[111]Sharon S, Duhen T, Bambina S, Baird J, Leidner R, Bell B, et al. Explant Modeling of the Immune Environment of Head and Neck Cancer. Frontiers in Oncology. 2021;11.

[112]Kachroo U, Zachariah SM, Thambaiah A, Tabasum A, Livingston A, Rebekah G, et al. Comparison of Human Platelet Lysate versus Fetal Bovine Serum for Expansion of Human Articular Cartilage–Derived Chondroprogenitors. CARTILAGE. 2020;13(2_suppl):107S-16S.

[113]Basnayake BWMTJ, Leo P, Rao S, Vasani S, Kenny L, Haass NK, et al. Head and neck cancer patient-derived tumouroid cultures: opportunities and challenges. British Journal of Cancer. 2023;128(10):1807-18.

[114]Ock C-Y, Kim S, Keam B, Kim S, Ahn Y-O, Chung E-J, et al. Changes in programmed death-ligand 1 expression during cisplatin treatment in patients with head and neck squamous cell carcinoma. Oncotarget. 2017;8(58).

[115]Abuzeid WM, Davis S, Tang AL, Saunders L, Brenner JC, Lin J, et al. Sensitization of Head and Neck Cancer to Cisplatin Through the Use of a Novel Curcumin Analog. Archives of Otolaryngology–Head & Neck Surgery. 2011;137(5):499-507.

[116]Cui J-W, Li Y, Yang Y, Yang H-K, Dong J-M, Xiao Z-H, et al. Tumor immunotherapy resistance: Revealing the mechanism of PD-1 / PD-L1-mediated tumor immune escape. Biomedicine & Pharmacotherapy. 2024;171:116203.

[117]Lin W, Chen M, Hong L, Zhao H, Chen Q. Crosstalk Between PD-1/PD-L1 Blockade and Its Combinatorial Therapies in Tumor Immune Microenvironment: A Focus on HNSCC. Frontiers in Oncology. 2018;8.

[118]Wang H-C, Chan L-P, Cho S-F. Targeting the Immune Microenvironment in the Treatment of Head and Neck Squamous Cell Carcinoma. Frontiers in Oncology. 2019;9.

[119]Jakl V, Popp T, Haupt J, Port M, Roesler R, Wiese S, et al. Effect of Expansion Media on Functional Characteristics of Bone Marrow-Derived Mesenchymal Stromal Cells. Cells. 2023;12(16):2105.

[120]Kwang Chae Y, Arya A, Chiec L, Shah H, Rosenberg A, Patel S, et al. Challenges and future of biomarker tests in the era of precision oncology: Can we rely on immunohistochemistry (IHC) or fluorescence in situ hybridization (FISH) to select the optimal patients for matched therapy? Oncotarget. 2017;8(59).

[121]Jung EK, Chu T-H, Vo M-C, Nguyen HPQ, Lee DH, Lee JK, et al. Natural killer cells have a synergistic anti-tumor effect in combination with chemoradiotherapy against head and neck cancer. Cytotherapy. 2022;24(9):905-15.

[122]Ward MC, Koyfman SA, Bakst RL, Margalit DN, Beadle BM, Beitler JJ, et al. Retreatment of Recurrent or Second Primary Head and Neck Cancer After Prior Radiation: Executive Summary of the American Radium Society Appropriate Use Criteria. International Journal of Radiation Oncology, Biology, Physics. 2022;113(4):759-86.

[123]Lin CJ, Grandis JR, Carey TE, Gollin SM, Whiteside TL, Koch WM, et al. Head and neck squamous cell carcinoma cell lines: Established models and rationale for selection. Head & Neck. 2007;29(2):163-88.

[124]Diepenbruck M, Christofori G. Epithelial–mesenchymal transition (EMT) and metastasis: yes, no, maybe? Current Opinion in Cell Biology. 2016;43:7-13.

[125]Dongre A, Weinberg RA. New insights into the mechanisms of epithelial–mesenchymal transition and implications for cancer. Nature Reviews Molecular Cell Biology. 2019;20(2):69-84.

[126]Rauch C, Feifel E, Amann E-M, Spötl HP, Schennach H, Pfaller W, et al. Alternatives to the use of fetal bovine serum: Human platelet lysates as a serum substitute in cell culture media. ALTEX - Alternatives to animal experimentation. 2011;28(4):305-16.

[127]Gstraunthaler G, Lindl T, van der Valk J. A plea to reduce or replace fetal bovine serum in cell culture media. Cytotechnology. 2013;65(5):791-3.

7. APPENDIX

Information A1. Biochemical properties of the hydrogels

Table 11 provides a comprehensive overview of the key differences among the three hydrogels utilized in this thesis. It includes detailed information on their functional groups, zeta potentials, surface area, viscosity, bioburden, endotoxin levels, drug-loading capacity, biocompatibility, and biodegradability, as well as their specific applications. These data were sourced from the product descriptions provided by the respective manufacturers, Ocean TUNICELL (Norway) and CELLINK (Sweden). References to the product descriptions are included below for further details.

- TTC hydrogel- https://oceantunicell.com/wp-content/uploads/2021/08/MSDS-TTCM-version-2-170821.pdf
- CTC hydrogel- https://oceantunicell.com/wp-content/uploads/2021/08/MSDS-TTCM-version-2-170821.pdf
- GelMAA hydrogel- https://www.cellink.com/wpcontent/uploads/2022/03/GelMA-A-SDS-12-July-2019-4.pdf

BIOGRAPHY

ALEXYA AZHAKESAN

• Mannheim- 68165, Germany • +49 151 45947204
•alexya0695@gmail.com • LinkedIn • Publications

I am a passionate researcher specializing in 3D bioprinting, tissue engineering, and bionanofabrication, with a strong focus on developing functional in vitro disease models for drug discovery and precision medicine. My work is dedicated to translating biofabricated models into physiologically relevant tissues for preclinical drug testing, bridging the gap between experimental research and clinical setting.

RESEARCH EXPERIENCE

DOCTORAL STUDENT

Department Otorhinolaryngology, Head and Neck surgery (HNO), Medical Faculty of Mannheim, University of Heidelberg, Germany **(07/2021- 03/2025)**

- Designed, established, and optimized homotypic 3D bioprinted and xeno-free explant head and neck squamous cell carcinoma model for high-throughput drug testing and advanced the 3D bioprinted model to heterotypic one.

MASTER THESIS SCHOLAR

AMBER Research Group, Department of Biomedical Engineering (DBE), University of Twente, the Netherlands **(01- 08/2020)**

- Designed, established, and optimized heterotypic hepatocellular carcinoma 3D spheroid model to evaluate and enhance the penetration of drug functionalized nanoparticles.

GRADUATE RESEARCH ASSISTANT

Department of Politie, the Netherlands and Advanced Forensics Technology (AFT) Research Group, Saxion University of Applied Sciences, the Netherlands **(04- 09/2019)**

- Surface functionalized SDE-sensors for the detection of Volatile Organic Compounds (VOCs) using e- nose principle (NDA-signed project).

BACHELOR THESIS SCHOLAR

Department Chemical Engineering & Life Sciences, Shiv Nadar University, Uttar Pradesh, India **(10/2016- 05/2017)**

- Established extraction and characterization of silica nanoparticles (SiNPs) from rice husk ash (RHA) to observe the apoptosis event in breast cancer cells with doxorubicin loaded SiNPs treatment.

O.U.R RESEARCH GRADUATE

Department of Nanotechnology & Life Sciences, Shiv Nadar University, India
(10/2016-05/2017)

- Synthesized hydrophobic Carbon Quantum Dots (CQDs) from Pluronics via One-Pot Synthesis method.

SUMMER RESEARCH INTERN

Department of Material Science Engineering, National Institute of Science and Technology (NIST), Odissa, India **(05- 07/2016)**

- Established extraction process of silica nanoparticles (SiNPs) from rice husk ash.

SUMMER INTERN

Department of Research and Development**,** SNAP Natural and Alginate Products Private Limited, Tamil Nadu, India **(05- 07/2015)**

- Established liquid and solid waste management techniques using microbes.

EDUCATION

PhD in Biomedical Engineering

Medical Faculty of Mannheim, University of Heidelberg, Germany
(07/2021- 03/2025)

- **Research Topic:** Development of a heterotypic 3D bioprinted model for Head & Neck Squamous Cell Carcinomas.
- **Advisors:** Prof. Nicole Rotter and Prof. Karen Bieback
- **Notable Coursework & Training:**
  - ✓ The Scientist Entrepreneur (Jan–Feb 2025, University of Heidelberg, Germany)
  - ✓ DKFZ Career Development (Mar–Jul 2024, DKFZ, Germany)
  - ✓ 3D Printing & Biofabrication (Jul 2022, University of Utrecht, Netherlands)
  - ✓ Innovation in Medicine (Aug 2022, University of Groningen, Netherlands)
  - ✓ Entrepreneurship & Innovation (Jun 2023, University of Mannheim, Germany)

Masters in Applied Nanotechnology (Specialized in Bio nanotechnology)

Saxion University of Applied Sciences, Enschede, Netherlands
(09/2018-08/2020)

- **Research Topic:** Hepatocellular carcinoma (HCC) 3D Multicellular Tumor Spheroid (MCTS) model to evaluate nanoparticle penetration.
- **Advisors:** Prof. Séverine Le Gac, Prof. Ruchi Bansal and Prof. Martin Bennink.
- **Honors:** Graduated 2nd in Class of 2020
- **Notable Coursework & Training:**
  - ✓ MicroNanofabrication (November 2019, University of Twente, Netherlands)
  - ✓ Clean Room Training (November 2019, University of Twente, Netherlands)
  - ✓ L'Oréal Display Design Challenge (April 2019, University of Twente, Netherlands)
  - ✓ Future Under The Skin Design Brainstorm Challenge (April 2019, University of Twente, Netherlands)

Bachelors in Chemical Engineering Minor in Biotechnology

Shiv Nadar University, Uttar Pradesh, India
(09/2013-05/2017)

- **Advisors:** Prof. Dr. Sanjeev Yadav, Prof. Dr. Dipak Maity.
- **Honors:** Graduated 3rd in Class of 2017.
- **Notable Conference:**
  - ✓ Chemical Engineering conference (December 2017, IIT Kharagpur, India)

AWARDS AND HONORS

- **3rd Best Poster Award** | ENT Congress 2024, Congress Centre Essen, Germany.
- **Winner** | International Speech Contest (Area Level), Toastmasters International (2024).
- **Finalist** | International Speech Contest (Division Level) 2023, Toastmasters International, Frankfurt, Germany.
- **Finalist** | Falling Walls Lab Heidelberg 2022 Global Pitch Competition, Germany.
- **Finalist** | Best Poster Award, Biofabrication Twitter Conference 2022, International Society for Biofabrication (ISBF).

TEACHING EXPERIENCE

- **Mentor - Master Thesis Student (03/2024 – 09/2024)**
  University of Heidelberg, Germany
  Project: Endothelial angiocrine factors in a 3D in vitro cardiomyocyte-endothelial model.
- **Mentor- Summer Intern (12/2023- 02/2024)**
  Institute of Transfusion Medicine and Immunology, University of Heidelberg, Germany
- **DFG-China Exchange Symposium (09/2023)**
  University Hospital of Mannheim, Germany
  Conducted a **3D Bioprinting Workshop** for 30 exchange students.
- **3D Bioprinting Workshop (01/2022)**
  University of Heidelberg, Germany
  Course: Evaluation of chondrogenic capacity of patient-derived chondrocytes & chondrogenic progenitor cells for advanced Masters students (30 participants).

LEADERSHIP AND SERVICE

- **Chair** | 3R-ECRN Committee, 3R-Network Baden-Württemberg, Germany | 12/2022 – 03/2025
- **President** | Mannheim International Toastmasters | 07/2023 – 06/2024
- **Co-Jury** | Mannheim International Toastmasters - Divisional Contest, Frankfurt | Mar 2024
- **Moderator** | 3R Young Investigator's Symposium- Annual 3R Network BW Conference, University of Heidelberg | Jun 2023
- **Co-Jury & Moderator** | Pitching 3R Science Contest, Germany | 2022
- **Student Cohort** | OPLC Saxion University of Applied Sciences, Netherlands | 2018 – 2020
- **Technical Support Team** | Micro-Nano Conference, Netherlands | 12/2018
- **Department Representative** | Saxion University Open Day | 2018 – 2019
- **Treasurer** | Kalakriti- Art & Design Club, Shiv Nadar University, India | 05/2016-03/2017

PUBLICATIONS

PUBLICATIONS

- **First author publication-** ***Azhakesan A***, *Kern J, Mishra A, Selhuber- Unkel C, Affolter A, Gatenholm P, Rotter N, Bieback K*, 3D Bioprinted Head and Neck Squamous Cell Carcinoma (HNSCC) Model Using Tunicate Derived Nanocellulose (NC) Bioink. Adv Healthc Mater. 2025 Jan 13:e2403114. doi: 10.1002/adhm.202403114. Epub ahead of print. PMID: 39801216.

- **Shared-first author publication-** ***A. Azhakesan***, *E. Seiz, J. Kern, L. Hendricks, J. Fleckenstein, F. Jungbauer, S. Ludwig, C. Brochhausen, L. Bugia, C. Scherl, A. Lammert, N. Rotter, and A. Affolter.* Xeno-free alternatives to the use of fetal bovine serum in head and neck cancer explant culture. Alternatives to Laboratory Animals. 2025;0(0). https://doi.org/10.1177/02611929251351559

- **Co-author Publication-** *Affolter A, Liebel K, Tengler L, Seiz E, Tiedtke M,* ***Azhakesan A***, *Schütz J, Theodoraki MN, Kern J, Ruder AM, Fleckenstein J, Weis CA, Bieback K, Kramer B, Lammert A, Scherl C, Rotter N, Ludwig S*. Modulation of PD-L1 expression by standard therapy in head and neck cancer cell lines and exosomes. Int J Oncol. 2023 Sep; 63(3):102.doi: 10.3892/ijo.2023.5550. Epub 2023 Jul 28. PMID: 37503786; PMCID: PMC10552694.

- **First author publication-** ***Azhakesan A***, *Yadav S, Rajesh V M*. Extraction of silica nanoparticles from Rice Husk Ash (RHA) and its characterization. JSIR-NISCAIR journal, Journal of Scientific & Industrial Research; Vol. 79, July 2020, pp. 656-660; July 2020.

PODIUM PRESENTATIONS

- Flash Talk: STMM Summer Symposium 2024, Mannheim, Germany.
- Flash Talk: Alliance Science Splash 2024, Heidelberg, Germany.
- Flash Talk: ENT Congress 2024, Essen, Germany.

- ‘A comparative study on the suitability of bioinks for 3D bioprinted head and neck tumor model’, ***Azhakesan A***, *Kern J, Bieback K, Affolter A, Rotter N*- CELLINK Partnership Conference 2023, Portsmouth, the United Kingdom.

- ‘Characterization and Further Development of Heterotypic 3D Spheroids from Head and Neck Squamous Cell Carcinomas’, ***Azhakesan A***, *Kern J, Bieback K, Affolter A, Rotter N*- Annual 3R network Baden-Württemberg conference 2023, University of Heidelberg, Germany.

- 3D Bio-printing workshop presentation as a part of DFG- China Exchange 2023 symposium (12-22nd September 2023), UMM Mannheim, Germany.

- ‘Characterization and Further Development of Heterotypic 3D Spheroids from Head and Neck Squamous Cell Carcinomas’, ***Azhakesan A***, *Kern J, Bieback K, Affolter A, Rotter N*- Annual 3R network Baden-Württemberg conference 2022, University of Tubingen, Germany.

- ‘Synthesis of hydrophobic Carbon Quantum Dots (CQDs) via one-pot synthesis method from Pluronics’, ***Azhakesan A***, *Lenin G, Maity D*- O.U.R conference 2017, Shiv Nadar University- Research Institute, India.

- ‘Extraction of silica nanoparticles from Rice Husk Ash (RHA) and its characterization for the therapeutic treatment of breast cancer’, ***Azhakesan A***, *Yadav S, Rajesh V M*, 70th annual session of Indian Chemical Engineering Congress (CHEMCON) 2017, Haldia Regional Centre of IIChE (Indian Institute of Chemical Engineering), India.

POSTER PRESENTATIONS

- ‘3D Bioprinted Head and Neck Squamous Cell Carcinoma (HNSCC)model-a preclinical tool’, ***Azhakesan A***, *Kern J, Mishra A, Selhuber- Unkel C, Affolter A, Rotter N, Bieback K*, STMM Summer Symposium 2024, Medical Faculty of Mannheim, University of Heidelberg, Germany.

- ‘Survival of head and neck squamous cell carcinoma (HNSCC) cells in a 3D bioprinted model: comparing nanocellulose (NC)- vs. gelatin methacrylate in alginate (GelMAA) bioink’, ***Azhakesan A***, *Kern J, Mishra A, Selhuber- Unkel C, Affolter A, Rotter N, Bieback K*, The 3R LAND conference Baden-Württemberg 2024, University of Tubingen, Germany.

- ‘Nanocellulose (NC)-based vs gelatin methacrylate (GelMA) bioink for fabricating a 3D bioprinted head and neck squamous cell carcinoma (HNSCC) model’, ***Azhakesan A***, *Kern J, Bieback K, Affolter A, Rotter N*- 95th Annual Meeting of the DGHNO-KHC, ENT Congress 2024, Congress Centre Essen, Germany.

- ‘Novel alternatives to conventional in-vitro cancer models using 3D-bioprinting technology’, ***Azhakesan A***, *Kern J, Bieback K, Affolter A, Rotter N*- 94th Annual Meeting of the DGHNO-KHC, ENT Congress 2023, Congress Centre Leipzig, Germany.

- ‘3D Bio-Printed HNSCC (Head and neck squamous cell carcinoma) in vitro model for biomedical applications’, ***Azhakesan A***, *Kern J, Bieback K, Affolter A, Rotter N*- 93rd Annual Meeting of the DGHNO-KHC, ENT Congress 2022, Deutsche Messe Hannover, Germany.

- ‘3D Bioprinted HNSCC (Head and Neck Squamous Cell Carcinoma) *in vitro* model’, ***Azhakesan A***, *Kern J, Bieback K, Affolter A, Rotter N*- Biofabrication twitter conference 2022, International Society of Biofabrication (ISBF).

ACKNOWLEDGMENTS

“Plan your work and work your plan.”- *Napoleon Hill*

For my 11th birthday, my dad gifted me a small desk frame with this quote. At the time, I barely paid attention to it, but as the years passed, its meaning became clearer. This PhD journey, with all its challenges and triumphs, would not have been possible without embracing this philosophy every single day. More importantly, this journey has been shaped, nurtured, and enriched by the extraordinary people who have stood by me through the highs and lows, near and far.

So, here’s my chance to say thank you- to my roots in India, to the friends and mentors who became my family in the Netherlands and Germany, and to everyone who played a part in this incredible journey.

To my first and greatest teachers, my biggest cheerleaders and go-to safe heaven, my parents, Azhakesan R and Vijayalakshmi A

Daddy, you have been my constant pillar of strength. Whether it was waking me up every morning with care, checking in on me, or reminding me that everything would be alright despite the numbered miles between us, your presence has been my greatest comfort and strength. Even in my loneliest moments, a simple video call with you made everything feel better again. You are my hero, the one person who never lets me give up, and I will always admire you for that.

Mummy, your resilience and strength have shaped me more than you know. You’ve taught me what it means to truly love what you do and to show up for it every single day. Even from across continents, you’re the first person I turn to when I’m feeling sick or lost. My love for research, my perseverance, it all comes from you.

To my **sister** and **second mother, Ajitha A**, thank you for always breaking my problems down for me whenever I was overwhelmed. Your patience, love, and tough-but-necessary reality checks have been my anchor. Even though we don’t always see eye to eye, your lessons in morality and sacrifice will stay with me forever.

I would also like to thank my old crew of from India. **Chitrakshi Mehta**, **Piu Banerjee**, and **Vignesh Swaminathan**- for being my pillars of support since our Bachelor’s days. **Chitrakshi**, your boundless energy and the way you always check in on everyone mean the world. **Piu**, your calm wisdom and no-nonsense advice have saved me countless times. Even though we do not talk every single day, those long video calls filled with life updates is here to stay. No matter where life takes us, I know this trio will always pick up right where we left off.

Vignesh, you are my go-to person, someone I trust implicitly. Your patience, support, and presence during my toughest times have meant everything. Our bond has only grown stronger, particularly after SNU, as we navigate our careers as European-SNUites side by side.

To **Aman Maheswari,** who became an unexpected but lifelong support system, our time together at Saxion may have been short, but our friendship has endured. Your encouragement and easy-going attitude during stressful times have been exactly what I needed, over and over again.

To my Master's roommates and best friends, **Rachel Phillips** and **Daria Korchun**, you both have been my home away from home. We've seen each other at our best and worst, and yet, our friendship has only grown stronger. With you, I never had to pretend and I could always be my true self. Distance means nothing when the bond is this real and every time, it's like coming home to you two every time.

Karen Bieback, I could not have asked for a better supervisor. From the start, I hoped for a supervisor who was not only brilliant but also genuinely supportive, and I couldn't be more grateful that I found exactly that in you. Your enthusiasm, guidance, and trust in me, especially through opportunities to attend conferences, summer schools and to gain exposure at the 3R-Network committee meetings have been invaluable. I know my long-winded writing is something you are not a fan of, but I hope I've at least improved a little (maybe a 6 or 7 out of 10 now? haha). Your ability to critic in an encouraging manner is something I admire about you, and I believe those skills have might have grown in me, a teeny tiny bit. Thank you for being more than just a supervisor you have been a mentor in every sense of the word, and I am truly grateful for that.

Johann Kern, I've been so lucky to have you as one of my daily supervisors. Your open-door policy- whether for my endless stream of questions (be it dumb or brilliant) or just to check in—made all the difference throughout my PhD. No matter how busy you were, you always took the time to listen, guide, and provide support in your own unique way. And while I may never fully grasp your dark, not-so-humorous Austrian humour (and let’s be honest, I probably never will), I have always appreciated your kindness and the way you genuinely cared about my well-being. Thank you for your patience, support, and for making this journey a little more entertaining!

Nicole Rotter, I am grateful to have been given this incredible opportunity to be part of this research journey. You are a woman of few words, and while I am the opposite, I aspire to communicate with the same precision and brevity you do. I have often wondered about your career path that led you to your role as a clinic director. Over time, I’ve come to understand that reaching such positions requires resilience, perseverance, and determination. If the opportunity arises, I’d love to hear more about your journey over a cup of coffee. Thank you for being both a critical and generous supervisor.

Annette Affolter, thank you for your guidance and support throughout this journey. Your insights, expertise and open discussions on clinical side of the project have helped shape my research, and I am grateful for the time and knowledge you have shared with me.

To my TAC members, **Ruediger Rudolf** and **Katja Breitkopf-Heinlein**, I sincerely appreciate your invaluable insights during all my evaluations. Your feedback played a crucial role in refining my project, and your honest opinions have helped me grow and reach this stage. Thank you for your support and guidance.

Luisa Tengler and **Elena Seiz**, you both became such an integral part of this PhD journey. **Luisa**aaa, my darlinggg and my lab partner-in-crime, I missed you so much in the last year of my PhD! From the weirdly long lab hours to your sharp eye for detail, I’ve always admired your precision and dedication. You have also become my personal unpaid German translator, and I promise to learn German (probably in a decade? :P). I just wish I could have seen you give a presentation at least once before I graduated!

Elena, my pseudo-colleague and my Russian mama, you’ve always had my back, both in and out of the lab. You’ve been my source of support, wisdom, and laughter. Thank you for all the reassurance, great conversations, and being there whenever I needed you. Here’s to one step-one achievement at a time!

I specifically want to thank my long-distance pen-pal, **Maria Helene Welle Kalkvik** from Ocean TUNICELL. Our email sign off exchanges has been the truest highlight to my Monday blues during this PhD journey. I wish to stop for a Glogg next time at Oslo and for the first time to meet you.

Carlo Alberto Paggi, we truly are each other's best conference find! Since the Micro-Nano conference, you've become one of my dearest and truest friends, and my comrade. Over the past six years, we've shared so many roles in each other's life—fellow students, lab mates, mentors, and above all, lifelong friends and well-wishers. I deeply admire your discipline, your ability to juggle a million things at once, and, of course, your legendary Italian-style complaints (especially about mine—oh, the irony!). You have taught me the importance of detaching professional struggles from personal life. Your support, both professionally and personally, has meant the world to me.

I would also like to thank all the members of **HNO**, **ITI**, **3R-Network BW**, **Ocean TUNICELL, AMBER**, **DBE, and, Twente and Mannheim Toastmasters International**. There are too many to name individually, but each of you has been part of this journey in a meaningful way. Thank you for the conversations, collaborations, and support over the years.

Finally, to everyone who has crossed my path during this PhD, whether in good moments or challenging ones, you have all played a role in shaping me into the person I am today. I hope our paths cross again in the next chapter of my journey.

THANK YOU ALL, FROM THE BOTTOM OF MY HEART!!!

Part of the results of this dissertation have been published in…

- **A. Azhakesan**, J. Kern, A. Mishra, C. Selhuber-Unkel, A. Affolter, P. Gatenholm, N. Rotter, K. Bieback, 3D Bioprinted Head and Neck Squamous Cell Carcinoma (HNSCC) Model Using Tunicate Derived Nanocellulose (NC) Bioink. *Adv. Healthcare Mater.* 2025, 14, 2403114. https://doi.org/10.1002/adhm.202403114

- **A. Azhakesan**, E. Seiz, J. Kern, L. Hendricks, J. Fleckenstein, F. Jungbauer, S. Ludwig, C. Brochhausen, L. Bugia, C. Scherl, A. Lammert, N. Rotter, and A. Affolter. Xeno-free alternatives to the use of fetal bovine serum in head and neck cancer explant culture. *Alternatives to Laboratory Animals. 2025;0(0).* https://doi.org/10.1177/02611929251351559